RUSSIAN ACADEMY OF SCIENCES
SIBERIAN BRANCH
INSTITUTE OF THEORETICAL AND APPLIED MECHANICS

SYMMETRIC AND ASYMMETRIC CROSSING-SHOCK-WAVES/TURBULENT BOUNDARY LAYER INTERACTIONS

A.A. Zheltovodov, A.I. Maksimov

EOARD Contract F61708-97-W0136

FINAL REPORT FOR THE PERIOD

JULY 1997 – JULY 1998

19980925 015

DISTRIBUTION STATEMENT A
Approved for public release;
Distribution Unlimited

DTIC QUALITY INSPECTED 1

Novosibirsk 1998

AQF98-12-2553

REPORT DOCUMENTATION PAGE

Form Approved OMB No. 0704-0188

Public reporting burden for this collection of information is estimated to average 1 hour per response, including the time for reviewing instructions, searching existing data sources, gathering and maintaining the data needed, and completing and reviewing the collection of information. Send comments regarding this burden estimate or any other aspect of this collection of information, including suggestions for reducing this burden to Washington Headquarters Services, Directorate for Information Operations and Reports, 1215 Jefferson Davis Highway, Suite 1204, Arlington, VA 22202-4302, and to the Office of Management and Budget, Paperwork Reduction Project (0704-0188), Washington, DC 20503.

1. AGENCY USE ONLY (Leave blank)	2. REPORT DATE	3. REPORT TYPE AND DATES COVERED
	July 1998	Final Report

4. TITLE AND SUBTITLE	5. FUNDING NUMBERS
Symmetric and Asymmetric Crossing-Shock-Waves/Turbulent Boundary Layer Interactions	F6170897W0136
6. AUTHOR(S) Dr. Alexander Zheltovodov	
7. PERFORMING ORGANIZATION NAME(S) AND ADDRESS(ES) Institute of Theoretical and Applied Mechanics Institutskaya 4/1 Novosibirsk 630090 Russia	8. PERFORMING ORGANIZATION REPORT NUMBER N/A
9. SPONSORING/MONITORING AGENCY NAME(S) AND ADDRESS(ES) EOARD PSC 802 BOX 14 FPO 09499-0200	10. SPONSORING/MONITORING AGENCY REPORT NUMBER SPC 97-4045

11. SUPPLEMENTARY NOTES

12a. DISTRIBUTION/AVAILABILITY STATEMENT	12b. DISTRIBUTION CODE
Approved for public release; distribution is unlimited.	A

13. ABSTRACT (Maximum 200 words)

This report results from a contract tasking Institute of Theoretical and Applied Mechanics as follows: The contractor will analyze experimental data (obtained at ITAM) such as surface flow visualization, surface pressure, adiabatic wall temperature and surface heat transfer for symmetric and asymmetric crossing shock waves/turbulent boundary layer interactions as detailed in his proposal submitted in April 97.

14. SUBJECT TERMS	15. NUMBER OF PAGES
Boundary Layer, Separated Flows	76
	16. PRICE CODE N/A

17. SECURITY CLASSIFICATION OF REPORT	18. SECURITY CLASSIFICATION OF THIS PAGE	19, SECURITY CLASSIFICATION OF ABSTRACT	20. LIMITATION OF ABSTRACT
UNCLASSIFIED	UNCLASSIFIED	UNCLASSIFIED	UL

NSN 7540-01-280-5500

Standard Form 298 (Rev. 2-89)
Prescribed by ANSI Std. 239-18
298-102

LIST OF AUTHORS

Date of Signature

Dr. Alexander A. ZHELTOVODOV
Chief of Separated Flows Research Group,
Senior Research Scientist

06.01.98.

Dr. Alexander I. MAKSIMOV
Senior Research Scientist

6.01.98.

FOREWORD

This document presents a detailed experimental investigation of symmetric and asymmetric crossing-shock-waves/turbulent boundary layer interactions. The study was conducted by the Supersonic Separated Flows Research Group of the Supersonic Combustion Laboratory, Institute of Theoretical and Applied Mechanics, Rusian Academy of Sciences, Siberian Branch (Russia, Novosibirsk).

This final report, submitted by the authors, describes all the work accomplished for the duration of the EOARD Contract F61708-97-W0136 (monitor Dr. C.Raffoul) from July 1997 to July 1998.

ABSTRACT

Three-dimensional interaction between a turbulent boundary layer and a sequence of crossing shocks and expansion waves arising between two symmetric and asymmetric vertical fins with side inclination angles $\beta = 7°$, 11°, and 15°, which are mounted on a plate, is experimentally studied. For Mach numbers $M_\infty = 3$ and 3.9 new data for combinations of fin angles $\beta_1 \times \beta_2$ equal to 7°×7°, 11°×11°, 15°×15° 7°×11°, 7°×15°, and 11°×15° are obtained on the structure of the limiting streamlines, surface pressure and heat transfer coefficients distributions, which clarify considerably the topological features of these flows at various stages of their development. On the basis of obtained results and generalization of previous studies, the influence of unsteady effects on some flow properties is explained. New information also forms the basis for verification of today's numerical methods.

CONTENTS

Page

1. INTRODUCTION 6

2. TEST MODELS, TECHNIQUES AND EXPERIMENTAL CONDITIONS

2.1. Windtunnel Facility, Test Conditions and Test Model 8

2.2. Instrumentation and Technique.

2.2.1. Surface Flow Pattern Visualization 9

2.2.2. Surface Pressure and Heat Transfer Distributions Measurements 9

3. SYMMETRIC INTERACTIONS 10

4. ASYMMETRIC INTERACTIONS 17

5. CONCLUSIONS 26

6. ACKNOWLEDGEMENTS 27

7. REFERENCES 28

8. FIGURES 33

9. APPENDICES

Appendix 1: The photographs of surface flow pattern 53

Appendix 2: Surface pressure distributions 66

Appendix 3: Surface heat transfer coefficient distributions 69

1. INTRODUCTION

The study of the shock wave/turbulent boundary layer interaction is one of the classical problems of gas dynamics, which is of great practical importance. Situations that occur in a supersonic flow around three-dimensional configurations attract now the major interest. These conditions are observed in inlet ducts and in external flow around various control surfaces of flying vehicles. Available experimental data, for example, [1–3] testify to a complex flow structure in inlets with three-dimensional compression, which is caused by the interaction of shocks and expansion waves between themselves and with a turbulent boundary layer developed on the surfaces. Prediction of their properties is a complex problem [4–7]. The absence of a single and reliable theoretical basis for turbulence description hinders the development of advanced numerical methods. Thus, their further development is determined to a large extent by the informativeness of experimental research used to construct physical flow schemes, justify the efficiency of chosen turbulence models, and test the numerical methods [4-10].

Further development and testing of advanced numerical methods requires a deeper understanding of the physics of these flows by the example of simplified canonical configurations that simulate the elements of real constructions. One of these configurations is a plate with two vertical fins, which induces in a supersonic flow a complex interaction between crossing shock waves with a turbulent boundary layer (Fig. 1). The first experimental and theoretical studies of such a configuration with small and moderate fin inclination angles were conducted more than a decade ago [11]. Since that time the interest in this problem has greatly increased due to the development of hypersonic scramjet, and a considerable number of papers have been published, which deal with similar problems [12–43].

The majority of known experimental and numerical works [11–35, 39, 40, 42], are devoted to the analysis of flows formed between two identical symmetrically located fins (symmetrical interactions). Asymmetrical interactions near the fins with different angles β of the side faces have been studied much less [11, 13, 35–42]. All these studies cover the Mach number range from 1.85 to 8.3 and $\beta = -3° - 15°$. Special emphasis in most papers is on the analysis of pressure distribution and the structure of the limiting streamlines on the plate surface in the interaction region. The most complete cycle of experimental researches of the symmetrical interaction between crossing shock waves with a turbulent boundary layer for $M_\infty = 3$ and 4 is presented in the papers [17–20, 22, 24, 28, 29]. Apart from the patterns of the limiting streamlines and pressure distribution on the plate surface, these works present the data on the distribution of the skin friction coefficient, total pressure fields and local angles of flow direction, as well as the optical visualization of a 3D flow pattern being formed. Fairly complete measurements of pressure distribution and heat-transfer intensity together with the fields of various parameters under the conditions of symmetrical interaction are analyzed for two situations ($M_\infty = 8.3$, $\beta_1 = \beta_2 = 10°$ and 15°) in [15, 23, 26, 27]. It is necessary to note that additional information about the heat transfer and the data on pressure distribution and the structure of the limiting streamlines

was obtained only by the authors of the present paper at $M_\infty = 3.9$ for some cases of symmetrical and asymmetrical interactions [35–40]. We should also emphasize the pioneering study [43] of symmetrical interaction for M_∞=3.85 near the fins with $\beta_1 = \beta_2 = 15°$ mounted on the surface of a 2D compression corner ($\alpha = 10°$). The data on the gas dynamic structure of this more complex flow obtained on the basis of optical visualization and the limiting streamlines on the surface are important for testing the up-to-date calculations and searching for effective configurations of inlets with 3D compression.

The studies dealing with unsteady effects are not numerous at the moment, but extremely important. The authors of [12] were, apparently, the first to measure the pressure and temperature fluctuations on the surface for the case of symmetrical interaction. These measurements allowed the authors to assume the existence of relationship between the fluctuations of these parameters and heat transfer intensity fluctuations. More detailed measurements of pressure fluctuations were performed later in [13, 19].

It should be noted that fins with flat internal faces that form a converging half-channel were used in most experiments, except for [15, 23, 26, 27] and performed by the authors of the present paper [35–40]. There was only one intersection of shock waves because of the threat of half-channel blockage, and the downstream region of investigation on the plate was limited. In the above papers the side faces had inflected generatrices with a constant-width channel behind the inflection (see Fig. 1). Specific features of the flow in these conditions are determined by the boundary layer interaction with a sequence of crossing shocks and expansion waves.

Of undoubtful interest are scarce investigations of asymmetrical interactions with different inclination angles of the fin sides $\beta_1 \neq \beta_2$ [11, 13, 35–41]. These studies are important, for example, for estimating a possible effect of the angle of sideslip on inlet flow and constitute a more general test case for validation of numerical methods. The first study of asymmetrical interactions for the Mach number $M_\infty = 1.85$ seems to be performed in [11] for various combinations of angles β_1 and β_2 in a limited range of their values from -3° to +9°. The data obtained for the limiting streamlines and pressure distributions on the surface allow one to characterize specific features of these flows under the conditions of boundary layer crossing weak shocks and expansion waves which do not cause its separation. It was shown on the basis of the theoretical model [44] that it is possible to predict some flow properties in the region of crossing disturbances, using a superposition of solutions for two isolated fins. Detailed data were obtained in [13] about the mean pressure distributions and its fluctuations on the surface for more intense asymmetrical interactions with intersecting shock waves at $M_\infty = 2.95$ and combinations of angles $\beta_1 \times \beta_2 = 7° \times 9°$ and $7° \times 13°$. An important feature is the high-frequency pressure fluctuations directly behind the calculated points of crossing shocks, corresponding to inviscid flow conditions, which were registered in experiments.

Advanced numerical studies of examined flows are based on the numerical solution of the full averaged Navier–Stokes equations with the use of various turbulence models: algebraic (Baldwin-Lomax and its modifications) and differential (k-ε, k-ω, k-l and their modifications) models, and also the Reynolds stress equations. The calculations

conducted for symmetrical [14, 18, 20, 21, 24–27, 29–34, 39, 40, 42] and asymmetrical [35–41] interactions and for symmetrical fins mounted on the compression surface [34, 43] demonstrated a reasonable agreement with experiments on pressure distribution on the plate surface, total and static pressure fields, Mach numbers and local angles of flow deflection, and the structure of waves formed in the interaction region. However, the agreement between the calculated and experimental fields of various parameters becomes much worse inside the central separation region formed in the vicinity of crossing shocks where viscous effects are essential, as compared with external regions of the boundary layer where an inviscid flow is mainly obtained [21, 29].

It should be noted that, according to results presented in [24–28, 30–43], an appreciable disagreement is observed under the considered conditions between the calculated and experimental heat-transfer and skin-friction coefficients. Besides, principal differences in topology of the limiting streamlines in the interaction region obtained numerically and experimentally [20, 24–26, 28, 31–34, 43]. This refers primarily to the position and type of singular points, and the exact position and shape of the separation and reattachment lines near these points. In particular, none of topological schemes on the plate surface obtained in numerical experiment corresponds to experimentally registered patterns [20, 22, 28] for moderate Mach numbers ($M_\infty = 3$ and 4). Besides, the calculated patterns of the limiting streamlines, like the distributions of the skin-friction and heat-transfer coefficients, depend substantially on the choice turbulence models, neither of which is preferable. Experimental patterns of the limiting streamlines for $M_\infty = 8.3$ [15], which are compared with the calculations in [23, 25–27, 32, 33, 42], are not very distinct and do not allow one to determine exactly the type and position of singular points under these conditions.

The difference between the calculated and experimental topological schemes necessitates further investigations for obtaining additional information supporting or refuting their validity. It should be also noted that the above cited papers, including those published by the authors, avoid analyzing the specific features of the flow around the side walls of the channel formed by the fins and the junctions of various surfaces. Very scarce data available in [15, 18, 28] on the limiting streamlines on the side surface near a single incident shock wave, compared with calculations in [18, 20, 27, 32, 42] are not representative and do not give a sufficient characteristic of their topological features. meanwhile, the flow analysis in these regions is extremely important as the basis for designing the elements of flying vehicles, in particular, inlets, and also for verification of today's numerical models. This gap is partly filled by the papers [45–47] dealing with the interaction of an incident oblique shock wave with the boundary layer on the surfaces of open streamwise corners and in a half-channel. Results presented in these works show a necessity of more careful examination of the topological schemes obtained.

The main objective of the present study is a further experimental investigation of a supersonic flow around the configuration shown in Fig. 1 and the refining of topology of 3D separated flows arising in these conditions at various stages of their development. Special emphasis is laid on the verification of the correspondence between various parameters measured in experiments with the structure of the limiting streamlines to obtain the basis for verification of today's computational methods.

2. TEST MODELS, TECHNIQUES AND EXPERIMENTAL CONDITIONS

2.1. Windtunnel Facility, Test Conditions and Test Model

The experiments were performed in a supersonic wind tunnel T-333 of ITAM SB RAS [48] with the test section in the form of Eiffel chamber and a 30 cm initial diameter of the incoming stream.

Experimental conditions are listed in the table 1.

Table 1

Mach number M_∞	3	3.92±0.03
Total pressure P_0, Mpa	0.85 - 1.0	1.48 ± 0.02
Static pressure P_1, kPa	21 - 25	11.30 ± 0.01
Stagnation temperature T_0, K	260	260 ± 2
Reynolds number Re_1, m^{-1}	$80 \cdot 10^6$	$(89 \pm 4) \cdot 10^6$
Boundary layer thickness δ, mm	3.4	3.5
Boundary layer displacement thickness δ_1, mm	1.12	1.12

A sketch of the test model under study and the coordinate system used hereinafter are shown in Fig. 2. The model is a plate with two symmetrically or asimmetrically mounted fins with sharp (~0.1 mm) leading edges. Their height is 100 mm, and their total length is 192 mm. The fin vertices are located at a distance of 210 mm from the leading edge of the plate, which ensured a developed turbulent boundary layer of thickness δ upstream of the fins. Six configurations used in experiments for combinations of fin angles β_1 and β_2 equal to 7°×7°, 7°×11°, 7°×15°, 11°×11°, 11°×15° and 15°×15°. For these variants the width of the channel entrance was $b = b_1+b_2 = 71.5$, 73.6, 75.4, 75.6, 77.4, and 79.1 mm. The size of the constant-width channel section was the same in all cases (32 mm). Table 2 shows the coordinates b_1 and b_2 of fin vertices with respect to the channel centerline, which is the symmetry axis of the constant-width section. This model allowed us to study the boundary layer interaction with successively crossing shocks and expansion waves of various strength.

Table 2

$\beta_1 \times \beta_2$	7° × 7°	7° × 11°	7° × 15°	11° × 11°	11° × 15°	15° × 15°
b_1, mm	35.75	35.8	35.8	37.8	37.8	39.55
b_2, mm	35.75	37.8	39.6	37.8	39.6	39.55

The fins were positioned on replaceable inserts flush-mounted with the plate surface (see Fig. 2). Steel polished inserts with smooth and perforated surfaces were used in experiments on visualization of the limiting streamlines and pressure measurements, respectively. The pressure orifices 0.5 mm in diameter were located in four sections: one longitudinal section along the plate centerline and three cross-sections at distances of 46, 79, and 112 mm from the leading edges of the fins.

A textolite insert was used for heat-transfer measurements. The insert surface was covered with current-conducting film of special graphite paste ~0.1 mm thick. Eighty

chromel-coppel thermocouples with wire diameter of 0.2 mm were installed under the film and a thin layer of electroinsulating varnish. Thermocouple coordinates were analogous to the coordinates of the corresponding pressure orifices. Cables for electric current supply were located along the leading and trailing edges of the film.

2.2. Instrumentation and Technique

2.2.1. Surface Flow Pattern Visualization

Visualization of the limiting streamlines on the model surface was performed using a 10-15% mixture of lampblack and transformer oil. To increase the contrast of obtained photos the model was covered with white paint, while the amount and concentration of the oil-lampblack mixture were chosen individually for each configuration. For convenience, the plate was mounted in the vertical position, which led to a certain asymmetry of the visualization picture with respect to the longitudinal axis of the model due to gravitational force effect on the oil-soot mixture accumulated at the central separation line. Special studies showed that this influence becomes much more significant in the downstream direction along the considered line as the run time is increased. Topological schemes presented below take into account these optical distortions, as well as those caused by the fin three-dimensionality, which were eliminated to the largest possible extent in computer processing of the visualization patterns photographs. The photographs of surface flow pattern are presented in the Appendix 1.

2.2.2. Surface Pressure and Heat Transfer Distributions Measurements

The pressure distribution was measured by silicon integral membrane pressure gages and group manometers of class 0.5 (with the measurement range of 0-0.1 MPa). The pressure orifices coordinates together with the measured pressure values are tabulated in the Appedix 2.

The heat transfer coefficients were measured by a calorimetric technique suggested in [49]. A steady adiabatic temperature of the film T_{aw} and a steady temperature of the heated surface T_w (after supplying the electric current to the film) were measured in the course of experiment. Electric power supplied to the film was calculated from the measured values of current and voltage. The ratio of this power to the film surface determines the mean heat flux q_m entrained from the film. The value of the heat transfer coefficient C_q was determined as

$$C_q = q/(T_w - T_{aw}) .$$

Here $q = k \times q_m$, where k is a coefficient individual for each thermocouple, which is obtained by means of prior calibrations and takes into account the effect of possible inhomogeneity of the current-conducting film. The employed technique for determining the heat transfer coefficients was justified only for films with rectangular planform, therefore, the number of thermocouples in cross-sections of a heat-insulated plate was smaller than the number of pressure orifices. Thermocouples coordinates together with the measured heat traansfer coefficient values are tabulated in the Appedix 3.

The measurement error of surface pressure P was ±0.5%, and the maximum error of the relative quantity P/P_1 did not exceed 10%. The random measurement error of the heat transfer coefficients, which was caused by the measurement errors of temperature, heat flux and individual coefficients k, being recalculated in the nondimensional form C_q/C_{q1} could reach 5% of its local value. Systematic errors caused by the heat flux losses for radiation and heat overflow are estimated as about 10%. (Here and below P_1 and C_{q1} are the pressure and heat transfer coefficients measured on the plate surface in the free stream undisturbed by the shock waves for $x = 0$ and 30 mm, respectively).

3. SYMMETRIC INTERACTIONS

Obtained on the basis of careful analysis of the oil-film visualization, the topological schemes of the limiting streamlines on the plate and fin surfaces together with the pressure and heat flux distributions on the plate allow one to refine substantially the specific features of flows under consideration. The schemes analyzed below are in qualitative and quantitative agreement with the limiting streamlines registered on the photographs.

In all considered cases, the flow at the entrance of the channel formed by two fins is determined by the interaction of glancing shock waves, generated by the fins, and a turbulent boundary layer on the plate. The main features and regimes of its development up to the region of secondary flows arising near the model centerline are similar to those typical of one isolated fin, which was previously studied in detail in [50–53]. In all topological schemes (Figs. 3–5, 8, 9, 11) the letter "a" refers to the limiting streamlines on the side surfaces of the upper (left with respect to the flow) fin, the letter "b" to the flow patterns on the plate surface. Since the flow patterns on the surfaces of both fins are almost identical for the symmetric interactions, we present here the schemes for only one (upper) fin, all its faces being sweeped into a single plane. The letters in the figures denote: "***S***" – separation lines (convergence of the lampblack-oil mixture), "***R***" – divergence lines (flow reattachment), "***U***" – lines of pressure growth beginning (upstream influence lines), singular points (saddles, nodes, and foci) are denoted by "***C***", "***N***", and "***F***", respectively. The arrows indicate the local flow directions.

For the case $\beta_1 = \beta_2 = 7°$ and $M_\infty = 3$ (Fig. 3, *b*) the non-separated flow behind the fins is characterized by a smooth turning of the limiting streamlines towards the channel axis along the inviscid shock traces (dashed lines). These lines asymptotically approach each other to form a narrow zone of parallel motion, a convergence zone. For simplicity, some limiting streamlines reaching this region are conventionally terminated in the figures. A local (singular) separation arises only in the immediate vicinity of the leading edges of the fins in saddle points ***C*** (Fig. 3, *c*) with flow reattachment in node points ***N*** which can shift from the plate to the side surfaces of the fins as β increases. Separation lines $\boldsymbol{S}_1$ and $\boldsymbol{S}_2$ emerging from the saddle points degenerate into convergence zones in the region of 3-D secondary flows.

The mutual influence of the fins starts to manifest itself when the lines of pressure growth beginning ***U*** (shown by thin dash-dotted lines in Fig. 3, *b*) merge. These lines are accompanied by the curvature of streamlines induced by shock waves. A characteristic throat is formed near the calculated point of shocks intersection. Practically all limiting streamlines captured by the channel entrance cross-section are compressed and enter this

throat. Secondary separation lines $\boldsymbol{S}_3$ and $\boldsymbol{S}_4$ are formed due to the interaction of intense secondary flows arising at the fin base with the flow passing through the throat. It should be noted that the character of these lines is similar to open separation, when the separation lines contain only regular points and do not start in singular points [54]. The overall flow pattern near the first intersection of shocks is analogous to that registered in similar conditions for fins with flat side surfaces [22, 24, 28]. Distributions of the skin friction coefficient C_f measured in these works reveal its dramatic decrease along the symmetry axis when the flow passes through the throat. Its value does not reach zero, however, which proves the absence of the boundary layer separation in this region. At the same time, some signs of formation of an asymmetric separation region were found in these experiments behind the throat ahead of the calculated point of secondary intersection of shock waves reflected on the fin surfaces (Fig. 3, *b*). This separation region is similar to that arising in an extended 3D-compression inlet at the early stage of its choking [3, 7]. The topological scheme of the limiting streamlines near this region (Fig. 3, *d*) is characterized by two saddle points $\boldsymbol{C}_1$ and $\boldsymbol{C}_2$ and two foci $\boldsymbol{F}_1$ and $\boldsymbol{F}_2$. Such a combination of singular points is associated with the formation of a pair of tornado-shaped vortices propagating downstream from points $\boldsymbol{F}_1$ and $\boldsymbol{F}_2$ [55, 56]. It can be assumed that the increasing channel blockage by these vortices under the conditions of growing central separation region is one of important factors that favor the channel choking. A qualitatively similar flow picture was obtained in the region of the first calculated intersection of shock waves after their interaction with a fairly thick boundary layer ($\delta = 30$ mm, $b/\delta = 10.5$) at the stage preceding the channel choking with $M_\infty = 3.44$ and $\beta_1 = \beta_2 = 9°$ [19]. The same features are typical of the choking stage of convergent inlets studied in [2]. Figure 4 shows a scheme corresponding to the complete channel choking, which was obtained for $\beta_1 = \beta_2 = 15°$ and $M_\infty = 3$. It is seen that the topology of the limiting streamlines on the plate in this case (Fig. 4, *b*) is similar to that considered above. It is characterized by the presence of two saddle points $\boldsymbol{C}_1$ and $\boldsymbol{C}_2$ and two foci $\boldsymbol{F}_1$ and $\boldsymbol{F}_2$. Simultaneously, in this situation the separation lines $\boldsymbol{S}_1$ and $\boldsymbol{S}_2$, emanating from the saddle point $\boldsymbol{C}_1$, are formed in front of the channel entrance, and a complete blockage of the channel by the separation region is observed. There are two reattachment lines $\boldsymbol{R}_1$ and $\boldsymbol{R}_2$ near the fin base, along which the flow reattachment can occur.

The patterns of the limiting streamlines on the side surfaces of the channel formed by two fins have some additional features. Narrow 3D separation regions, bounded by the lines of separation $\boldsymbol{S}_5$ and reattachment $\boldsymbol{R}_5$, with the maximum width of 5–6 mm are formed at $M_\infty = 3$ and $\beta_1 = \beta_2 = 7°$ (Fig. 3, *a*) at a certain height from the fin base in the region of calculated place of incidence of secondary "inviscid" shocks onto the fin surface. For an inviscid flow over the side surface with the Mach number $M_2 = 2.66$ the calculated pressure ratio in the secondary and reflected shocks incident onto it is $P_4/P_2 = 2.4$. According to [7, 51], this value is quite sufficient for an onset of turbulent boundary layer separation, since in the present conditions it is higher than the critical shock strength $\xi^* = 2.32$. The curvature of lines $\boldsymbol{S}_5$ and $\boldsymbol{R}_5$ in the upper part and the upstream flow orientation inside the separation region bounded by these lines are caused by tip effects due to finite fin height. There is no boundary layer separation on the side surface near the plate, and the limiting streamlines are only slightly curved near the boundaries of a system of compression waves, which are shown by the dashed lines. Like in the case of isolated

fin [52], these compression waves are formed in the base of the shock wave incident onto the fin face, due to the shock/boundary layer interaction on the plate. In the case under consideration, their strength is insufficient to cause the boundary layer separation. As it follows from the above cited work, as the shock wave strength increases, it base is transformed to a λ-configuration of shocks separating the boundary layer. Under these conditions the upstream-curved separation line S_5 (Fig. 3, *a*) should extend ahead of the λ-configuration as far as to the plate surface. Exactly this typical shape of the separation line S_5 is observed in the case of channel choking (Fig. 4, *a*). This explanation of the separation line shape near the fin base makes clearer the concept [45], wherein similar features in a streamwise corner are associated with a separation-prone 3D boundary layer formed at the junction of surfaces. The upward deviation of streamlines from the line of wedge/plate junction, observed in Figs. 3, *a* and 4, *a*, is related to the influence of low-scale streamwise vortex formed here, which was found in [53] near the isolated fin base.

An increase of the free-stream Mach number to $M_\infty = 3.9$ affects significantly the evolution of considered flows with changing β. For $\beta_1 = \beta_2 = 7°$ (Fig. 5, *b*, *c*) the limiting streamlines on the plate surface, entering the throat near the first intersection of shocks, propagate without separation to the region of their second intersection. Being compressed in the throat, these lines diverge a little and then converge again to a certain downstream asymptotic separation line together with secondary separation lines S_3 and S_4 which cover this region. The pressure distribution along the model centerline in this case (Fig. 6, *a*) is practically the same as for an isentropically converging supersonic stream tube. As we move downstream from the intersection point of the upstream influence lines (x = 46–48 mm), its gradual increase is observed, and at $x > 140$ mm the calculated pressure level behind the crossing shocks in an inviscid flow is almost achieved (it is shown by the horizontal dashed line).

The character of pressure distribution in cross-sections I, II, and III, corresponding to x = 46, 79, and 112 mm (Fig. 5, *b*), is illustrated in Fig. 6, *b–d* (lower curves). The vertical sections in these figures show the side faces of the fins. The thin dashed lines indicate the calculated pressure distributions for an inviscid flow. It is seen (Fig. 6, *b*) that in cross-section I, which is located slightly upstream of the crossing point of the lines of pressure growth beginning, the measured pressure distribution (lower curve) corresponds to that for two isolated fins located symmetrically about the centerline, and the pressure level increases gradually in secondary flow regions formed near the fins. In cross-section II (Fig. 5, *b*) the flow is compressed between the shocks in the region of streamlines converging to the axis, and a region of elevated and nearly constant pressure appears (Fig. 6, *c*). Finally, in cross-section III an explicit pressure peak is formed at the centerline (Fig. 6, *d*) behind the throat, where the streamlines slightly diverge (Fig. 5, *b*).

In the case under consideration ($\beta_1 = \beta_2 = 7°$, $M_\infty = 3.9$) the heat transfer coefficient C_q in the interaction region $46 < x < 140$ mm (Fig. 7, *a*) remains practically constant on the background of gradually increasing pressure along the model centerline (Fig. 6, *a*). Obviously, an intense thickening of the boundary layer in this region due to flow convergence from the fins to the axis compensates for the influence of increasing pressure. Under the conditions of constant pressure for $x < 46$ mm a natural downstream increase of the boundary layer thickness on the plate causes a gradual decrease of C_q/C_{q1}. A negative gradient in the C_q/C_{q1} distribution revealed for $x > 145$ mm is connected with

the influence of expansion waves at the end of the channel, which originate on the inflections of the side surfaces of the fins. According to the measurements in cross-sections I-III (Fig. 7, *b–d*, lower curves), the lowest values of C_q/C_{q1} are observed in the elevated-pressure convergence region formed along the centerline, and then C_q/C_{q1} increases towards the fins. A similar heat transfer minimum on the background of pressure maximum was registered in the vicinity of the streamwise convergence region formed behind symmetrical skewed steps [57].

The character of the limiting streamlines on the side surface of the fin in the case under consideration (Fig. 5, *a*) is qualitatively similar to that discussed previously for $M_\infty = 3$ (Fig. 3, *a*). As the Mach number increases, the separation region bounded by lines $\boldsymbol{S}_5$ and $\boldsymbol{R}_5$ slightly decreases in length and it shifts to the channel throat in accordance with the calculated incident shock position. The region of compression fan near the plate (dashed lines), where a typical curvature of streamlines is observed, becomes significantly wider.

As the fin angle is increased up to $\beta_1 = \beta_2 = 11°$ at $M_\infty = 3.9$ (Fig. 8), separation regions, that existed previously at a certain distance from the leading edges, turn to separation lines $\boldsymbol{S}_1$ and $\boldsymbol{S}_2$ (Fig. 8, *b*), and clear reattachment lines $\boldsymbol{R}_1$ and $\boldsymbol{R}_2$ appear on the plate near the fin base. These features testify to gradual transformation of secondary flows into separated flows [4, 7] and to an increase in intensity of transverse flows directed to the axis. The throat formed between the lines $\boldsymbol{S}_1$ and $\boldsymbol{S}_2$ becomes narrower, and the flow expanding behind the throat and directed along the symmetry axis is decelerated slightly upstream of the point of the first intersection of the shocks. The topological scheme in Fig. 8, *b*, *c* is associated with the emergence of a non-closed central separation region of the "horse-shoe" vortex type [55, 56], whose separation surface begins from the convergence lines $\boldsymbol{S}_5$ and $\boldsymbol{S}_6$ propagating from the saddle point $\boldsymbol{C}_1$. The node point $\boldsymbol{N}_1$ located downstream gives birth to the streamwise reattachment line $\boldsymbol{R}_5$ of limited length, which gradually degenerates behind the separation region into a dividing streamline along the axis in the region of meeting transverse flows. The character of the flow around the side inflections of the fins at the entrance of a constant-width half-channel is partly determined by the influence of expansion waves emanating from these inflections, which are not shown in the figure for the sake of simplicity. Obviously, the influence of these waves favors a more intense motion of the near-wall flow towards the faces. Following [58, 59], these expansion waves also favor the curvature and amplification of shock waves of the opposite family, generated by the fins, which enter the chanel. The limiting streamlines upstream of repeatedly crossing shocks deflect towards the axis without any signs of separation formed in this region. A qualitatively similar topology of the limiting streamlines in the separation region formed in the vicinity of shocks intersection was registered in [22, 24, 28] under the same conditions for fins with flat side surfaces. Special attention should be paid to a principal difference in topological features of the examined separated flow from the regimes of incipience and complete channel choking typical of lower Mach number, which points to different "scenarios" of their development.

The pressure distribution along the centerline under the considered conditions ($\beta_1 = \beta_2 = 11°$, $M_\infty = 3.9$) shows the origin of a typical pressure plateau between the singular points $\boldsymbol{C}_1$ and $\boldsymbol{N}_1$, inherent in separated flows (Fig. 6, *a*). The relative pressure here is

close to the plateau value $P_p/P_1 \approx 3$ calculated for 2D separation for the considered value of M_∞ [7]. In this case, the separation region formation is quite regular here, in contrast to the situation $\beta_1 = \beta_2 = 7°$. A more intense pressure growth is observed again behind the point N_1, reaching the maximum value, equal to the calculated one behind the intersection of inviscid shocks, at $x \approx 130$ mm. Further downstream a dramatic pressure decrease is registered with a minimum at $x \approx 145$ mm, which is caused by expansion fans induced by the fin surface inflections. A repeated increase in pressure is then observed near the second intersection of shocks.

The pressure distributions in cross-sections I, II, and III are presented in Fig. 6, *b-d* (middle curves). Its qualitative character is similar to the previously considered case $\beta_1 = \beta_2 = 7°$ (lower curves), but the pressure level is higher. The pressure peaks in cross-section II ($x = 79$ mm) roughly coincide with the separation lines $\boldsymbol{S}_1$ and $\boldsymbol{S}_2$ that embrace the separation region (Fig. 8, *b*). The maxima observed in cross-section III ($x = 112$ mm) correspond to the reattachment lines $\boldsymbol{R}_1$ and $\boldsymbol{R}_2$ near the fins at points $z \approx \pm 10$ mm, and to the central reattachment line $\boldsymbol{R}_5$ at point $z = 0$.

A vast separation region bounded by lines $\boldsymbol{S}_7$ and $\boldsymbol{R}_7$ is formed on the fins behind the side surface inflections at $\beta_1 = \beta_2 = 11°$ (Fig. 8, *a*). The behavior of the limiting streamlines allows one to assume the existence of singular points: saddle $\boldsymbol{C}_2$ and focus $\boldsymbol{F}_1$. We can suppose that a vortex propagates downstream over the surface from the point $\boldsymbol{F}_1$. These features are more clearly revealed at further stages of evolution of these flows, which are analyzed below.

The schemes of the limiting streamlines corresponding to the case $\beta_1 = \beta_2 = 15°$, $M_\infty = 3.9$ are presented in Fig. 9. A developed separation is formed at the channel entrance in these conditions. This is evidenced by the upstream influence lines $\boldsymbol{U}$ (Fig. 9, *b*) approaching the separation lines $\boldsymbol{S}_1$ and $\boldsymbol{S}_2$, which is typical of separation flows near isolated fins [7, 51]. A narrow throat is preserved between the lines $\boldsymbol{S}_1$ and $\boldsymbol{S}_2$. A large-scale central separation region bounded by separation lines $\boldsymbol{S}_5$ and $\boldsymbol{S}_6$ is formed behind this throat (Fig. 9, *b*, *c*). The saddle point $\boldsymbol{C}_1$ and the node $\boldsymbol{N}_1$ are located upstream of the first calculated intersection of shocks. The lines of secondary separation $\boldsymbol{S}_3$ and $\boldsymbol{S}_4$, propagating from the fins, merge with lines $\boldsymbol{S}_5$ and $\boldsymbol{S}_6$ approximately in the middle of the central separation region and are entrained together downstream along the symmetry axis. Additional separation lines $\boldsymbol{S}_7$ and $\boldsymbol{S}_8$ are clearly seen on the plate surface. These lines are caused by the action of internal shocks reflected on the side surfaces. It can be assumed that the appearance of these lines can be also favored by additional shocks caused by flow overexpansion in expansion waves propagating from fin inflections. The behavior of streamlines behind the corner points does not contradict this conclusion.

The pressure distribution along the symmetry axis in the examined case ($\beta_1 = \beta_2 = 15°$, $M_\infty = 3.9$) is characterized by a plateau region behind the saddle point $\boldsymbol{C}_1$ (Fig. 6, *a*) inherent in developed separated flows. A pressure maximum is formed behind the node point $\boldsymbol{N}_1$, the pressure level there almost reaches the calculated inviscid value behind the first intersection of shocks. A rapid decrease in pressure is then observed due to expansion fans propagating from the surface inflections, and its repeated increase caused by the action of shock waves reflected on the side surfaces (see Fig. 9, *b*). The heat transfer coefficient distribution has approximately the same character (Fig. 7, *a*). At the same time, a typical feature is the formation of an explicit heat flux peak in the supposed

node point N_1, which elucidates its position, and a section of its gradual decrease at x = 70–82 mm. In the region $x \approx$ 90–110 mm, where a distinct pressure peak is formed, the distribution of C_q/C_{ql} has a more complicated character.

The distributions of relative pressure and heat transfer coefficient in cross-sections I, II, and III are shown in Figs. 6, *b–d* and 7, *b–d* (upper curves), respectively. The pressure maximum (Fig. 6, *b*), which appears at the centerline (z = 0) in cross-section I (x = 46 mm), corresponds to the flow compressed in the throat (Fig. 9, *b*). No specific features are observed in the heat transfer distribution in this region (Fig. 7, *b*). The pressure and the heat transfer intensity increase dramatically towards the fins. The high-pressure region observed in cross-section II (x = 79 mm) near the axis (Fig. 6, *c*) corresponds to the central separation region. The pressure level is significantly lower here than its calculated inviscid value behind the crossing shocks (dashed line). The pressure mimima at $z \approx$ 6-7 mm correspond approximately to the separation lines $\boldsymbol{S}_1$ and $\boldsymbol{S}_2$ that cover the central separation region (see Fig. 9, *b*, *c*), and additional maxima are formed at points with coordinates $z \approx \pm 10$ mm near the reattachment lines $\boldsymbol{R}_1$ and $\boldsymbol{R}_2$. The heat transfer intensity increases also in the direction from the axis to these reattachment lines (Fig. 7, *c*). In cross-section III (x = 79 mm) the pressure attains the maximum value at the dividing streamline formed on the axis behind the separation region (Fig. 9, *b*) and drastically decreases at $z \approx \pm 10$ mm due to the influence of expansion waves propagating from the side surface inflections (Fig. 6, *d*). When approaching the fins, a repeated growth of pressure is observed behind the separation lines $\boldsymbol{S}_7$ and $\boldsymbol{S}_8$ in the influence region of secondary shocks reflected on the fin surfaces. The heat transfer coefficients also decrease dramatically in the influence region of expansion waves (Fig. 7, *d*). Contrary to pressure, a heat transfer minimum is formed on the central dividing line.

The topological flow scheme on the side surface of the fin for the considered case reveals a larger separation region between the separation line $\boldsymbol{S}_9$ and reattachment line $\boldsymbol{R}_9$ (Fig. 9, *a*) that for $\beta_1 = \beta_2 = 11°$. Obviously, this is primarily caused by increasing strength of the shocks incident onto the fin surfaces. It can be also assumed that the observed growth in the absolute scale of separation is also caused by a prior action on the boundary layer of more intense expansion fans propagating from the surface inflections, like in the flow over backward-facing steps with inclined faces [60]. According to that paper, the suppression of turbulence by expansion waves (relaminarization) in the near-wall part of the boundary layer immediately ahead of the shock favors a significant increase in separation scales. The character of the limiting streamlines testifies also to the existence of three more singular points (saddles $\boldsymbol{C}_2$, $\boldsymbol{C}_3$, and node $\boldsymbol{N}_2$) near the fin base, apart from the focus $\boldsymbol{F}_1$. These features point to the growth in intensity and scale of the vortex that should appear at point $\boldsymbol{F}_1$.

The above considered structure of the limiting streamlines in the central large-scale separation region in the vicinity of shocks merging for $\beta_1 = \beta_2 = 15°$, $M_\infty = 3.9$ turned out to be identical to that observed in [19, 21, 25] under similar conditions near the fins with flat side surfaces for a larger width of the channel entrance (b = 96.3 mm). A quantitative comparison of obtained pictures of the limiting streamlines with those presented in the above cited works revealed a complete coincidence in scale, shape, and character of the limiting streamlines in this region. This circumstance is extremely important because it proves a good reproducibility and reliability of the typical topological schemes for

considered flows obtained in different experiments. Taking this into account, as well as practically identical values of M_∞, Re_1, β, and boundary layer thickness δ at the channel entrance, the joint analysis of quantitative data obtained in different wind tunnels seems reasonable and important.

Figure 10 shows a comparison of the pressure and heat flux distributions measured along the model centerline with the pressure and skin friction distributions obtained in the above cited works. The origin of x_1 was chosen in the calculated point of the first intersection of shocks. A complete coincidence is observed for the measured pressure distributions (Fig. 10, *a*) from the beginning of the interaction region up to $x_1 = 30$ mm, where the difference in model geometry (the presence or absence of inflections of the side surfaces of the fins) starts to manifest itself. Since the pressure and heat flux measurements in cross-sections are not available in these works, it is not possible to perform a more detailed comparison with results obtained. At the same time, it is seen that an additional heat flux maximum found in these studies corresponds to the position of the node point N_1 (Fig. 10, *a*) with only a tendency to the formation of pressure peak but clearly registered $C_f = 0$ (Fig. 10, *b*). According to the cited works [22, 24, 28], it is supposed that the flow separated at the saddle point C_1, where the skin friction also tends to zero, reattaches at this place on the symmetry axis. The character of heat transfer behind the point N_1 supports the existence of a region of weak decrease in skin friction at $x_1 > 0$ with its subsequent dramatic increase. A comparison of results of different experiments proves their reliability and the correspondence of behavior of various parameters to the typical topological flow scheme considered above. This gives grounds for further use of the considered experimental data as a credible basis for verification of numerical methods.

Situations considered above (Figs. 3, 5, 8, and 9) allow one to analyze the flow topology under the conditions without separation or obvious existence of the central separation region near the first intersection of shocks. The picture of the limiting streamlines obtained for $\beta_1 = \beta_2 = 11°$, $M_\infty = 3$ (Fig. 11) describes the intermediate stage of their development. Under these conditions, the limiting streamlines passing through the throat near the symmetry axis (Fig. 11, *b*) do not show a saddle point associated with separation, but form only a streamwise reattachment line $\boldsymbol{R}_3$, which was also registered in the case of developed separation. The shape of a typical flow region bounded by the merging separation lines $\boldsymbol{S}_1$, $\boldsymbol{S}_3$ and $\boldsymbol{S}_2$, $\boldsymbol{S}_4$ is similar to the early stages of the central separation region (Fig. 8, *b*). A qualitatively similar pattern was obtained in analogous conditions in [12, 17, 18, 28], and in the vicinity of a conical generator of the incident shock [61], where only a node point of a source type was registered. However, these properties are not interpreted in the above works.

The measurements performed in [24, 28] for the case under consideration (Fig. 11) show that the skin friction near the calculated point of the first intersection of shocks is close to zero, which corresponds to incipient separation. On the basis of analysis performed in [7] and generalization of experimental data for various types of separated flows, it can be assumed that the reason for the observed properties of the limiting streamlines are unsteady effects under the conditions of incipience and evolution of an intermittent separation. According to this work, the oil-lampblack mixture at early stages of separation formation for skin friction values close to zero does not feel the influence of

the weak reverse flow region, which exists for a very small period of time, and does not register the arising separation lines or points, penetrating downstream from the interaction region. The separation line appears at a later stage of steady separation development when the reverse flow exists for more than 50% of time, which corresponds to the intermittency factor values $\gamma > 0.5$. As is shown in the cited work, the pressure in the plateau region being formed reaches the values calculated for a developed 2D separation for the first time. The mean pressure distributions along the centerline presented in [22, 28] show that for $M_\infty = 3$ these conditions arise at $\beta_1 = \beta_2 = 11°$. The measurements of fluctuations of the surface pressure and temperature [12, 13] confirm the governing role of significant unsteadiness found in the regions under consideration. Thus, unsteady effects under the conditions of intermittent separation can be the reason for the absence of singular points or the violation of a topological rule valid for steady flows [55, 56] which claims that the saddle points in examined local regions should be compensated by nodes and foci.

The pictures of the limiting streamlines on the side surfaces of the fins for $\beta_1 = \beta_2 = 11°$, $M_\infty = 3$ are determined by shocks twice incident on them (Fig. 11, *a*). The boundary layer separation was found in each interaction region. The first, more extensive separation region is bounded by the lines $\boldsymbol{S}_5$ and $\boldsymbol{R}_5$, which have a saddle $\boldsymbol{C}_1$ and focus $\boldsymbol{F}_1$ closer to the fin base. At the place of secondary interaction the shock initiates on the side surface of the fin only the second low-scale separation region bounded by the lines $\boldsymbol{S}_6$ and $\boldsymbol{R}_6$.

A good agreement of various experimental data obtained in this work and by other authors (Fig. 10) and reliability of the corresponding topological scheme (Fig. 9) demonstrated above for $\beta_1 = \beta_2 = 15°$, $M_\infty = 3.9$ gives grounds for a more critical analysis of today's calculations. The same Figure 10 compares experiments and numerical calculations on the basis of averaged Navier–Stokes equations and various modifications of the k-ε turbulence model, which were performed previously in [39] for the geometry considered in the present work and in [24, 31] for the geometry considered in the cited papers [22, 28]. It can be stated that the calculated and numerical results on pressure distribution are in good agreement (Fig. 10, *a*). The formation of pressure plateau is well predicted, but the downstream pressure level is significantly overestimated. The above mentioned weak decrease in skin friction at $x_1 > 0$ with its subsequent dramatic increase (Fig. 10, *b*) was not predicted by numerical calculations [24] using the k-ε or Baldwin–Lomax turbulence models. Later calculations [31] using the k-ε model demonstrate a qualitative tendency in this region similar to experiment, though do not coincide with experiment within the mentioned accuracy. It should be noted that a satisfactory calculation of the heat transfer distribution has been possible yet only for $\beta_1 = \beta_2 = 7°$ [39, 40]. The considered situation has not been predicted with acceptable accuracy, and there is a tendency to significant overprediction of the heat flux level in comparison with experiment, as the shock strength increases.

4. ASYMMETRIC INTERACTIONS

The pictures of the limiting streamlines on the model surface for the asymmetric interaction case $\beta_1 \times \beta_2 = 7° \times 11°$ and $M_\infty = 3.9$ are shown in Fig. 12. All faces of the first (upper) and second (lower) fins (Fig. 12, *a* and 12, *c*, respectively) are developed into one plane. Like in the case of symmetrical interactions, the flow at the entrance of the channel

formed by two fins (Fig. 12, *b*) is determined by the interaction of glancing shock waves, generated by the fins, and a turbulent boundary layer on the plate, similar to the influence of two isolated fins. The traces of shock waves on the surface, corresponding to inviscid flow are shown hereinafter by dashed lines. The mutual influence of the fins starts to manifest itself when the upstream influence lines $\boldsymbol{U}$ (shown by thin dash-dotted lines in Fig. 12, *b*) merge. These lines correspond to the beginning of streamlines curvature ahead of shock waves. Behind the intersection point of the lines $\boldsymbol{U}$, the separation lines $\boldsymbol{S}_1$ and $\boldsymbol{S}_2$ propagating from the fin vertices form a characteristic throat. Practically all limiting streamlines captured by the channel entrance cross-section are compressed and enter this throat. Secondary separation lines $\boldsymbol{S}_3$ and $\boldsymbol{S}_4$ are formed due to the interaction of intense secondary flows arising at the fin base from the divergence (reattachment) lines $\boldsymbol{R}_1$ and $\boldsymbol{R}_2$. The limiting streamlines themselves diverge to form a streamwise reattachment line $\boldsymbol{R}_3$ that degenerates downstream into a dividing streamline. This line is the boundary between the flows propagating from the fins near the surface. Because of asymmetry of examined configuration, the near-wall flow passing through the throat deflects from the channel centerline (shown by a thin dash-dotted line) to the region of lower pressures near the fin with smaller angle and extends the influence zone of the flow propagating from the lower fin with larger angle. The character of the flow past the side inflection of the lower fin is partly determined by the action of expansion waves propagating from it, which are not shown in the figure for simplicity. These waves favor a more intense motion of the near-wall flow towards the face. As shown in [58, 59], these expansion waves also favor the curvature and amplification of the shock wave of the opposite family, generated by the upper fin, which enters the channel. This effect appreciably stimulates the separation development as this shock interacts with the boundary layer on the side surfaces of the fins in the case of symmetrical interaction.

The character of the limiting streamlines penetrating through the throat above the channel centerline (Fig. 12, *b*) testifies that the considered flow regime under the conditions of asymmetrical interaction is transient in comparison with that registered at a similar Mach number for symmetrical interactions $\beta_1 = \beta_2 = 7°$ and $\beta_1 = \beta_2 = 11°$ (Fig. 5 and 8) . In the first case the streamlines, having passed through the throat without signs of separation, only weakly diverged behind the intersection point of the shock waves. In the second case a saddle point was formed at the throat exit, and a node point was formed slightly downstream. A streamwise reattachment line, similar to $\boldsymbol{R}_3$, emanated from this node point. These features are associated with the existence of a steady separation in the flow passing through the throat. A picture of the limiting streamlines similar to the asymmetrical case under discussion was registered for $\beta_1 \times \beta_2 = 11°$ and $M_\infty = 3$ (Fig. 11). Its features were explained by the influence of unsteady effects inherent in conditions of incipience and evolution of an intermittent separation that comes prior to the steady separation. Under these conditions the oil-lampblack mixture does not feel the influence of the weak reverse flow from the node to the saddle point, which exists for a period of time less than 50%, and does not register the arising separation lines or points. Because of that, the pattern of the limiting streamlines is characterized only by the presence of a streamwise reattachment line. Taking into account similar feature in the case under consideration (Fig. 12, *b*), we can assume the existence of a non-separated flow passing

through the throat or of only an intermittent separation. This assumption is confirmed by the analysis of pressure distribution on the plate surface, presented below.

The pressure distributions along the channel centerline (Fig. 13, *a*), as well as in three cross-sections $x = 46$, 79, and 112 mm (Fig. 14, *a–c*) presented for comparison with data for symmetrical interactions at $\beta_1 = \beta_2 = 7°$ and 11° and Mach number $M_\infty = 3.9$ characterize additional specific features of the examined flow. The relative surface pressure along the channel centerline, which for $\beta_1 \times \beta_2 = 7° \times 11°$ is in the lower fin influence zone (Fig. 12, *b*), increases monotonically (Fig. 13, *a*) from the line $\boldsymbol{U}$ approximately to the intersection point of inviscid shocks (46 mm $< x <$ 100 mm). Its further more intense growth for $x >$ 100 mm is caused by repeated pressure increase behind the crossing shocks. The maximum at point $x \approx 138$ mm corresponds to the reattachment line $\boldsymbol{R}_2$. Then a decrease in pressure is observed up to $x \approx 145$ mm, which is caused by expansion waves propagating from the fin surface inflection, and then the pressure increases again behind the trace of the shock reflected on the fin surface. Approximately the same character is observed in the relative heat transfer coefficient distribution C_q/C_{q1} (Fig. 15, *a*). At the same time, contrary to increasing pressure after the minimum at $x = 145$ mm, the heat transfer continues decreasing in this region.

It should be noted that the heat transfer intensity increases in the region $x \approx 90$–112 mm, as compared with $x \approx 46$–90 mm, on the background of gradually decreasing rate of pressure growth with the formation of a plateau at $x = 90$–100 mm (Fig. 13, *a*). The analysis of the character of limiting streamlines reaching the channel centerline (Fig. 12, *b*) shows that as the streamwise coordinate increases, their length changes differently in these regions. In the region $x \approx 90$–112 mm, due to the existence of the reattachment line $\boldsymbol{R}_2$, which is an effective beginning of secondary flow, the streamline length decreases noticeably faster than for $x \approx 46$–90 mm, where the secondary flow extends from the fin surface. It can be assumed that these features in changing secondary flow length are one of the reasons for a more rapid growth of the heat release in the first region, as compared with the second one.

The relative pressure and heat flux distributions in cross-sections I, II, and III (Fig. 12, *b*) corresponding to $x = 46$, 78, and 112 mm, are illustrated in Figs. 14, *a–c* and 15, *b–d* together with the measurement result for symmetrical configurations $\beta_1 = \beta_2 = 7°$, 11°, and 15°. The vertical sections in figures for pressure distributions show the side faces of the fins. The pressure distribution in cross-section I (Fig. 14, *a*) completely coincides in the asymmetrical case with that obtained on symmetrical models for the corresponding values of angle β up to the point of intersection of the upstream influence lines $\boldsymbol{U}$ in the vicinity of different fins. The positions of minima in cross-section II (Fig. 14, *b*) for an asymmetrical configuration roughly coincide with the secondary separation lines $\boldsymbol{S}_3$ and $\boldsymbol{S}_4$, between which the flow is compressed, like in symmetrical cases. The pressure maximum for $z \approx 4$ mm acquires an intermediate value in comparison with analogous symmetrical situations. Near the corresponding fins for $z >$ 16 mm and $z <$ -11 mm the pressure distributions are the same for symmetrical and asymmetrical configurations. In cross-section III (Fig. 14, *c*) the pressure for an asymmetrical configuration acquires, on average, an intermediate value between the corresponding symmetrical situations. The reattachment line $\boldsymbol{R}_3$ for $z \approx 8.6$ mm corresponds to pressure maximum, and the separation

line S_4 for $z \approx 4$ mm to pressure minimum. It is seen that the pressure distribution in the vicinity of different fins behind the calculated intersection point of inviscid shock waves is almost symmetrical with respect to the minimum point. As it follows from Fig. 15, *b–d*, contrary to the case of symmetrical interaction, the heat transfer intensity increases in the studied regions for $\beta_1 \times \beta_2 = 7° \times 11°$ in the direction from the fin with smaller angle to that with larger angle. A small number of measurement points in the asymmetrical case does not allow for a more detailed analysis of specific features of pressure distributions.

On the basis of above-considered pressure data it is possible to analyze qualitatively the evolution of the near-wall flow passing in an asymmetrical configuration through the throat formed by the limiting streamlines (Fig. 12, *b*) in comparison with a symmetrical case. It follows from results for three cross-sections at $\beta_1 \times \beta_2 = 7° \times 11°$ that the pressure distribution along the centerline shown in Fig. 13, *a* has hardly any differences from the flow passing through this throat and then along the reattachment line $\boldsymbol{R}_3$ in the region 46 mm $< x <$ 100 mm. It is seen that the flow character is very similar to that registered for symmetrical interaction at $M_\infty = 3.9$ and $\beta_1 = \beta_2 = 7°$ (Fig. 5), where no signs of separation were found. In this case the saddle point $\boldsymbol{C}_1$ and node $\boldsymbol{N}_1$ appear in the flow penetrating through the throat only when fin angles are $\beta_1 = \beta_2 = 11°$ (Fig. 8, *b*) when the relative pressure in the region of plateau originating between them (Fig. 13, *a*) reaches the critical value calculated for 2D separation. For the value of M_∞ under consideration it is $P_p/P_1=3$ [7], which corresponds to the formation of steady separation in these conditions.

Thus, the data obtained on pressure distribution confirm the conclusion drawn above on the basis of analysis of the limiting streamlines that there is no steady large-scale separation of flow passing through the throat between the fins in the examined case of asymmetrical interaction. Taking into account higher pressure fluctuations behind the point of crossing shocks, which was registered in [13], a considerable influence of unsteady effects is obvious in this region. They can appreciably affect the topology of the limiting streamlines at the stage of incipience of intermittent separation.

The limiting streamlines on the internal side surfaces of the fins have some features qualitatively similar to those registered for symmetrical configurations (Fig. 12, *a*, *c*). 3D separation regions bounded by the separation lines $\boldsymbol{S}_5$, $\boldsymbol{S}_6$ and reattachment lines $\boldsymbol{R}_5$, $\boldsymbol{R}_6$ are formed on the fin faces at a certain height from their bases near the place of incidence of "inviscid" shock waves propagating after crossing. Separation region length on the upper fin in the interaction region with a more intense shock is much larger than on the lower one. It should be noted that the separation region size can be also determined by a number of other factors to be analyzed below. The curvature of separation and reattachment lines with distance from the plate and an upward flow orientation in separation regions bounded by these lines are caused by tip effects due to finite length of the fins. There is no boundary layer separation on the side surfaces near the plate, and the limiting streamlines are only slightly curved near the boundaries of the system of compression waves shown by dashed lines or near a sequence of shocks formed at the base of shock waves incident to the side faces due to the shock wave/boundary layer interaction on the plate. In the case under consideration their strength is insufficient to cause the boundary layer separation. The character of the limiting streamlines on the upper face (Fig. 12, *a*) points to the existence of singular points: saddle $\boldsymbol{C}_1$ and focus $\boldsymbol{F}_1$.

Topological schemes of the limiting streamlines on various surfaces for $\beta_1 \times \beta_2 = 7° \times 11°$ under the conditions of lower Mach number $M_\infty = 3$ are shown in Fig. 16. The structure of streamlines on the plate (Fig. 16, *b*) is qualitatively similar to that considered above for $M_\infty = 3.9$. At the same time, an increase in inclination angles of shock waves propagating from the fins favors the formation of a throat between the separation lines $\boldsymbol{S}_1$ and $\boldsymbol{S}_2$ closer to the channel entrance. The streamwise reattachment line $\boldsymbol{R}_3$ appears in immediate vicinity of the separation line $\boldsymbol{S}_2$ penetrating through the throat, and the flow effusion in the opposite directions from this line is more intense in comparison with the previous case. The behavior of the limiting streamlines at the beginning of the line $\boldsymbol{R}_3$ does not allow for unambiguous identification of singular points, and the pattern formed resembles those considered above for $M_\infty = 3.9$ and registered for $\beta_1 = \beta_2 = 11°$ and $M_\infty = 3$ (Fig. 11). In the latter case, the absence of conditions for an onset of steady separated flow is justified and it is concluded that, at best, an intermittent separation can exist.

The picture of the limiting streamlines on the face of the upper fin with an angle $\beta_1 = 7°$ at the place of incidence of the shock from the opposite fin with $\beta_2 = 11°$ (Fig. 16, *a*) is qualitatively similar to that registered for $M_\infty = 3.9$. At the same time, a remarkable feature in these conditions is the clearly registered periodic streamwise lines of separation $\boldsymbol{S}$ and reattachment $\boldsymbol{R}$, propagating to the separation region and downstream of it from sequentially positioned saddle $\boldsymbol{C}$ and node $\boldsymbol{N}$ points, which are shown in the enlarged inset of Fig. 16, *a*. Each singular point located on the reattachment line $\boldsymbol{R}_4$ is correlated with an opposite point on the separation line $\boldsymbol{S}_4$. Saddle points are balanced by nodes, which is in agreement with the known topological rule [55, 56]. These features are associated with ordered vortex structures formed in the boundary layer, similar to Taylor–Goertler vortices, and they were previously encountered in various cases of shock/boundary layer interaction [9, 62–64]. In the case under consideration, signs of these vortices are clearly observed within the streamwise convex part of the reattachment line $\boldsymbol{R}_4$, and their step if 3-5 mm (Fig. 16, *a*). For simplicity, the signs of these structures are shown in the figure only at the boundaries of the mentioned region.

Two separation regions bounded by the lines $\boldsymbol{S}_5$, $\boldsymbol{R}_5$ and $\boldsymbol{S}_6$, $\boldsymbol{R}_6$ are registered on the face of the lower fin at the place of incidence of two shock waves (Fig. 16, *c*). These separation regions are substantially smaller in size than those on the upper surface. Very weak signs of periodic streamwise vortices propagating downstream were observed only behind the convex part of the line $\boldsymbol{R}_5$.

An increase of the lower fin angle for $\beta_1 \times \beta_2 = 7° \times 15°$ and $M_\infty = 3.9$ favors the increase in flow asymmetry (Fig. 17). Its typical feature, as compared with previously considered, is the formation of the reattachment line $\boldsymbol{R}_3$ on the plate in the region of secondary flow propagating from the lower fin (Fig. 17, *b*). It is essential that clear patterns of the limiting streamlines obtained in these conditions do not reveal the signs of singular points upstream of this reattachment line, which are associated with an onset of separation. The pressure distribution along the channel centerline together with the data for symmetrical interactions with $\beta_1 = \beta_2 = 7°$ and 15° and similar Mach number (see Fig. 13, *b*), which are presented for comparison, characterizes some additional features of the flow under consideration. In accordance with Fig. 17, *b*, the centerline is in the influence region of the flow propagating from the lower fin with larger angle. As the upstream influence line $\boldsymbol{U}$ is achieved at $x \approx 40$ mm, the pressure in the interaction region starts to

increase and in the region $x \approx 50$–80 mm becomes almost constant and equal to $P/P_1 =$ 1.9–2.0. This value corresponds to the calculated pressure value in the plateau region $P_p/P_1 = 1.9$ in the separation region and near the lower isolated fin, which can be calculated within the framework of 2D analogies [7] along the Mach number normal component to the inviscid shock wake $M_e = M_\infty \cdot \sin\varepsilon = 1.8$ where ε is the shock angle with the free-stream direction. Then the pressure increases again and reaches the maximum value at $x \approx 110$ mm near the reattachment line $\boldsymbol{R}_2$. Its further decrease to a minimum at $x \approx 133$ mm is caused by the influence of expansion waves induced by the inflection of the side surface of the lower fin. The next intense pressure growth with another maximum is observed at $133 < x < 143$ mm near the intersection of separation $\boldsymbol{S}_5$ and reattachment $\boldsymbol{R}_5$ lines formed on the plate (Fig. 17, *b*). They obviously arise due to a shock wave reflected on the upper fin surface and propagating to this region. The position of this shock is different from that typical of inviscid flow and determined by viscous-inviscid interaction effects. The behavior of the relative heat transfer coefficient along the channel centerline in this situation (Fig. 15, *a*) is in qualitative agreement with pressure evolution, and its level for $x \approx 60$–115 mm is appreciably higher than for the case $\beta_1 \times \beta_2 = 7° \times 11°$.

The pressure distributions for the analyzed situation ($\beta_1 \times \beta_2 = 7° \times 15°$, $M_\infty = 3.9$) in cross-sections I, II, and III for x = 46, 78, and 112 mm are presented in Fig. 14, *d–f* together with the measurement results for symmetrical configurations $\beta_1 = \beta_2 = 7°$ and 15° under similar conditions. The pressure distribution in cross-section I (Fig. 14, *d*) located behind the intersection point of the upstream influence lines $\boldsymbol{U}$ for $6 < z < -6$ mm coincides with the corresponding symmetrical cases $\beta_1 = \beta_2 = 7°$ and 15°. In cross-section II (Fig. 14, *e*) there is a pressure maximum on the reattachment line $\boldsymbol{R}_3$ at $z \approx 12$ mm, and the flow region bounded by the separation lines $\boldsymbol{S}_3$ and $\boldsymbol{S}_4$ ($5 < z < 20$ mm) is characterized by an elevated pressure level. Approaching the reattachment line $\boldsymbol{R}_2$ near the lower fin base ($z < -4$ mm) the pressure dramatically increases. For an asymmetrical interaction, the pressure level in cross-section II take intermediate values in comparison with those typical of symmetrical configurations with $\beta_1 = \beta_2 = 7°$ and 15°. In cross-section III further from the pressure maximum near the reattachment line $\boldsymbol{R}_2$ ($z \approx 0$, Fig. 17, *b*) the pressure level dramatically decreases as approaching the lower fin ($z < 0$) due to expansion waves propagating from the side surface inflection (Fig. 14, *f*). The flow effusion at $z > 0$ is accompanied by pressure decrease to a minimum at $z \approx 10$ mm and its secondary growth in the direction towards the upper fin base, where the separation line $\boldsymbol{S}_4$ is formed at $z \approx 11$ mm. Like pressure, the relative heat flux distributions for $\beta_1 \times \beta_2 =$ 7°×15° in cross-sections I-III are strongly asymmetrical, and their level increases in the direction from the fins with smaller angle to that with larger angle (Fig. 15, *b–d*) within the interval between the typical values for symmetrical interaction $\beta_1 = \beta_2 = 7°$ and 15°. A limited number of measurement points does not allow a more detailed analysis of specific features of these distributions.

An additional analysis of the limiting streamlines on the plate in the examined situation (Fig. 17, *b*) together with the above data on pressure distribution allows one to explain the absence of singular points, associated with separation and subsequent reattachment, immediately ahead of the reattachment line $\boldsymbol{R}_3$. It is seen that this reattachment line is formed in the secondary flow propagating from the lower fin behind

the separation line S_2 on the background of high initial pressure $P/P_1 \approx P_p/P_1 = 2.0$ typical of it. The distribution of the current relative pressure P/P_p between cross-sections I-III (x = 40–110 mm) for a chosen characteristic limiting streamline, whose continuation is the reattachment line R_3, is practically coincident with that registered for symmetrical interaction for $\beta_1 = \beta_2 = 7°$ shown in Fig. 13, *b*). This weak adverse pressure gradient is insufficient to cause the boundary layer separation, contrary to cases $\beta_1 = \beta_2 = 11°$ (Fig. 13, *a*) and $\beta_1 = \beta_2 = 15°$ (Fig. 13, *b*), for which a sequence of saddle C_1 and node N_1 points was registered. It can be also assumed that the expected high level of turbulent fluctuations in the secondary flow propagating from the fin tip behind the line S_2 also hinders the onset of separation and singular points.

The topology of the limiting streamlines on the side surfaces of the fins in this situation (Fig. 17, *a*, *c*) is determined by the interaction of shock waves of various strength with boundary layers developed on them. A stronger shock incident onto the face of the upper fin (Fig. 17, *a*) initiates a large-scale separation region bounded by the lines S_6 and R_6. The separation line S_6 extends almost to the plate, since the intensity of disturbances near the lower fin base becomes sufficient to cause separation. In addition to previously noted singular points C_1 and F_1, a node N and saddle S were found. Specific features of the flow around these points are shown in the enlarged fragment in Fig. 17, *a*. Very weak signs of periodic streamwise vortices with a step of 5.5–6 mm were registered behind the line R_6. They are not shown for simplicity. A local separation is formed between the lines S_7 and R_7, where a weaker shock from the leading edge of the upper fin in incident onto the lower surface (Fig. 17, *c*). It should be noted, however, that the formation of this region is also determined, apparently, by the influence of rather strong disturbances propagating from the upper surface, which arise in the course of viscous-inviscid interaction on this surface. As noted above, they are the reason for the appearance of the separation line S_5 on the plate. The signs of streamwise periodic vortices downstream of this local separation region are very difficult to distinguish.

The topological schemes of the limiting streamlines for $\beta_1 \times \beta_2 = 7° \times 15°$ and Mach number $M_\infty = 3$ are presented in Fig. 18. In this case the flow on the plate (Fig. 18, *b*) is more complex than in the above cases. The scale of the characteristic region bounded by the converging lines S_1, S_2 and additional separation line S_4 substantially increases. The secondary flow from the lower fin penetrating into this region is decelerated to form the saddle point C_1 and separation lines S propagating to the opposite sides from it. The fragment in Fig. 18, *c* shows these features in more detail. They point to the existence of steady separation. The foci F_1 and F_2 are formed in the reverse flow region propagating from the source N_1. The separation line S_5 with saddle point C_2 appears as the result of interaction of the flow propagating from the source and a narrow stream along the channel that penetrates above the focus F_1. This saddle point separates oppositely directed flows along the separation line. An additional saddle point C_3 is located behind the focus F_2. It is of interest that the topological rule mentioned previously is also valid for the region under study, whereby the number of saddle points should correspond to the sum of nodes and foci. The observed topological features characterized by the emergence of separation region with two foci are inherent in considered flows at the stage of channel choking. Similar features are revealed in the pattern of the limiting streamlines obtained in [28] for symmetrical interaction with $\beta_1 = \beta_2 = 13°$ and $M_\infty = 3$.

The qualitative character of the limiting streamlines at the face of the upper fin (Fig. 18, *a*) is similar to that observed for $M_\infty = 3.9$ (Fig. 17, *a*). The size of the separation region limited by the lines $\boldsymbol{S}_7$ and $\boldsymbol{R}_7$ slightly increases. Comparatively weak signs of periodic streamwise vortices (not shown) with a step of 11.5–13 mm are found behind the reattachment line $\boldsymbol{R}_7$ between the streamwise limiting streamlines plotted in the figure. A remarkable feature is a significant growth of separation scale at the face of the lower fin between the lines $\boldsymbol{S}_9$ and $\boldsymbol{R}_9$ in the region of interaction with a weaker shock from the upper fin (Fig. 18, *c*) in comparison with the situation for $M_\infty = 3.9$ (Fig. 17, *c*). Obviously, the development of large-scale separation in this region, like on the upper face (Fig. 18, *a*), points to approaching channel choking. An intense growth of separation regions on the surfaces, due to their expulsion effect, favors an additional flow compression in the channel and the growth of intensity of the shocks developed there, thus approaching the channel choking. Along with the above features, a local separation region limited by the lines $\boldsymbol{S}_{10}$ and $\boldsymbol{R}_{10}$ (Fig. 18, *c*) is formed at the place of incidence of the shock reflected on the side surface of the upper fin onto the low fin.

An increase of the upper fin angle for $\beta_1 \times \beta_2 = 11° \times 15°$ and $M_\infty = 3.9$ alters significantly the structure of the limiting streamlines (Fig. 19) in comparison with the above considered case $\beta_1 \times \beta_2 = 7° \times 15°$ (Fig. 17). In this regime the asymmetry of the pattern formed on the plate slightly decreases (Fig. 19, *b*). At the same time, its appreciable effect manifests itself in the region slightly above the channel centerline (dash-dotted line). Specific features of the flow penetrating through the throat formed by the lines $\boldsymbol{S}_1$ and $\boldsymbol{S}_2$ are very similar to those registered for symmetrical interaction with $\beta_1 = \beta_2 = 11°$, $M_\infty = 3.9$ (Fig. 8). A typical feature is the formation of the central separation region bounded by the line $\boldsymbol{S}$ emanating from the saddle point $\boldsymbol{C}_1$, and also the node $\boldsymbol{N}_1$, which is the origin of the streamwise reattachment line $\boldsymbol{R}$ (see the enlarged fragment in Fig. 19, *c*). A small initial asymmetry is the reason for the lower part of the region under consideration to be formed under the conditions of elevated pressure and its lower gradients within the limits of secondary flow propagating from the lower fin. As shown above, these conditions are more favorable and prevent the separation. This explains the observed suppression of the signs of separation in the lower part of the examined region, which is an additional source of flow asymmetry revealed in this case. As it follows from the picture of the limiting streamlines, the disturbances reflected on the lower fin surface are rather intense to cause separation on the plate along the separation line $\boldsymbol{S}_5$.

The pressure distributions along the channel centerline (Fig. 13, *c*), and also for cross-sections I, II, and III (Fig. 14, *g–i*), together with the data presented for comparison and obtained in similar conditions for symmetrical interactions with $\beta_1 = \beta_2 = 7°$ and 15°, characterize some additional features of the flow under study. In accordance with Fig. 19, *b*, the central line is in the influence region of the flow propagating from the lower fin with larger angle. The pressure levels and gradients observed along this line are higher than in the case $\beta_1 = \beta_2 = 11°$, wherein the saddle point $\boldsymbol{C}_1$ and node $\boldsymbol{N}_1$ caused by the formation of the central separation region were registered. Taking into account the pressure distributions in cross-sections (Fig. 14, *g–i*), it is easy to see that the flow passing through the throat between the lines $\boldsymbol{S}_1$ and $\boldsymbol{S}_2$ (Fig. 19, *b*) overcomes even larger pressure gradients. Thus, it is not accidental that the signs of separation and similar singular points are found there. As it follows from Fig. 14, *g*, in the considered situation,

when approaching the fins, the pressure distribution in cross-section I begins to coincide from a certain moment with that typical of the corresponding symmetrical interactions. The region of local pressure increase in cross-section II for $4 < z < 11$ mm (Fig. 14, *h*) corresponds to the above described separation region formed above the channel centerline (Fig. 19, *b*). In cross-section III the pressure decreases from the reattachment line $\boldsymbol{R}_2$ ($z \approx$ 0–3 mm) towards the lower fin ($z < 0$) behind the inflection of its side face and increases towards the upper fin.

The limiting streamlines on the upper fin (Fig. 19, a) reveal a separation region bounded by the lines $\boldsymbol{S}_6$ and $\boldsymbol{R}_6$ at the place of incidence of the shock from the lower fin near the side surface inflection. It is remarkable that the separation length under these conditions decreases in comparison with the previously considered case $\beta_1 \times \beta_2 = 7° \times 15°$ (Fig. 17, *a*) when the shock was incident significantly higher than the surface inflection. This effect is not incidental and is in line with the results of [65, 66]. Following these papers, a gradual suppression of separation to a certain minimum scale as the shock wave approaches the surface inflection occurs under the action of expansion waves. A gradual increase of suppressed separation length takes place as the shock wave passes through the inflection and moves away from it. Obviously, in the above situations when the separation regions are formed near surface inflections (Figs. 16, *c*, 17, *c*, 18, *c*), their dimensions are determined by a similar influence, along with other factors. Among these factors there is relaminarization of the near-wall flow in expansion waves, which can favor the growth of separation length [60], and the above mentioned effects of viscous-inviscid interaction caused by additional flow compression in the channel due to the expulsion action of separation regions.

Apart from these features, the signs of developing periodic vortices (not shown for simplicity of the picture) with a step of 4–5.5 mm are found behind the line $\boldsymbol{R}_6$ in the analyzed situation (Fig. 19, *a*), like in some previously considered cases. The growth of intensity of the shock propagating from the upper fin leads to an increase of separation length between the lines $\boldsymbol{S}_7$ and $\boldsymbol{R}_7$ on the lower face (Fig. 19, *c*) in comparison with the case shown in Fig. 17, *c*. The number and type of singular points ($\boldsymbol{C}_3$, $\boldsymbol{C}_4$, $\boldsymbol{F}_2$, $\boldsymbol{N}_3$) is in line with topological rules [55, 56]. The step of observed periodic streamwise vortices behind the line $\boldsymbol{R}_7$ lies within 2.7–4 mm.

A decrease of the Mach number to $M_\infty = 3$ in the case $\beta_1 \times \beta_2 = 11° \times 15°$ leads to characteristic changes in the topology of the limiting streamlines associated with the development of channel choking (Fig. 20). The main features in these conditions are the upstream displacement of the separation lines $\boldsymbol{S}_1$ and $\boldsymbol{S}_2$ emanating from the saddle point $\boldsymbol{C}_1$ (Fig. 20, *b*) towards the channel entrance, and also the formation of two foci $\boldsymbol{F}_1$, $\boldsymbol{F}_2$ and the saddle point $\boldsymbol{C}_2$ located downstream. A similar structure was observed for a complete channel choking (Fig. 4) when the separation lines $\boldsymbol{S}_1$ and $\boldsymbol{S}_2$ appeared at some distance upstream of the fins, and the flow from recirculation region passed in the transverse direction between these lines and the leading edges of the fins. There is no such an overflow in the examined situation, and the central region is bounded by the nodes $\boldsymbol{N}_1$, $\boldsymbol{N}_2$ and saddle points $\boldsymbol{C}_3$, $\boldsymbol{C}_4$ located behind them. Specific features of the limiting streamlines in the vicinity of these nodes and saddle points are qualitatively analogous to those shown in the enlarged fragment (Fig. 17, *a*). In the considered case of

developed separation (Fig. 20, *b*) the saddle points are balanced by nodes and foci in accordance with the topological rule.

Vast separation regions between the lines S_3 and R_3, S_3 and R_3 are formed on the side surfaces of the upper and lower fins (Fig. 20, *a*, *c*), with an intense upward flow. Additional lower-scale separation regions arise downstream between the lines S_4 and R_4, S_5 and R_5. The dashed lines on the side surfaces show the positions of expected shocks whose influence is felt in the limiting streamlines behavior. Obviously, the gas dynamic flow structure formed in this case, like in previously analyzed situations, is rather complex and allows for the existence of regions of both Mach and regular interactions of shock waves. Its detailed description requires a special additional study.

Considered wide experimental data [69, 70] has been used as the basis for verification of numerical methods developed in Air Force Research Laboratory Write-Patterson AFB, Ohio, USA. The capability for numerical simulation of symmetric and asymmetric shock waves/turbulent boundary layer interactions using the Reynolds averaged Navier-Stokes equations and the k–ε turbulence model at $M_\infty = 3.9$ and different values of the fins inclination angles was demonstrated in [71, 72]. The computations have been employed successfully to propose a model which is valid under a wide range of interaction strengths and asymmetries. The various regimes identified previously for symmetric interactions have been shown to persist in asymmetric interactions and provide a unified understanding of the flowfield. Nevertheless it is necessary to note, that for strong interaction ($\beta_1 = \beta_2 = 15°$), the experimental surface flow pattern, while in agreement with the major features observed in computations, differ in some topological detailes. The prediction of the sidewall/shock-vortex interaction has been improved through the use of a modification which inhibits transition of the sidewall boundary layer. An understanding of the flow structure was shown to be an important component of quantitative turbulence model evaluation. The computed surface pressure displayed good agreement with experiment. The computations of the heat transfer and comparison with experimental data would be important on the next stage of the investigation.

5. CONCLUSIONS

Systematic experimental studies of 3D interaction of a turbulent boundary layer with a sequence of symmetric and asymmetric crossing swept shocks and expansion waves have been conducted. New data on the structure of the limiting streamlines, surface pressure and heat transfer distributions have been obtained. New information allows one to refine considerably the topological features of such flows at various stages of their development and forms the basis for verification of today's numerical methods.

A good reproducibility of specific features of the considered flows in different experiments has been demonstrated. Specific topological features of 3D separation in the vicinity of crossing shocks under the conditions of absence and development of channel choking have been demonstrated and analyzed. On the basis of obtained results and generalization of previous studies, the unsteady effects on the experimentally registered

picture of the limiting streamlines at the stage of separation incipience have been explained.

It is shown that the examined class of assymmetric interaction flows has much more versatile topological forms, as compared with symmetric interactions. It has been found that increasing asymmetry of the considered configuration favors the displacement of the central separation region on the plate to the region of secondary flow from the fin, which develops under elevated pressure, and the suppression of separation due to decreasing local pressure gradient. When approaching the channel choking regime, an intense growth of separation region scale on the channel surfaces is observed, as well as the change in flow topology in this region on the plate with the formation of two foci.

Under the conditions of limited 3D flow in the channel, like in the flow around open 2D configurations, the separation suppression is observed when the shock waves fall in the vicinity of inflections of its side surfaces.

Considered wide experimental data has been used for verification of numerical computations, developed in Air Force Research Laboratory Write-Patterson AFB, Ohio, USA on a basis of the Reynolds averaged Navier-Stokes equations and the k–ε turbulence model [71, 72]. It was demonstrated that the computational model is valid under a wide range of interaction strengths and asymmetries and the computed surface pressure as well as limiting streamlines properties displayed good agreement with experiment. Nevertheless it is necessary to note, that for strong interaction, the experimental surface flow pattern, while in agreement with the major features observed in computations, differ in some topological detailes.

The prediction of the sidewall/shock-vortex interaction has been improved through the use of a modification which inhibits transition of the sidewall boundary layer. The computations of the surface heat transfer and comparison with experimental data are important in future.

A collaborative experimental and computational study of the crossing shock wave/turbulent boundary layer interaction at hypersonic Mach numbers may be considered as the next important stage of future program.

ACKNOWLEDGEMENTS

The authors wish to express their sincere gratitude to Doctors D.V.Gaitonde, M.R.Visbal and J.S.Shang (Air Force Research Laboratory Wright-Patterson AFB, Ohio, USA) for collaboration in a framework of this program. We would like also to acknowledge the assistance of Dr. M.S.Maurice. The studies were supported by EOARD Contract F61708-97-W0136 (monitor: Dr. C.Raffoul).

References

1. Proceedings of the AFOSR Workshop on Fluid Dynamics of High Speed Inlets / Eds. Sakel L., Knight D., Zheltovodov A. - Department of Mechanical and Aerospace Engineering, Rutgers University, New Brunswick, NJ, May, 1994.
2. Gutov B.I., Zatoloka V.V., Numerical and experimental study of new convergent inlets with 3D flow combinations // Preprint ITAM SB RAS No.30-83. Novosibirsk, 1983. 53 p.
3. Gogish L.V., Zheltovodov A.A., Kurmashev R.Kh., Lokotko A.V., Kharitonov A.M., The influence of entrance conditions of a rectangular channel on the structure of internal supersonic flow // Preprint ITAM SB RAS No.13-90. Novosibirsk, 1990. 39 p. (in Russian)
4. Settles G.S., Dolling D.S. Swept shock wave/boundary layer interactions – tutorial and update // AIAA Paper. 1990. № 0375. 29 p.
5. Knight D.D. Numerical solution of 3-D shock wave turbulent boundary layer interactions // AGARD Special Course on Shock Wave / Turbulent Boundary Layer Interactions in Supersonic and Hypersonic Flows, Advisory Group for Aerospace Research and Development, August 1993. AGARD Report. 1993. № 792. P. 1-34.
6. Delery J., Panaras A.G. Shock wave/boundary layer interactions in high Mach number flows // Hypersonic Experimental and Computational Capability, Improvement and Validation. AGARD-AR-319. 1996. Vol. 1. P. 2-1 – 2-61.
7. Zheltovodov A.A. Shock waves/turbulent boundary layer interactions - fundamental studies and applications // AIAA Paper. 1996. № 1977. 27 p.
8. Gogish L.V., Stepanov G.Yu. Separation and Cavitation Flows. Moscow, Nauka, 1990. 384 p. (in Russian)
9. Borovoi V.Ya., Gas Flow and Heat Transfer in Shock Wave/Boundary Layer Interaction Regions. Moscow, Mashinostroenie, 1983. 141 p. (in Russian)
10. Marvin J.G. Perspective on computational fluid dynamics validation // AIAA J. 1995. Vol. 33. № 10. P. 1778-1787.
11. Mee D.J., Stalker R.J., Stollery J.L. Glancing interaction between single and intersecting oblique shock waves and a turbulent boundary layer // J. of Fluid Mech. 1986. Vol. 170. P. 411-433.
12. Batcho P.F., Ketchum A.C., Bogdonoff S.M., Fernando E.M. Preliminary study of the interactions caused by crossing shock waves and a turbulent boundary layer // AIAA Paper. 1989. № 0359. 11 p.
13. Poddar K., Bogdonoff S.M. A study of unsteadiness of crossing shock wave turbulent boundary layer interactions // AIAA Paper. 1990. № 1456. 13 p.
14. Narayanswami N., Knight D., Bogdonoff S., Horstman C. Interaction between crossing oblique shocks and turbulent boundary layer // AIAA J. 1992. Vol. 30. № 8. P. 1945-1952.
15. Kussoy M.I., Horstman K.C. Intersecting shock wave/turbulent boundary layer interactions at Mach 8.3 // NASA TM. 1993. № 103909. 46 p.

16. Bogdonoff S.M., Stokes W.L. Crossing shock wave turbulent boundary layer interactions - variable angle and shock generator length geometry effects at Mach 3 // AIAA Paper. 1992. № 0636. 20 p.
17. Garrison T.J., Settles G.S. Flowfield visualization of crossing shock wave/boundary layer interactions // AIAA Paper. 1992. № 750. 10 p.
18. Garrison T.J., Settles G.S., Narayanswami N., Knight D. Interaction strength and model geometry effects on the structure of crossing-shock wave/turbulent boundary-layer interactions // AIAA Paper. 1992. № 3670. 12 p.
19. Davis D. O., Hingst W. R. Surface and flow measurements in a symmetric crossing shock waves/turbulent boundary layer interaction // AIAA Paper. 1992. № 2634. 18 p.
20. Garrison T., Settles G., Narayanswami N., Knight D. Structure of crossing shock wave/turbulent boundary layer interactions // AIAA J. 1993. V. 31. № 12. P. 2204-2211.
21. Narayanswami N., Knight D.D., Bogdonoff S.M., Horstman C.C. Crossing shock wave/turbulent boundary layer interactions // AIAA Paper. 1991. № 649. 23 p.
22. Garrison T.J., Settles G.S. Interaction strength and model geometry effects on the structure of crossing shock wave/turbulent boundary layer interactions // AIAA Paper. 1993. № 0780. 12 p.
23. Kussoy M.I., Horstman K.C., Horstman C.C. Hypersonic crossing shock wave/turbulent boundary layer interactions // AIAA J. 1993. Vol. 31. № 12. P. 2197-2203.
24. Garrison T.J., Settles G.S., Narayanswami N., Knight D.D. Laser interferometer skin-friction measurements of crossing shock wave/turbulent boundary layer interactions // AIAA J.1994. Vol. 32. № 6. P. 1234-1241.
25. Gaitonde D., Shang J. Calculation on a double fin turbulent boundary layer interaction // AIAA Paper. 1993. № 3432. 13 p.
26. Narayanswami N., Horstman C.C., Knight D.D. Numerical simulation of crossing shock/turbulent boundary layer interaction at Mach 8.3 - comparison of zero- and two-equation turbulence models // AIAA Paper. 1993. № 0779. 17 p.
27. Narayanswami N., Horstman C.C., Knight D.D. Computation of crossing shock/turbulent boundary layer interaction at Mach 8.3 // AIAA J. 1993. Vol. 31. №8. P. 1369-1376.
28. Garrison T. The interactions between crossing shock waves and a turbulent boundary layer // Ph. D. Thesis, Dept. of Mechanical Engineering, Pennsylvania State Univ., PA, 1994.
29. Garrison T.J., Settles G.S., Narayanswami N., Knight D.D., Horstman C.C. Comparison of flowfield surways and computations of a crossing shock wave/boundary layer interaction // AIAA Paper. 1994. № 2273. 12 p.
30. Bardina J.E., Coakley T.J. Three-dimensional Navier-Stokes simulations with two-equation turbulence models of intersecting shock waves/turbulent boundary layer at M=8.3 // AIAA Paper. 1994. № 1905. 11 p.

31. Gaitonde D., Shang J.S. The structure of a turbulent double fin interaction at Mach 4 // AIAA Paper. 1994. № 2810. 15 p.
32. Bardina J.E., Coakley T.J. The structure of intersecting shock waves/turbulent boundary layer interaction flow // AIAA Paper. 1995. № 2215. 11 p.
33. Gaitonde D., Shang J.S., Visbal M. Structure of a double fin interaction at high speed // AIAA J. 1995. Vol. 33. № 2. P. 193-200.
34. Gaitonde D., Shang J.S. On 3-D shock wave/turbulent boundary layer interactions at Mach 4 // AIAA Paper. 1996. № 0043. 16 p.
35. Zheltovodov A.A., Maksimov A.I., Shevchenko A.M., Vorontsov S.S., Knight D.D. Experimental study and computational comparison of crossing shock wave/turbulent boundary layer interaction // Proc.: Int. Conf. on the Methods of Aerophys. Research, August 22-26, 1994, Novosibirsk, Russia. Novosibirsk, 1994. Part 1. P. 221-230.
36. Zheltovodov A.A., Maksimov A.I., Shevchenko A.M. The study of three-dimensional separation of single and crossing shock waves with turbulent boundary layer // Mathematical Modeling, Aerodynamics, and Physical Gas Dynamics /ed. V.M.Fomin. Novosibirsk, 1995. P. 121-132 (in Russian)
37. Knight D.D., Garrison T.J., Settles G.S., Zheltovodov A.A., Maksimov A.I., Shevchenko A.M., Vorontsov S.S. Asymmetric crossing shock wave/turbulent boundary layer interaction // AIAA J. 1995. Vol. 33. № 12. P. 2241-2249.
38. Knight D.D., Garrison T.J., Settles G.S., Zheltovodov A.A., Maksimov A.I., Shevchenko A.M., Vorontsov S.S. Asymmetric crossing shock wave/turbulent boundary layer interaction // AIAA Paper. 1995. № 0231. 18 p.
39. Gnedin M., Knight D., Zheltovodov A., Maksimov A., Shevchenko A., Vorontsov S. 3-D crossing shock wave - turbulent boundary layer interaction // AIAA Paper. 1996. № 96-2001. 18 p.
40. Gnedin M., Zha G., Knight D., Zheltovodov A., Maksimov A., Shevchenko A., Vorontsov S. 3-D crossing shock wave - turbulent boundary layer interaction // Proc.: Int. Conf. on the Methods of Aerophys. Research, September 2-6, 1996, Novosibirsk, Russia. Novosibirsk, 1996. Part 1. P. 114-122.
41. Zha G.Ch., Knight D. Computation of 3D asymmetric crossing shock wave/turbulent boundary layer interaction using a full Reynolds stress equation turbulence model // AIAA Paper. 1996. № 0040. 16 p.
42. Smith B.R. Prediction of hypersonic shock-wave/turbulent boundary-layer interactions // J. of Spacecraft and Rockets. 1996. Vol. 33. № 5. P. 614-619.
43. Garrison T.J., Settles G.S., Horstman C.C. Measurements and computation of the triple shock wave/turbulent boundary layer interaction // AIAA Paper. 1994. № 2274. 11 p.
44. Lighthill M.J. On boundary-layers and upstream influence : Part II - Supersonic flows without separation // Proc. of the Royal Society. 1953. Vol. A217. P. 478-507.
45. Kornilov V.I. Development of 3D flow in a corner configuraiton initiated by an impinging oblique shock wave // Mathematical Modeling, Aerodynamics and Physical Gas Dynamis, ed. V.M.Fomin. Novosibirsk, 1995. P. 79-89 (in Russian)

46. Kornilov V.I. Formation peculiarities of the flow structure in a corner comfiguration under the conditions of interaction with the impinging incident shock wave // Thermophysics and Aeromechanics. 1995. Vol. 2. No. 2. P. 95-104 (in Russian)
47. Kornilov V.I. Interaction of an external incident oblique shock wave with the boundary layer in a rectabgular half-channel // Thermophysics and Aeromechanics. 1995. Vol. 2. No. 3. P .191-202 (in Russian)
48. Lokotko A.V., Shushpanov M.M. Thermal wind tunnel T-333 // Aerophysical Research.- Novosibirsk, 1972. P. 18-20 (in Russian)
49. Zaikovsky V.N., Zaulichny E.G., Melamed B.M., Senov Yu.M. An experimental study of local heat transfer coefficients on the walls of a valve device // J. Appl. Mech. Tech. Phys. - 1982. No. 2. P. 52-58 (in Russian)
50. Zheltovodov A.A., Regimes and properties of 3D separated flows initiated by oblique shock waves // J. Appl. Mech. Tech. Phys. 1982. No. 3. P. 116-123.
51. Zheltovodov A.A., Maksimov A.I., Shilein E.Kh., Development of turbulent separated flows in the vicinity of glancing shock waves // Interaction of Complex 3D Flows. ITAM SB RAS, Novosibirsk, 1987. P. 67-91 (in Russian)
52. Zheltovodov A.A., Dvorzhak R., Shafarzhik P., Specific features of the interaction of shock waves with a turbulent boundary layer at trans- and supersonic velocities // Izv. SO AN SSSR, Ser. tech. nauk. 1990. Iss. 6. P. 31-42 (in Russian)
53. A.A.Zheltovodov, Physical features and some properties of 2D and 3D separated flows // Izv. AN SSSR, Ser. Mekhanika Zhidkosti i Gaza. 1979. No. 3. P. 42-49.
54. Wang L., New achievements in the study of open separation // Three-Dimensional Turbulent Boundary Layers / ed. H. Fernholtz and E. Krause. - Spinger-Verlag, New-York 1982.
55. Delery J. M. Physics of vortical flows // J. of Aircraft. 1992. Vol. 29. № 5. P. 856-876.
56. Tobak M., Peake D.J. Topology of three dimensional separated flows // Annual Review of Fluid Mech. 1982. Vol. 14. P. 61-85.
57. Trofimov V.M., Shtrekalkin S.I., The study of the flow structure and heat transfer intensity in the vicinity of an expanding step on a plate // Sib. Fiz.-Tekh. Zhurn. 1992. Iss. 6. P. 42-47 (in Russian)
58. Darian A., Daso E.O. Analysis of shock interactions and flow structure in high speed inlets // AIAA Paper. 1990. № 2132. 10 p.
59. Li H., Ben-Dor G. Oblique-shock/expansion-fan interaction – analitical solution // AIAA J. 1996. Vol. 34. № 2. P. 418-421.
60. Zheltovodov A.A., Shilein E.Kh., Horstman C.C., Development of separation under the interaction of shock wave with a turbulent boundary layer disturbed by expansion waves // J. Appl. Mech. Tech. Phys. 1993. No. 4. P. 58-68 (in Russian)
61. Glagolev A.I., Zubkov A.I., Taabaldiev K.A., Separated flows formed by the interaction of a shock wave from a conical obstacle with internal compression and the boundary layer // Izv. AN SSSR, Ser. Mekhanika Zhidkosti i Gaza. 1995. No. 1. P. 147-151 (in Russian)

62. Zheltovodov A.A., Shilein E.Kh., Yakovlev V.N. Development of turbulent boundary layer under the conditions of mixed interaction with shock and expansion waves // Preprint ITAM SB RAS No. 28-83. Novosibirsk, 1990. 51 p.
63. Glotov G.F., Moroz E.K. Streamwise vortices in supersonic flows with separation regions // Uch. Zap. TsAGI. 1977. Vol. VIII. No. 4. P. 44-53.
64. Brazhko V.N. Some features of transverse periodicity of the flow in 2D supersonic separation regions // Uch. Zap. TsAGI. 1991. Vol. XXII. No. 4. P. 25-32.
65. Chew Y.T. Shockwave and boundary layer interaction in the presence of an expansion corner // Aeronautical Quarterly. 1979. Vol. XXX. Part 3. P. 506-527.
66. Hawbold R.J., Sullivan P.A., Gottlieb J.J. Interactions between shock wave and hypersonic laminar boundary layer near convex corner // J. Spacecraft and Rockets.1995. Vol. 32. № 5. P. 783-790.
67. Weinbaum S., Garvine R.W. On the two-dimensional viscous counterpart of the one-dimensional sonic throat // J. Fluid Mech. 1969. Vol. 39. Part 1. P. 57 - 85.
68. Chien K.-Y. Predictions of channel and boundary layer flows with a low Reynolds number turbulence model // AIAA J. 1982. Vol. 20. №1. P. 33-38.
69. Zheltovodov A.A., Maksimov A.I., Shevchenko A.M. Topology of three-dimensional separation under the conditions of symmetric crossing shocks and expansion waves/turbulent boundary layer interaction // Thermophysics and Aeromechanics. 1998. Vol. 5. (to be published).
70. Zheltovodov A.A., Maksimov A.I., Shevchenko A.M., D.D.Knight. Topology of three-dimensional separation under the conditions of asymmetric crossing shocks and expansion waves/turbulent boundary layer interaction // Thermophysics and Aeromechanics. 1998. Vol. 5. (to be published).
71. Gaitonde D.V., Shang J.S., Garrison T.J., Zheltovodov A.A., Maksimov A.I. Evolution of the separated flowfield in a 3-D shock wave/turbulent boundary layer interaction // AIAA Paper. 97-1837. 14 p.
72. Gaitonde D.V., Visbal M.R., Shang J.S., Zheltovodov A.A., Maksimov A.I. Parametric investigation of flowfield structure and validation issues in 3-D crossing-shock wave/turbulent boundary layer interaction // // Proc.: Int. Conf. on the Methods of Aerophys. Research, June 29-July 3, 1998, Novosibirsk, Russia. Novosibirsk, 1994. Part 1. 10 p. (to be published).

8. FIGURES

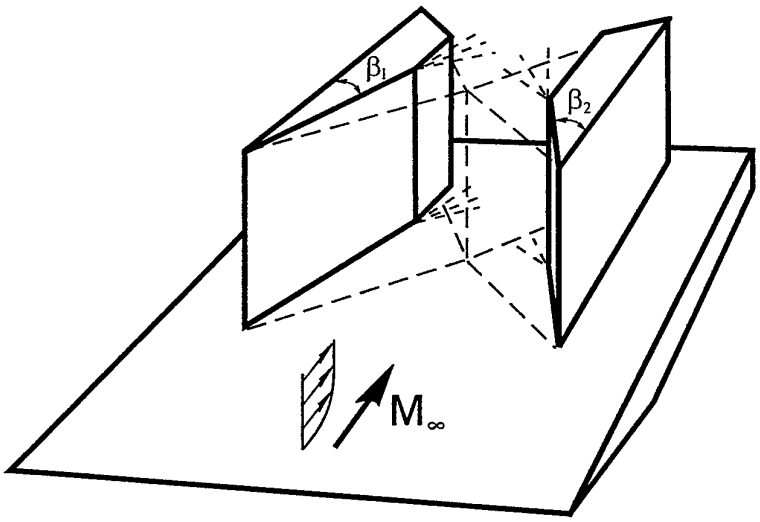
β1
β2
M∞

Fig. 1

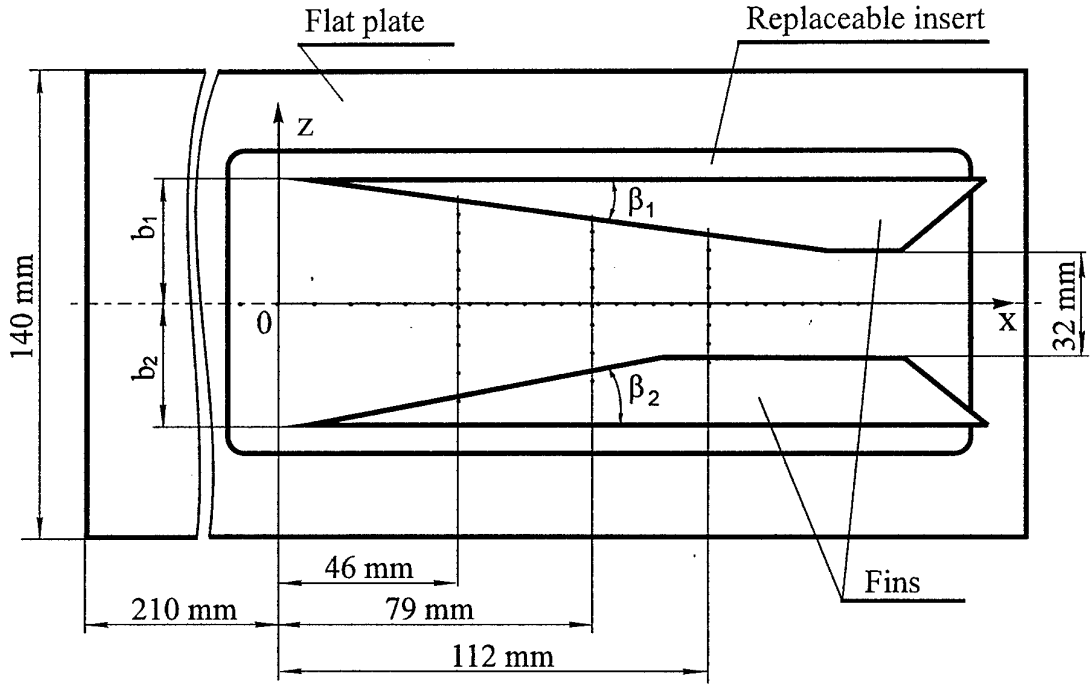
Flat plate
Replaceable insert
z
β1
b1
140 mm
0
x
32 mm
b2
β2
46 mm
Fins
210 mm
79 mm
112 mm

Fig. 2

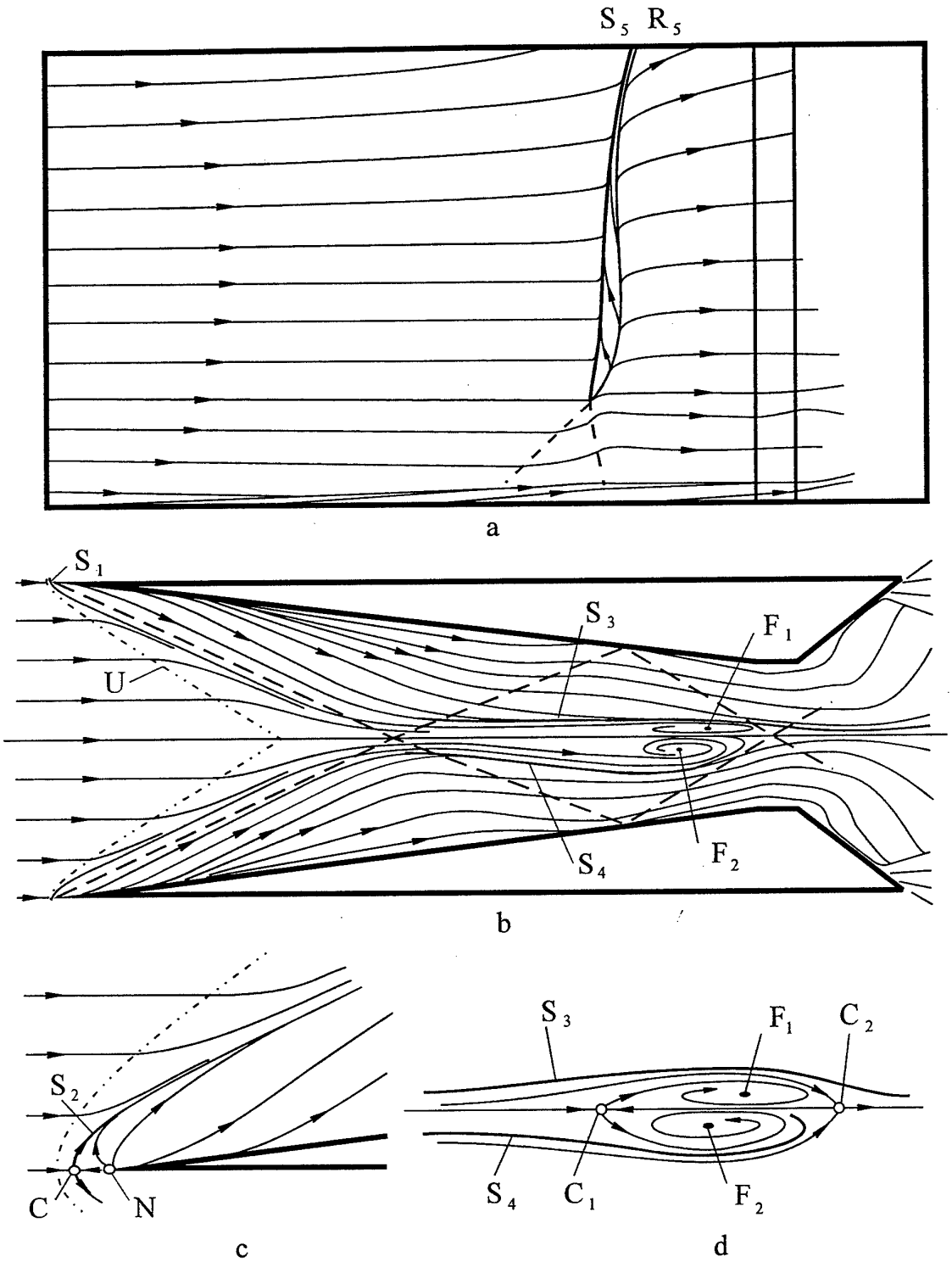

Fig. 3. Surface flow patterns at $M = 3$, $\beta_1 = \beta_2 = 7^\circ$

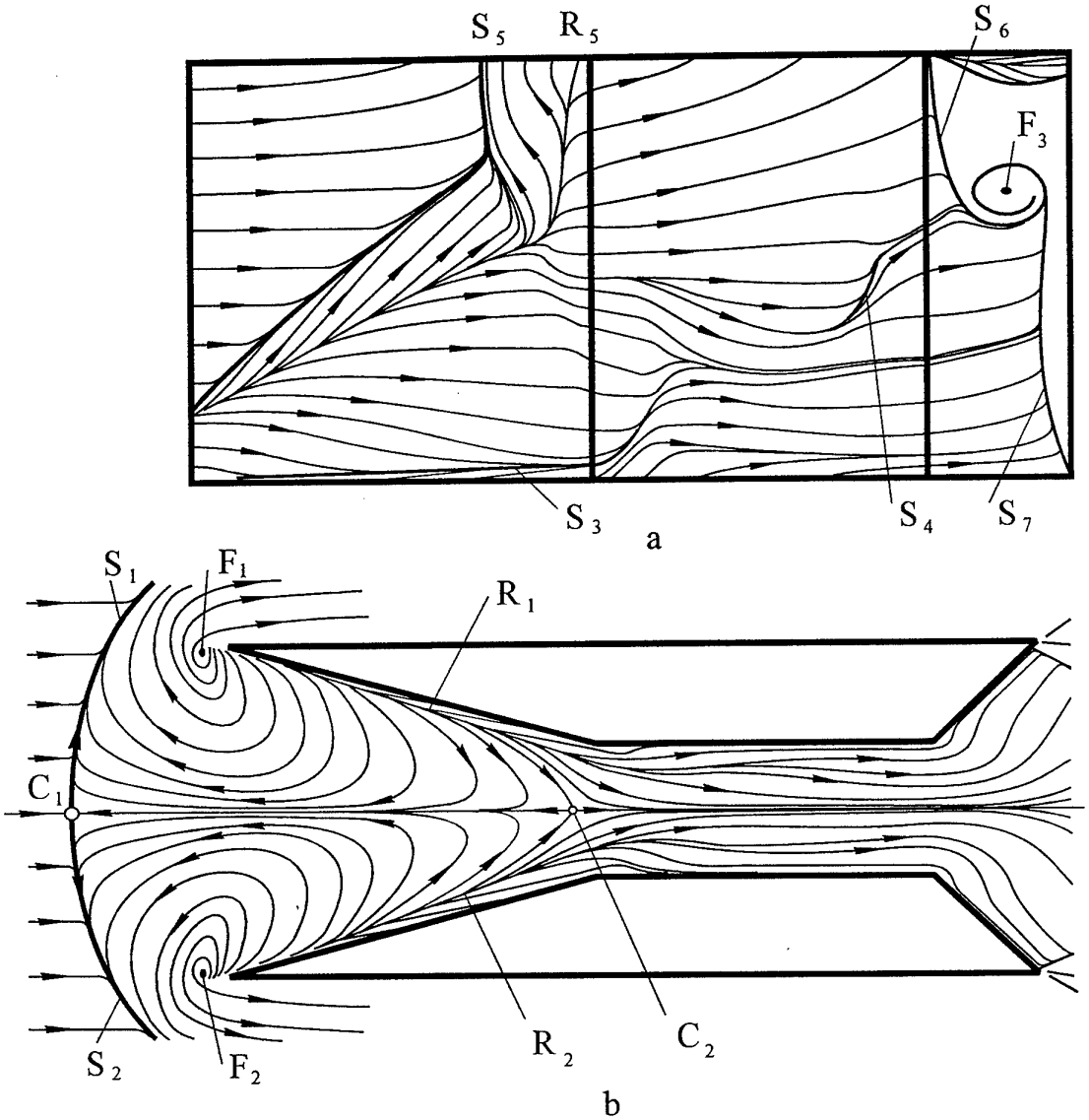

Fig. 4. Surface flow patterns at $M = 3, \beta_1 = \beta_2 = 15^\circ$

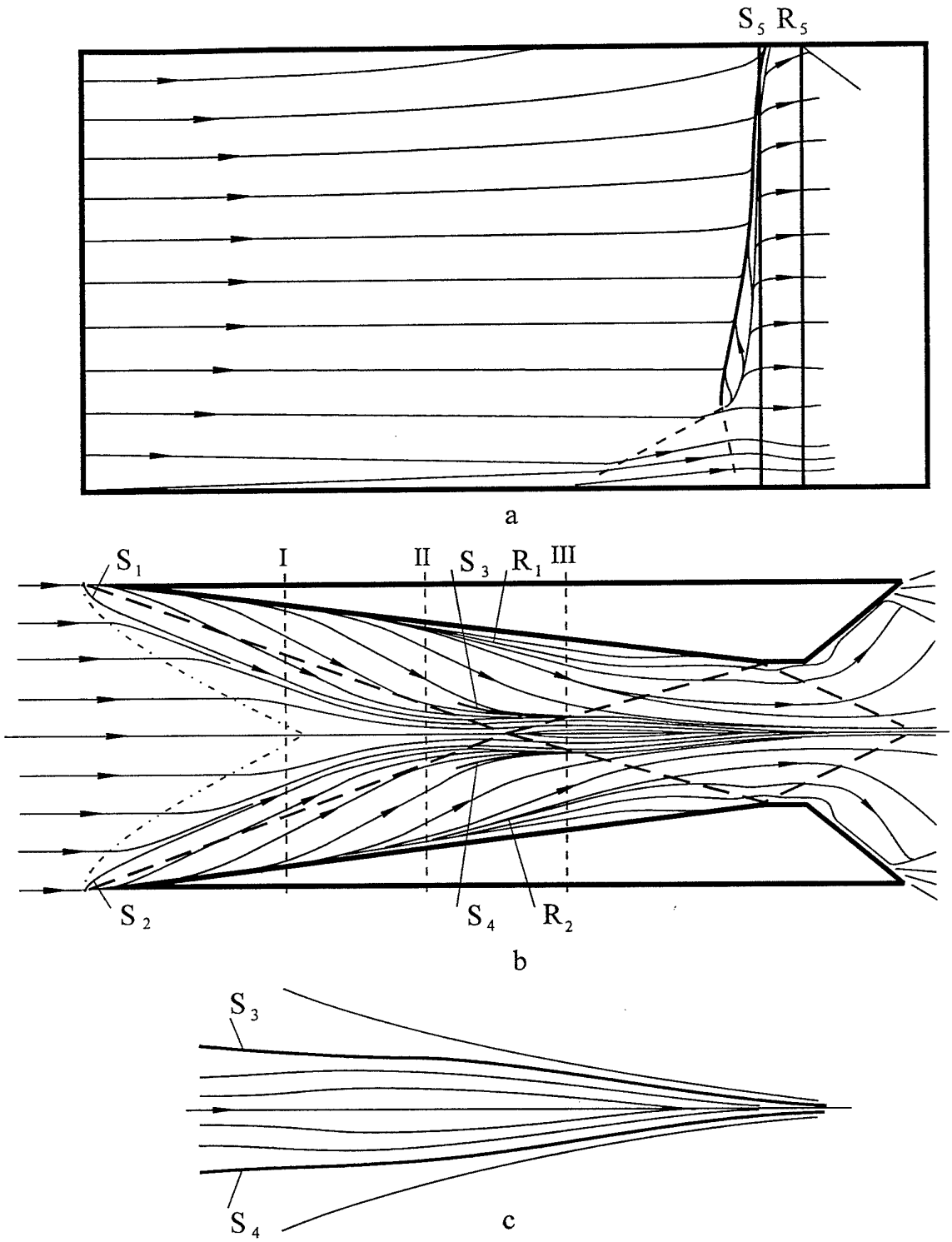

Fig. 5. Surface flow patterns at M = 3.9, $\beta_1 = \beta_2 = 7^\circ$

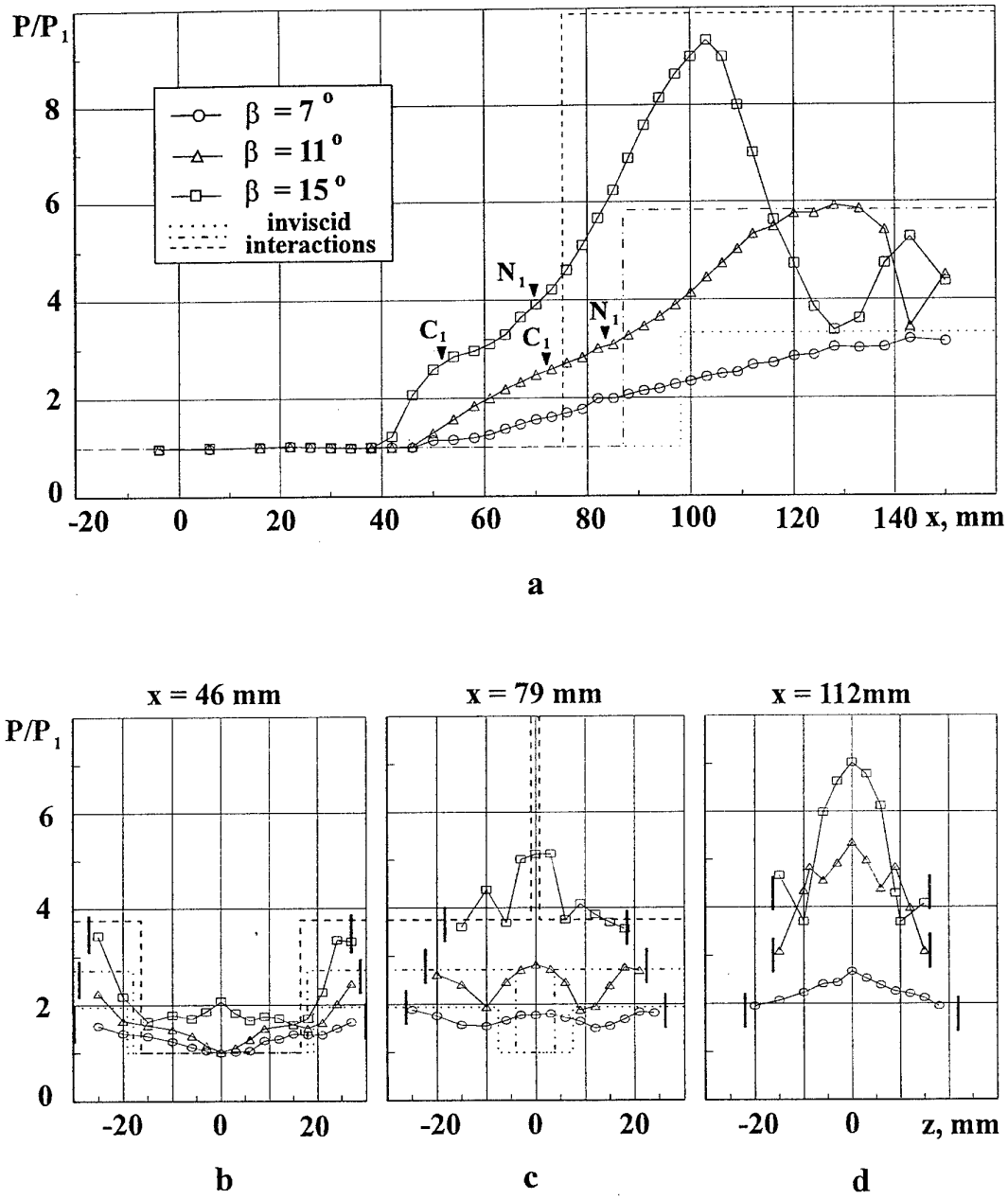
P/P1
β = 7°
β = 11°
β = 15°
inviscid
interactions
N1
C1
C1
N1
x, mm
a
x = 46 mm
x = 79 mm
x = 112mm
P/P1
z, mm
b
c
d

Fig. 6

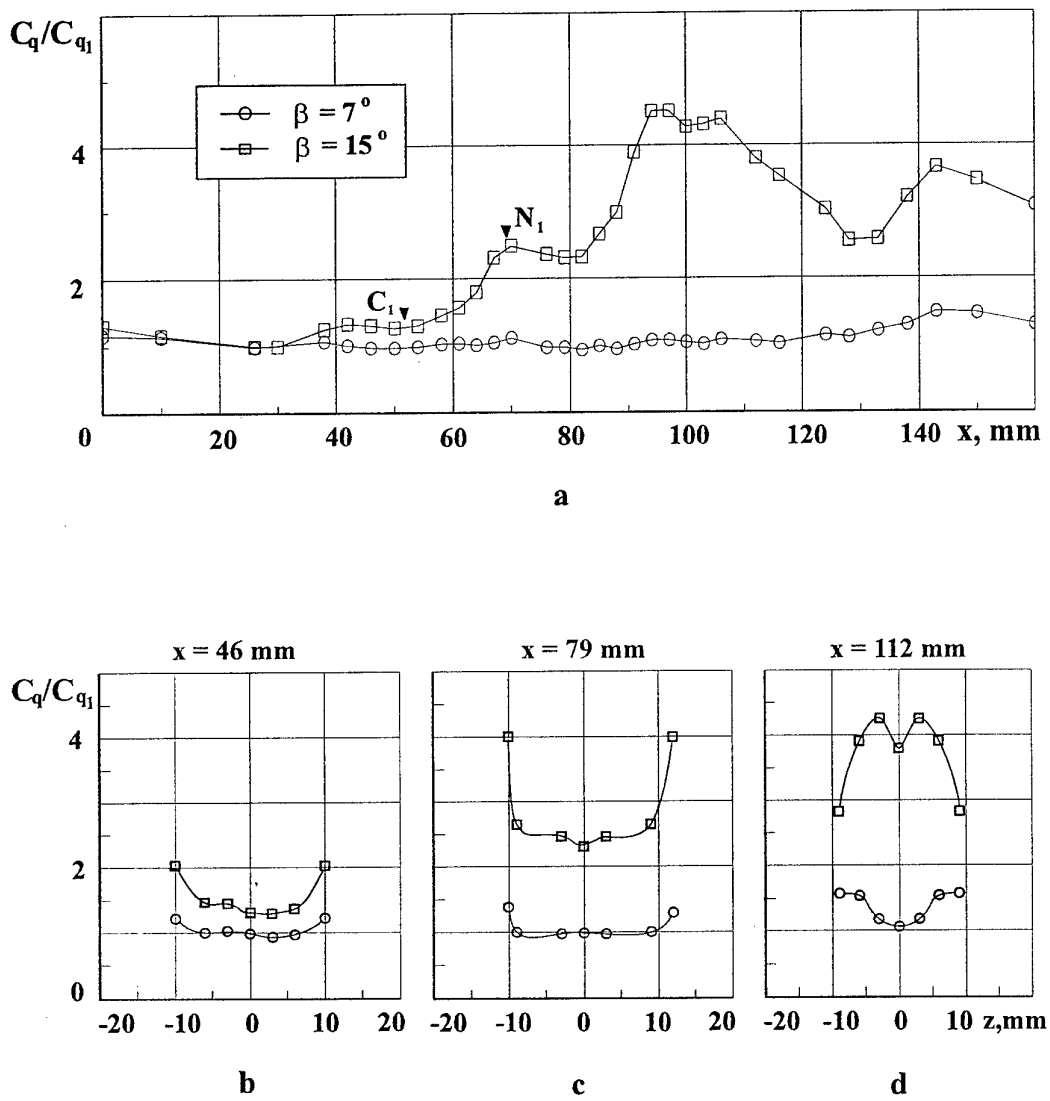
C_q/C_{q_1}
β = 7°
β = 15°
N_1
C_1
0
20
40
60
80
100
120
140
x, mm
a
x = 46 mm
x = 79 mm
x = 112 mm
C_q/C_{q_1}
4
2
0
-20
-10
0
10
20
z,mm
b
c
d

Fig. 7

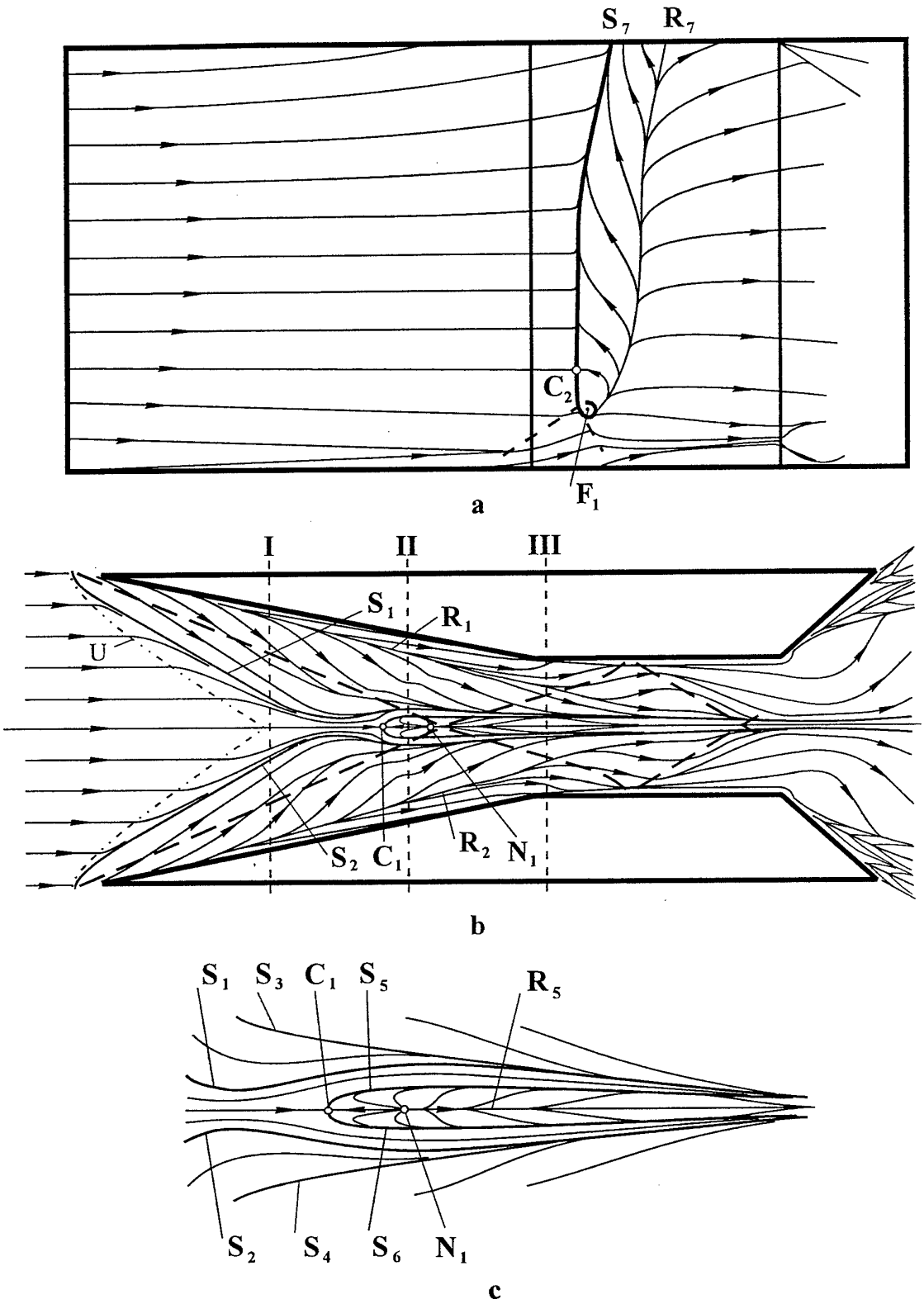

Fig. 8. Surface flow patterns at M = 3.9, $\beta_1 = \beta_2 = 11^\circ$

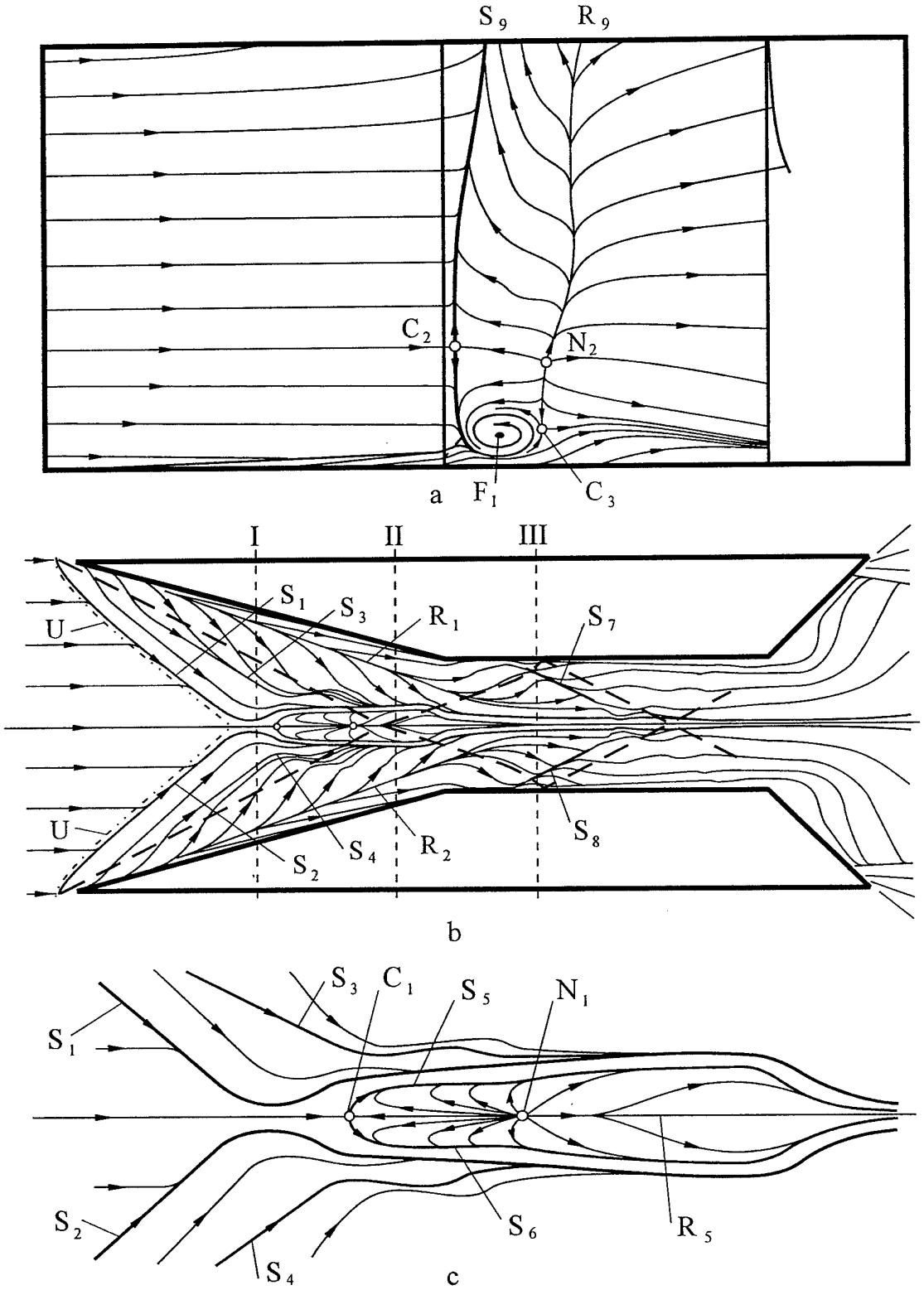

Fig. 9. Surface flow patterns at $M = 3.9$, $\beta_1 = \beta_2 = 15^\circ$

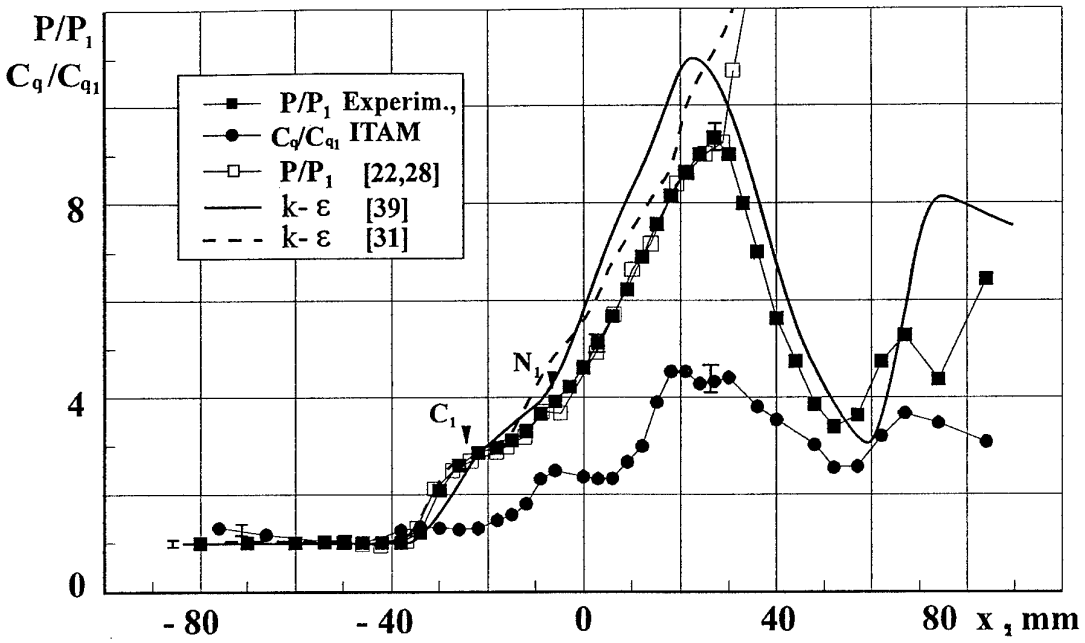
P/P1
Cq/Cq1
P/P1 Experim.,
Cq/Cq1 ITAM
P/P1 [22,28]
k- ε [39]
k- ε [31]
8
4
0
N1
C1
- 80
- 40
0
40
80
x1, mm

a

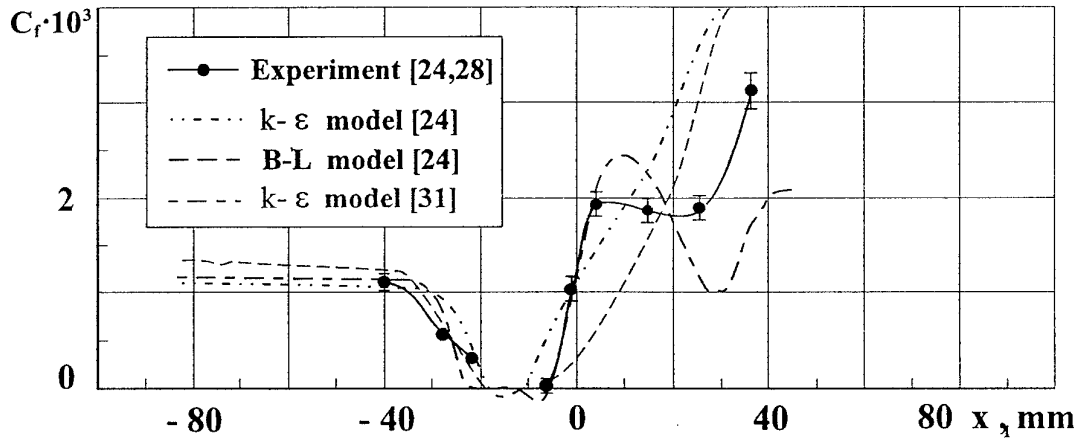
Cf·10³
Experiment [24,28]
k- ε model [24]
B-L model [24]
k- ε model [31]
2
0
- 80
- 40
0
40
80
x1, mm

b

Fig. 10

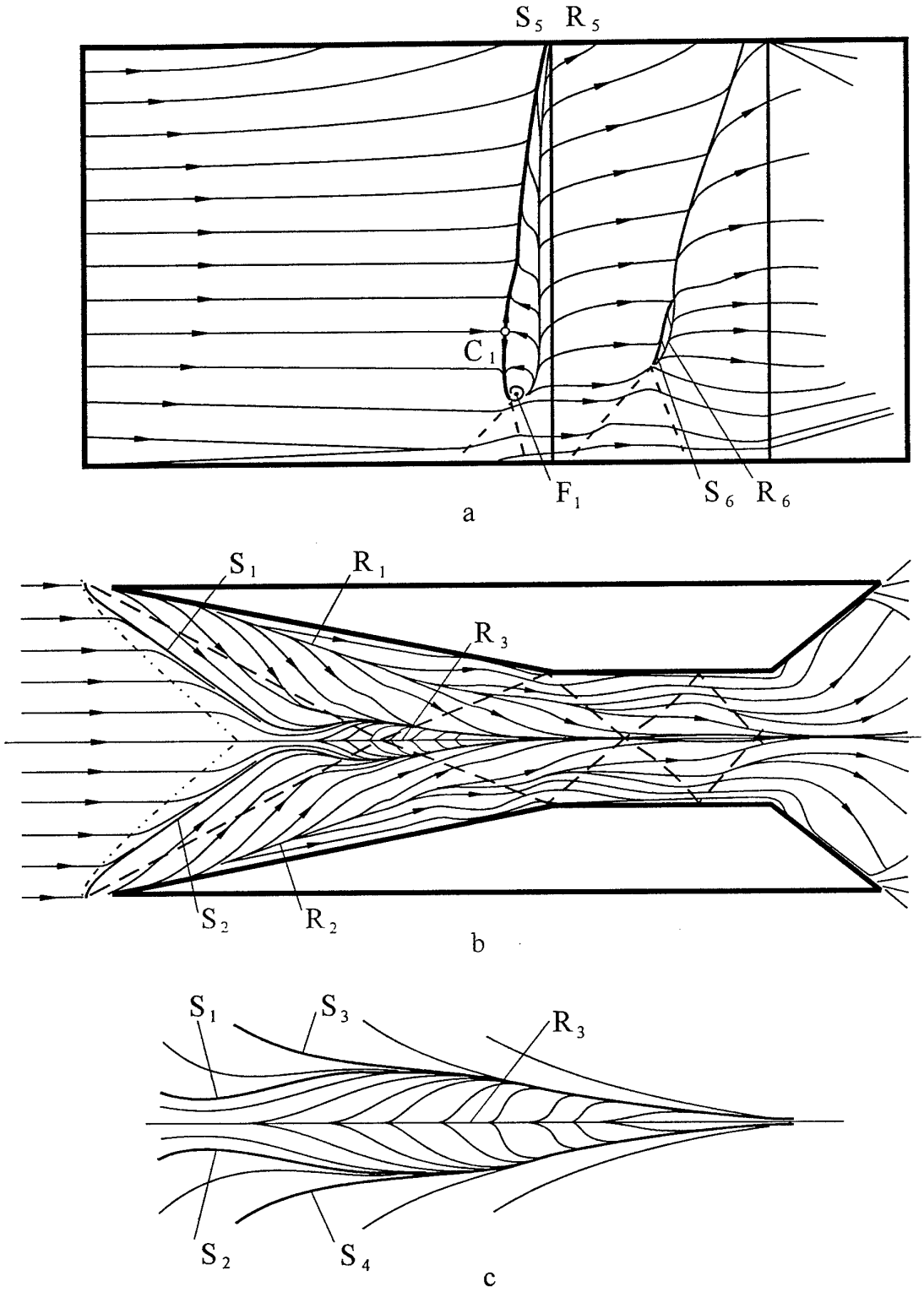

Fig. 11. Surface flow patterns at $M = 3$, $\beta_1 = \beta_2 = 11^\circ$

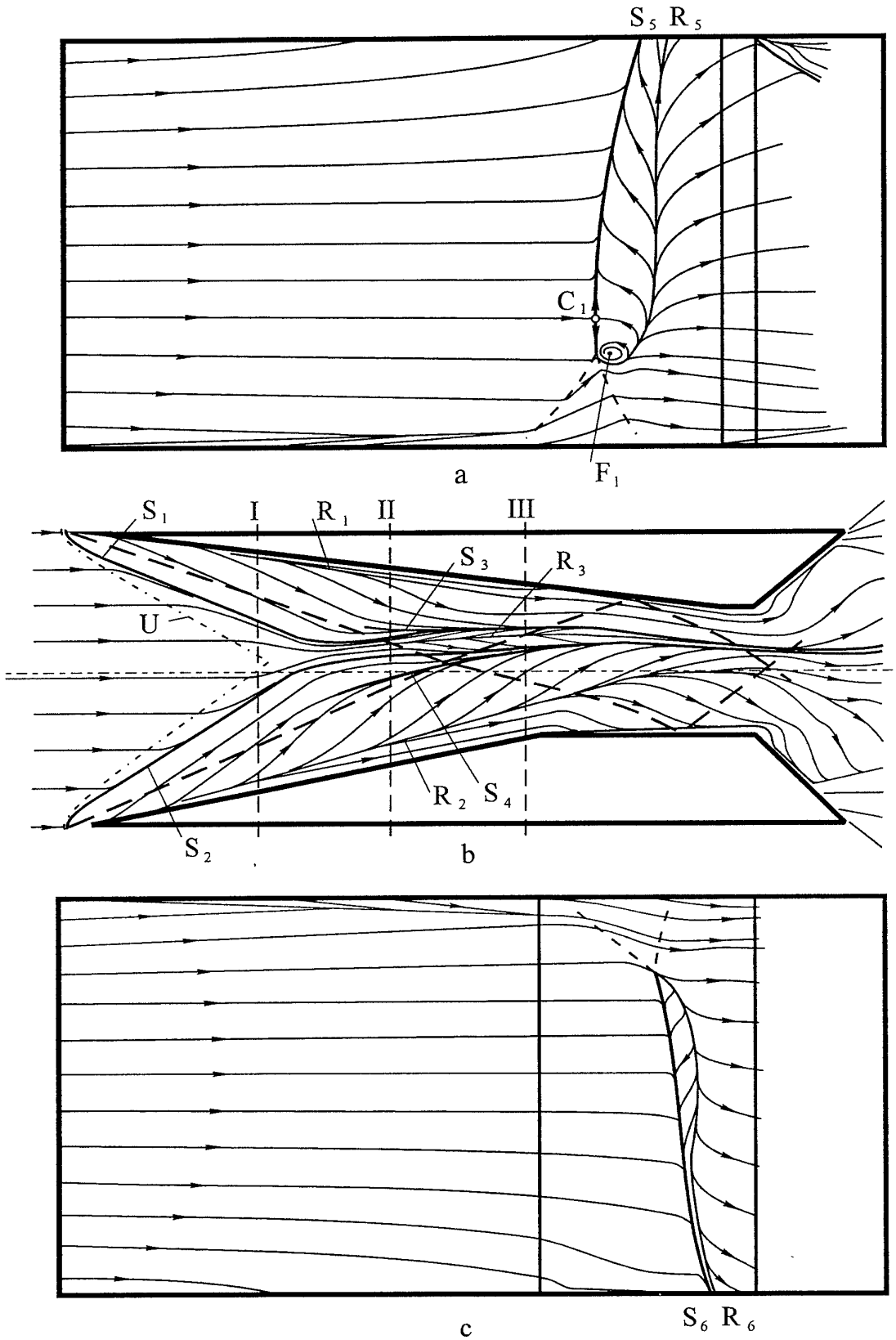

Fig. 12. Surface flow patterns at M = 3.9, $\beta_1 = 7^\circ$, $\beta_2 = 11^\circ$

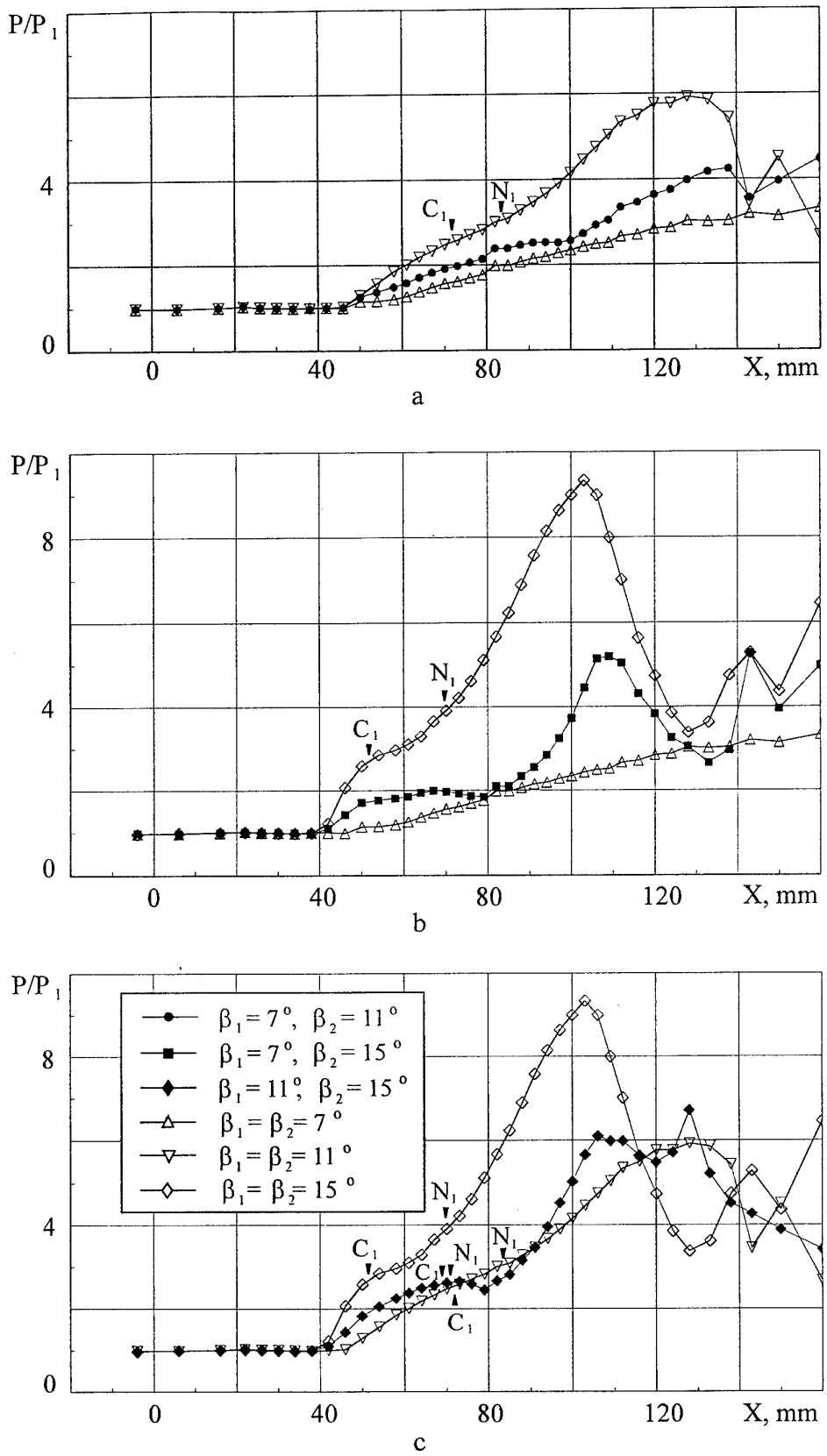
P/P 1
4
0
0
40
80
120
X, mm
C1
N1
a
P/P 1
8
4
0
0
40
80
120
X, mm
N1
C1
b
P/P 1
8
4
0
0
40
80
120
X, mm
β1 = 7°, β2 = 11°
β1 = 7°, β2 = 15°
β1 = 11°, β2 = 15°
β1 = β2 = 7°
β1 = β2 = 11°
β1 = β2 = 15°
N1
C1
N1
N1
C1
C1
c

Fig. 13

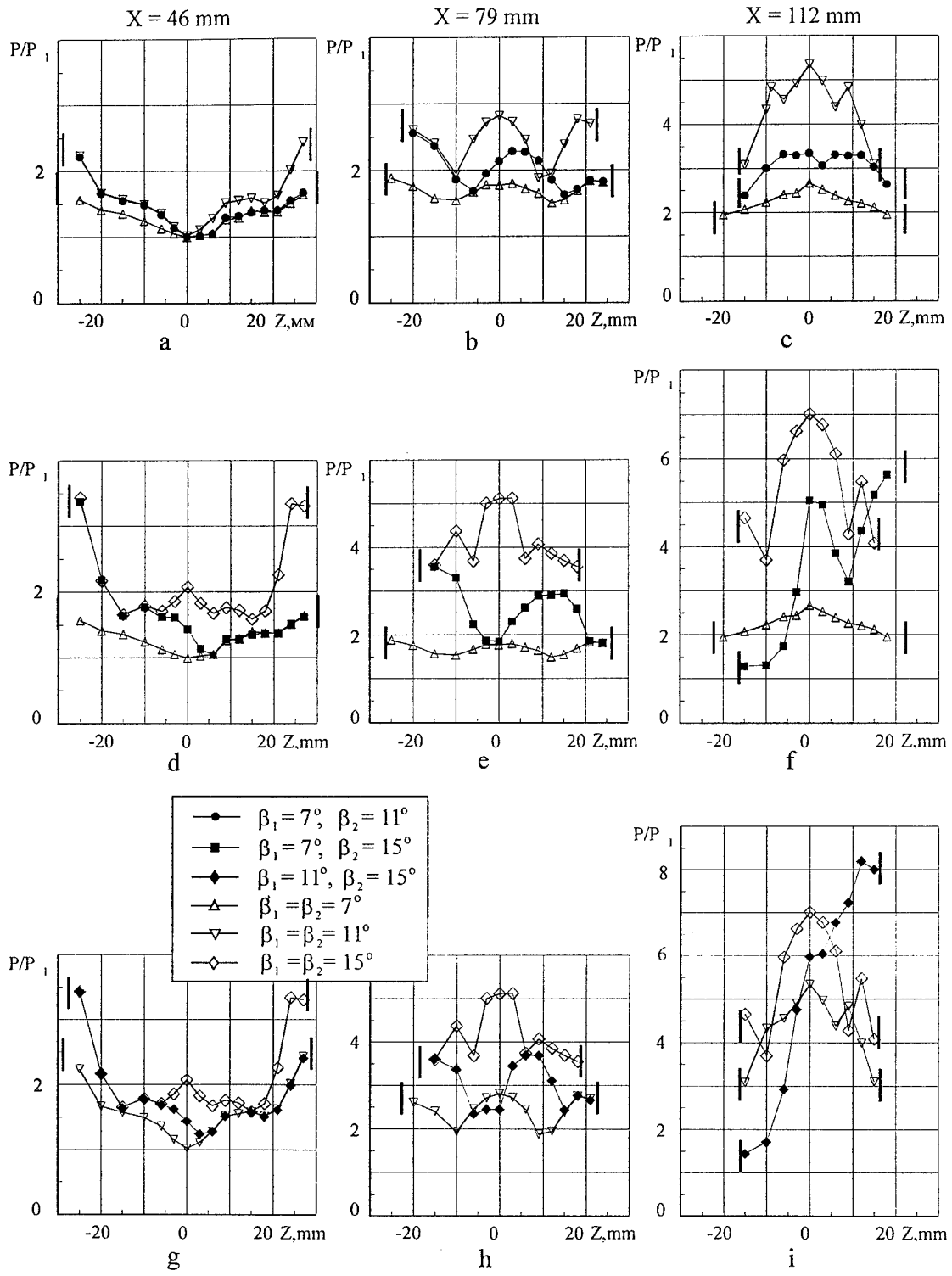
X = 46 mm
X = 79 mm
X = 112 mm
P/P 1
Z,мм
Z,mm
a
b
c
d
e
f
g
h
i
β1 = 7°, β2 = 11°
β1 = 7°, β2 = 15°
β1 = 11°, β2 = 15°
β1 = β2 = 7°
β1 = β2 = 11°
β1 = β2 = 15°

Fig. 14

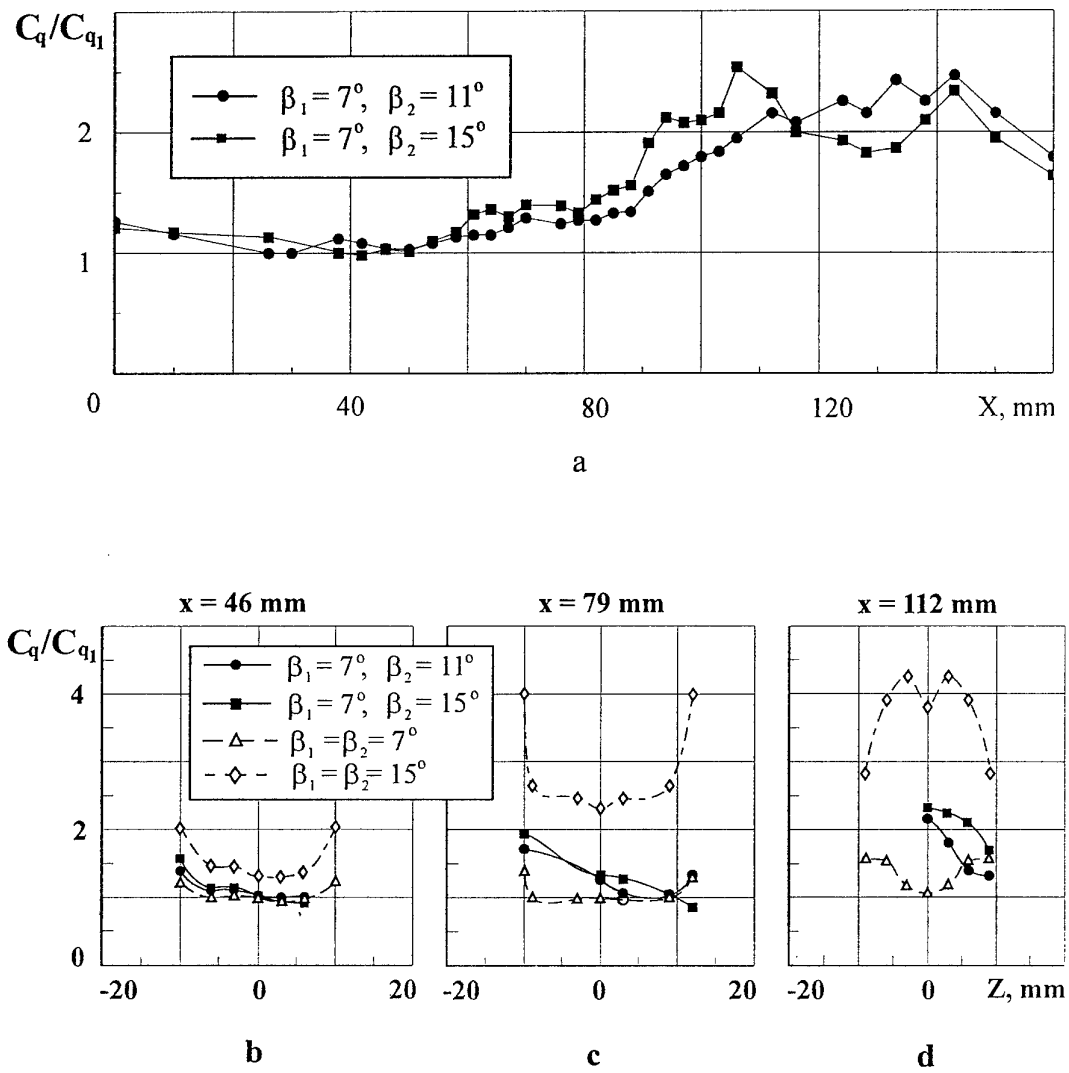
C_q/C_{q_1}
$\beta_1 = 7°$, $\beta_2 = 11°$
$\beta_1 = 7°$, $\beta_2 = 15°$
2
1
0
40
80
120
X, mm
a
x = 46 mm
x = 79 mm
x = 112 mm
C_q/C_{q_1}
$\beta_1 = 7°$, $\beta_2 = 11°$
$\beta_1 = 7°$, $\beta_2 = 15°$
$\beta_1 = \beta_2 = 7°$
$\beta_1 = \beta_2 = 15°$
4
2
0
-20
0
20
-20
0
20
-20
0
Z, mm
b
c
d

Fig. 15

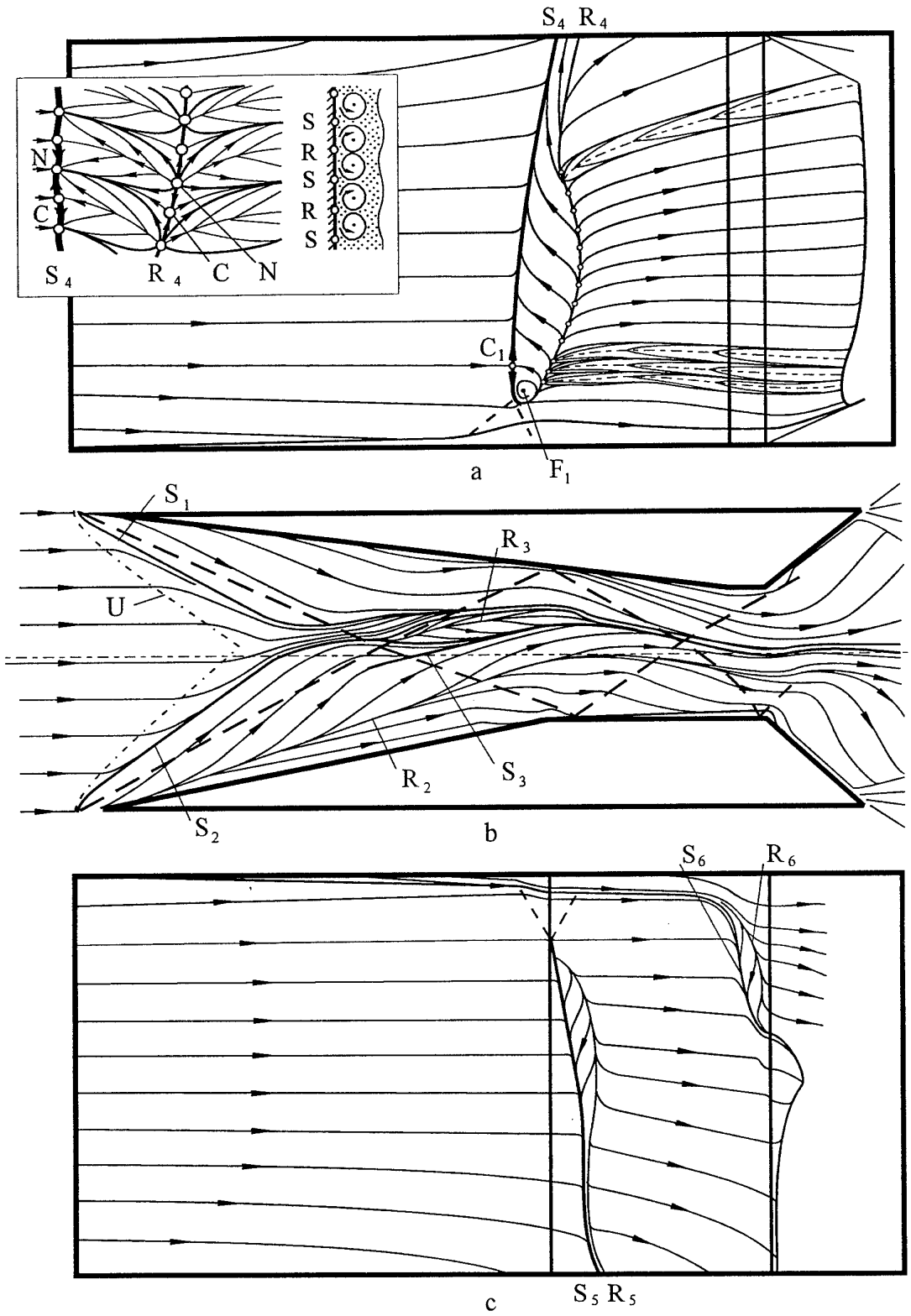

Fig. 16. Surface flow patterns at $M = 3$, $\beta_1 = 7°$, $\beta_2 = 11°$

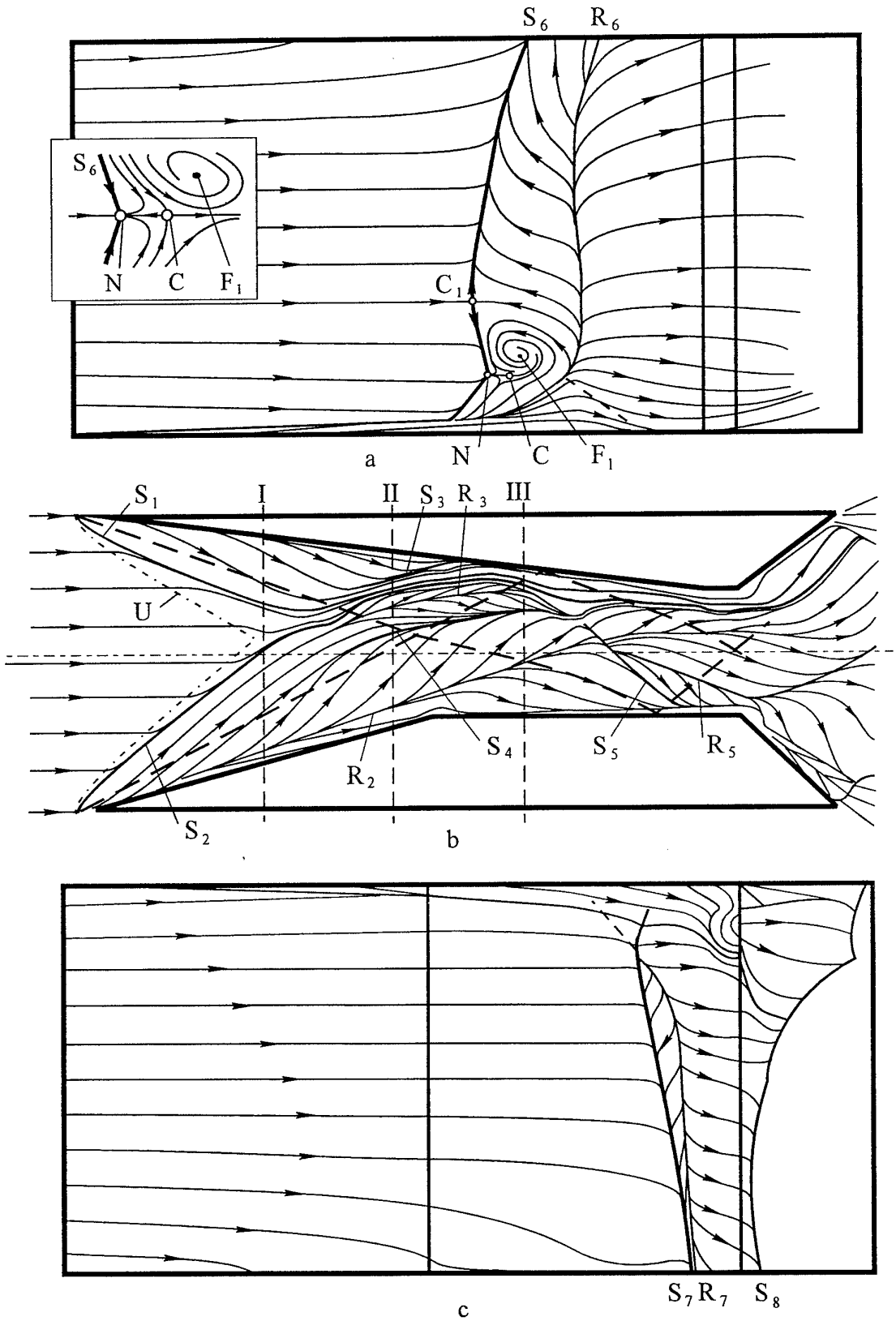

Fig. 17. Surface flow patterns at M = 3.9, β_1= 7°, β_2= 15°

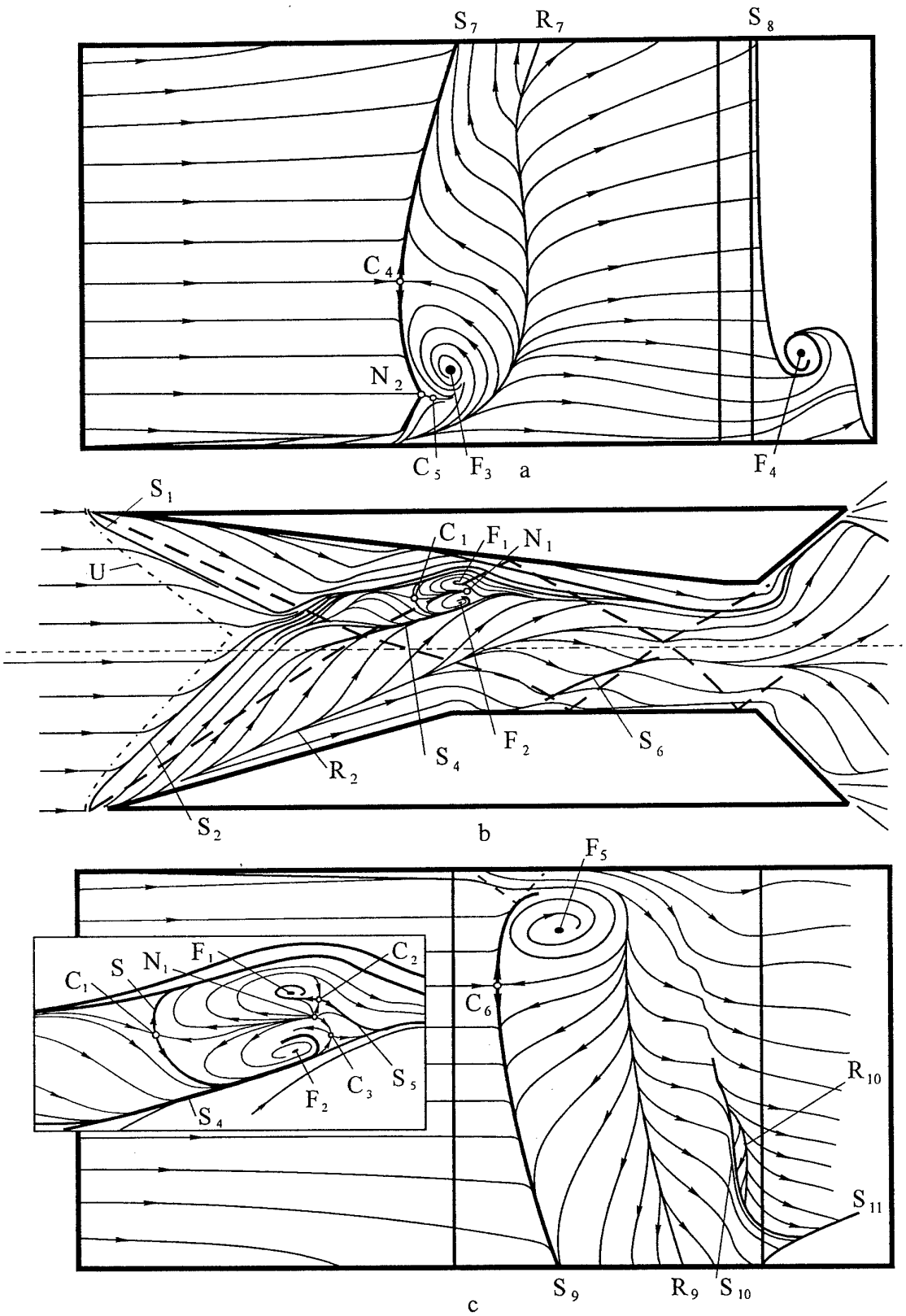

Fig. 18. Surface flow patterns at $M = 3$, $\beta_1 = 7^\circ$, $\beta_2 = 15^\circ$

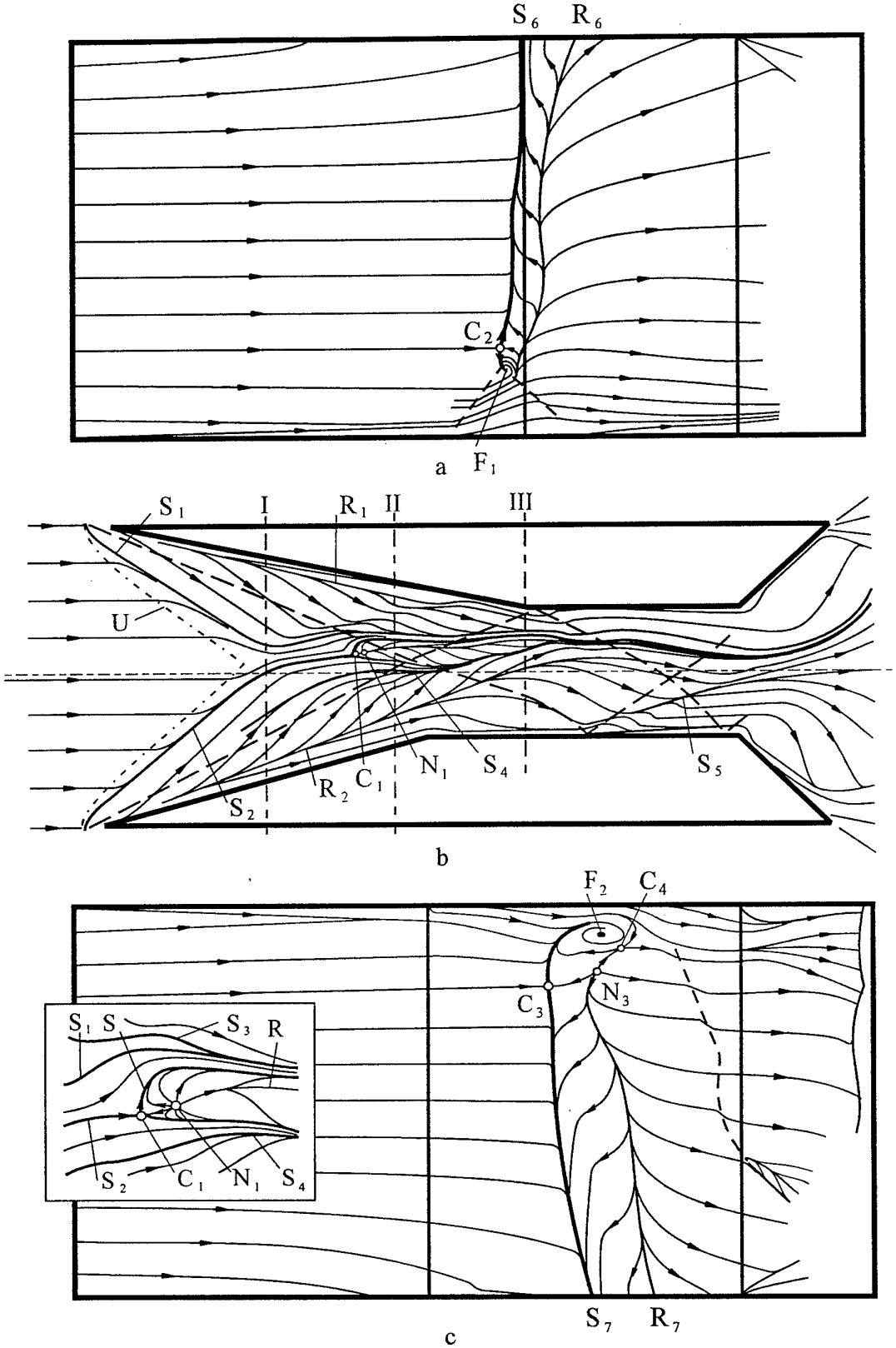

Fig. 19. Surface flow patterns at M = 3.9, $\beta_1 = 11^\circ$, $\beta_2 = 15^\circ$

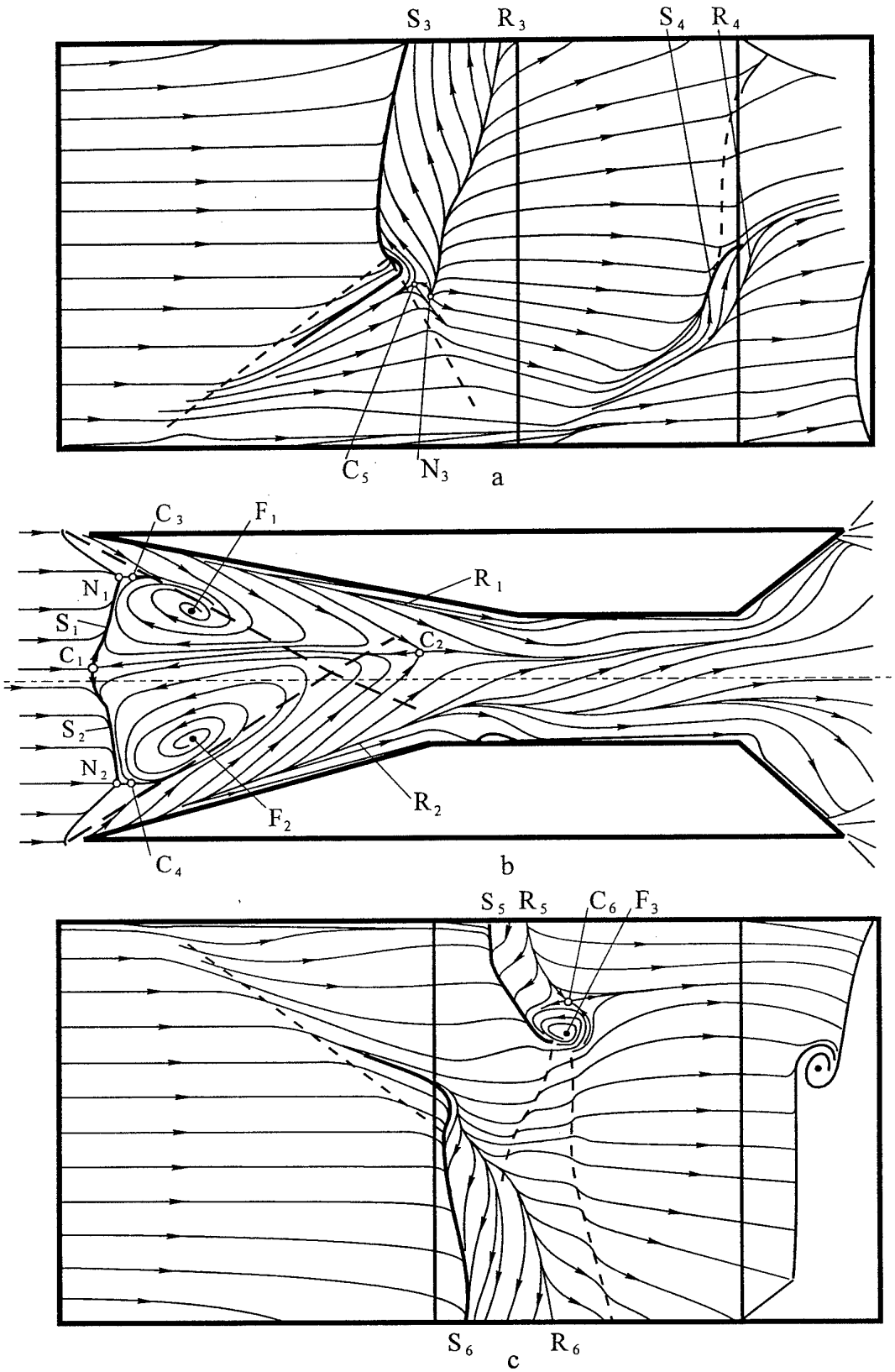

Fig. 20. Surface flow patterns at M = 3, β_1= 11°, β_2= 15°

APPENDIX 1

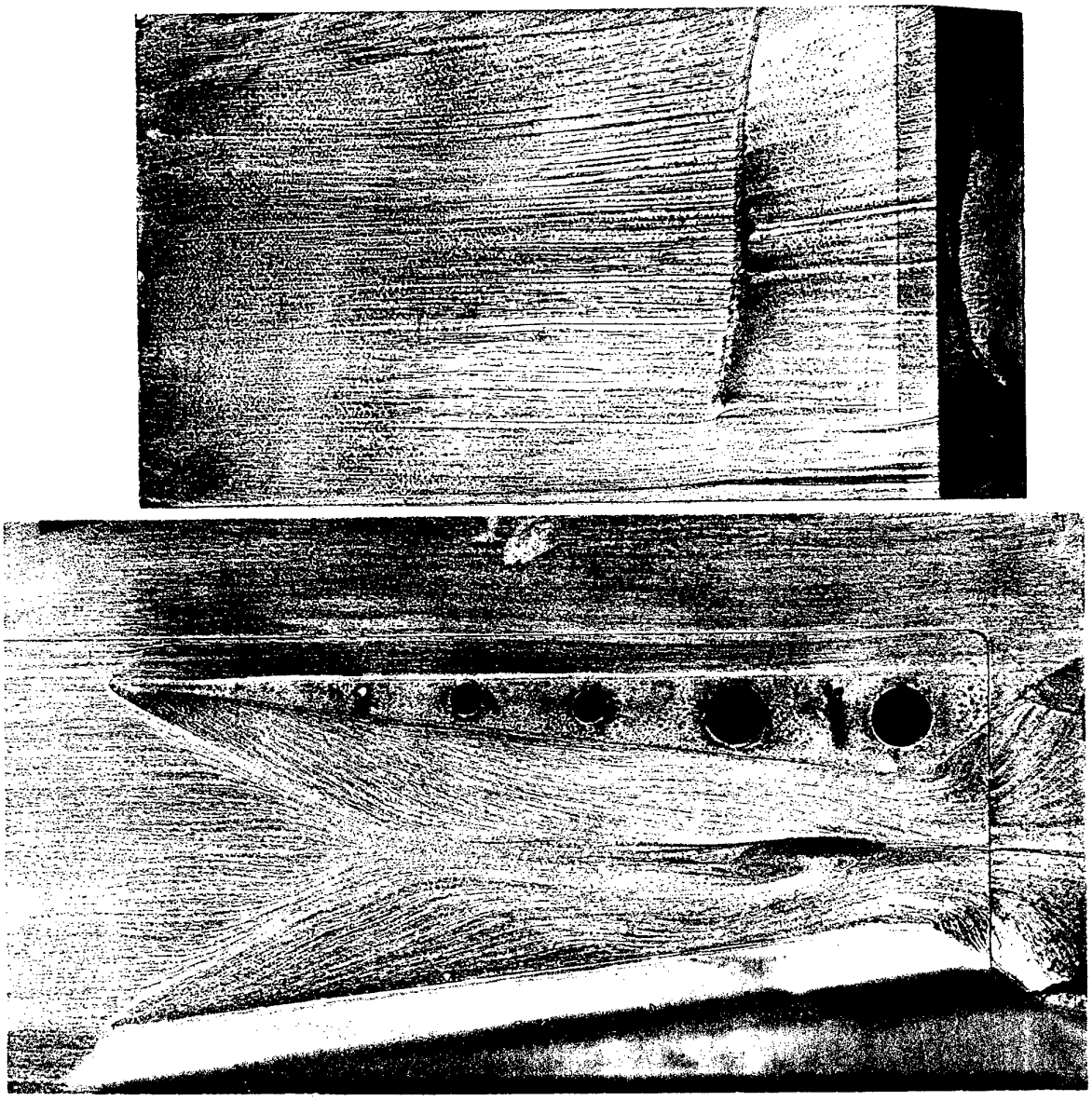

Fig. 1. $M_\infty = 3$, $\beta_1 = \beta_2 = 7°$

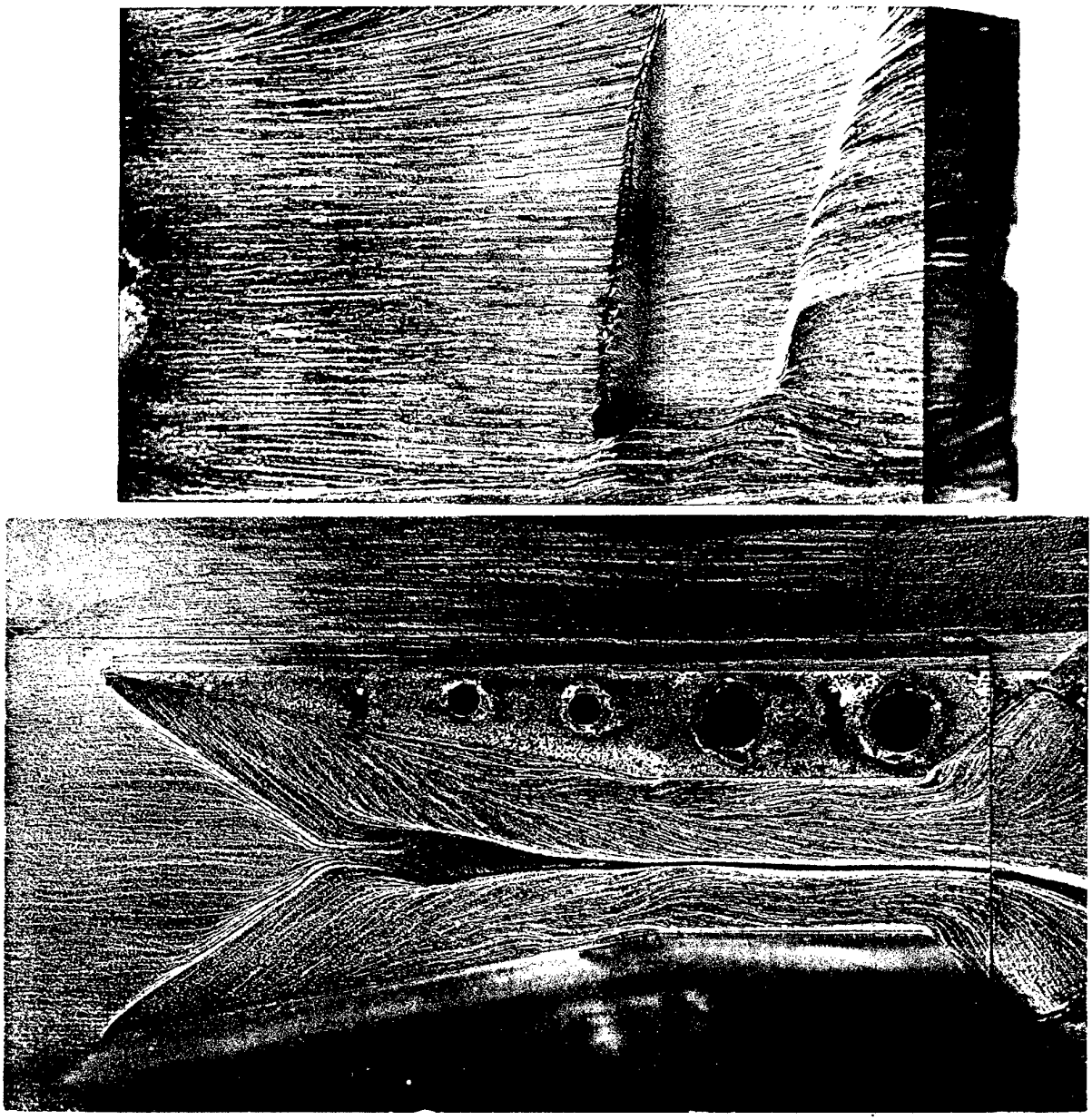

Fig. 2. $M_\infty = 3$, $\beta_1 = \beta_2 = 11°$

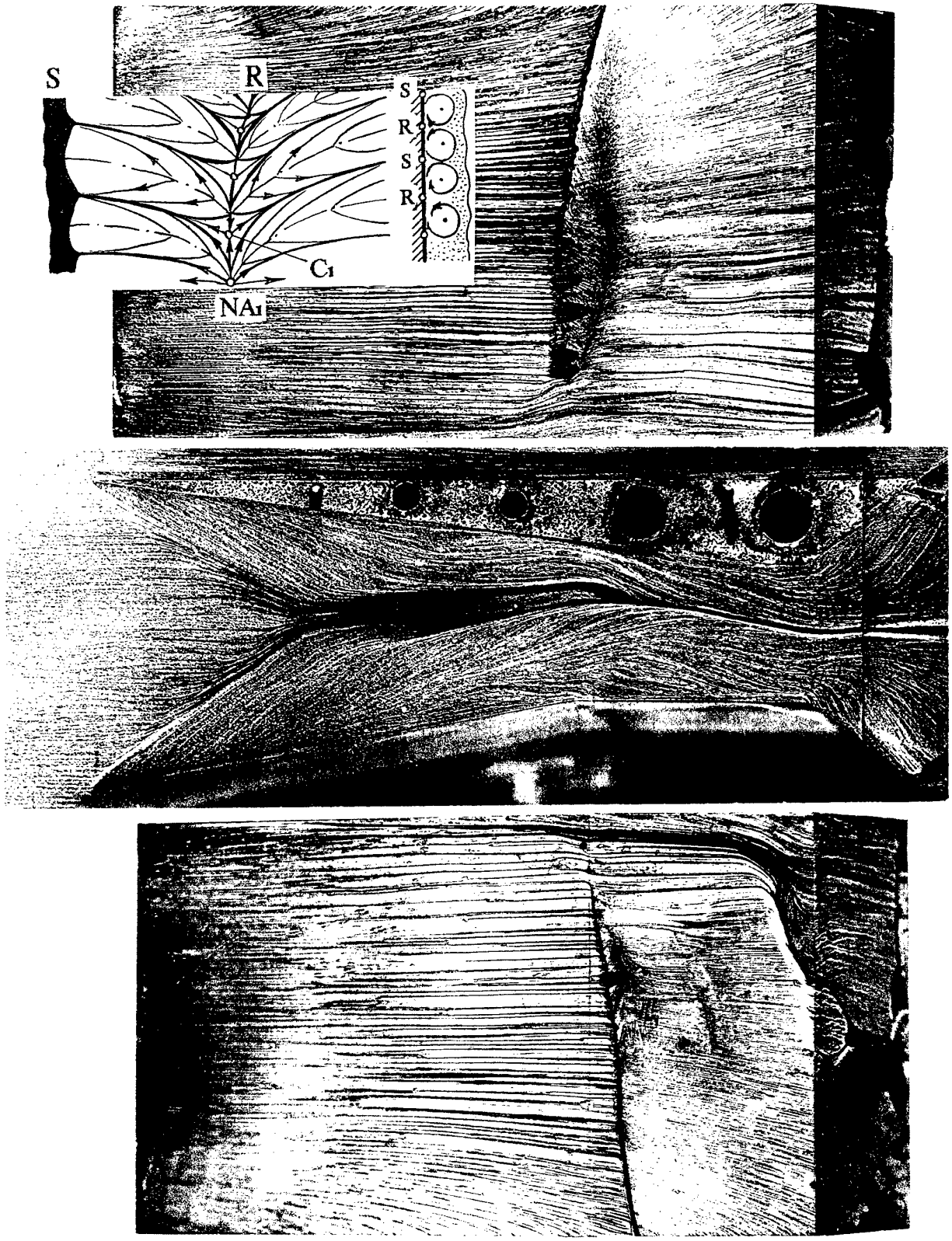

Fig. 3. $M_\infty = 3$, $\beta_1 = 7°$, $\beta_2 = 11°$

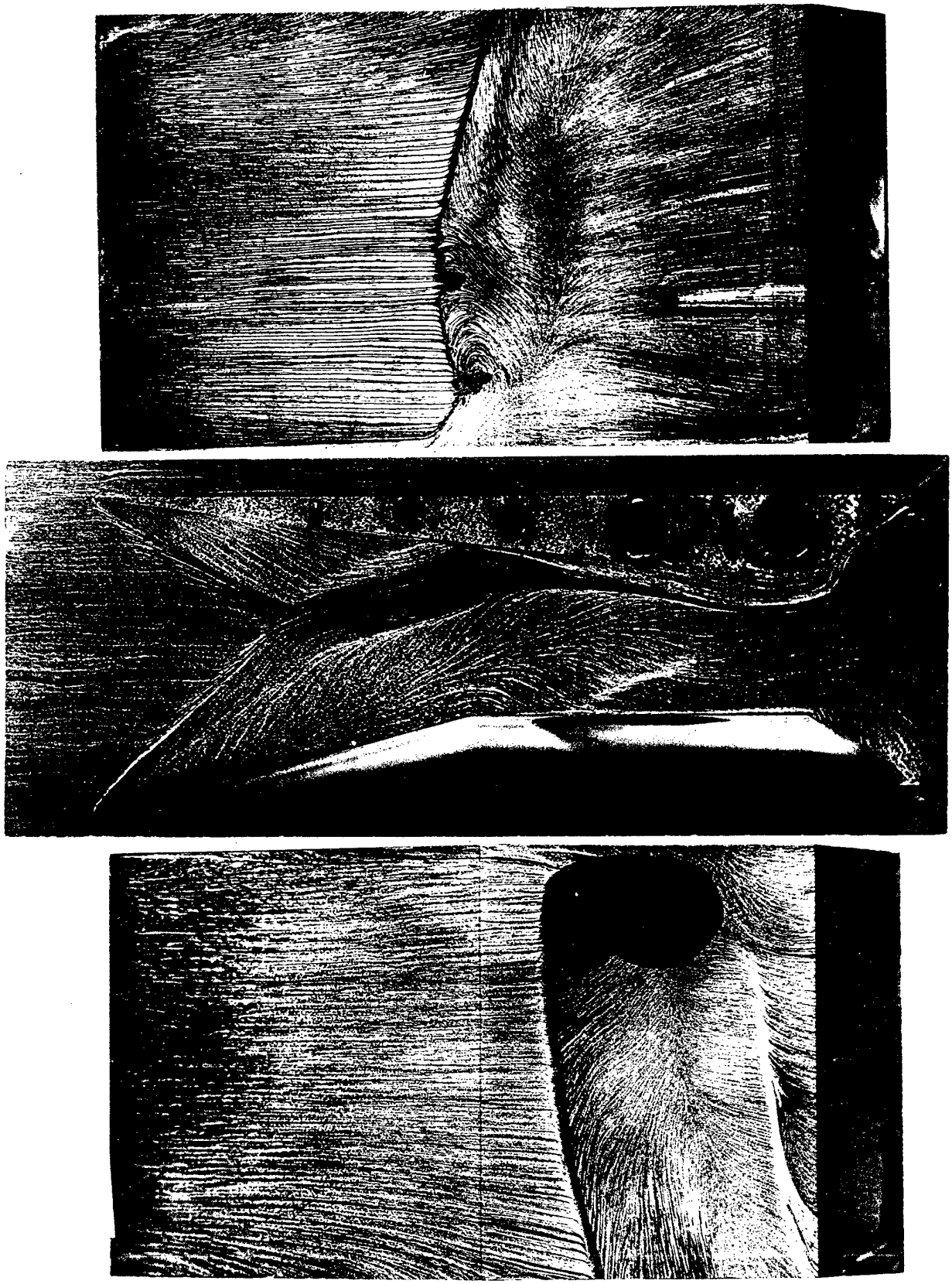

Fig. 4. $M_\infty = 3$, $\beta_1 = 7°$, $\beta_2 = 15°$

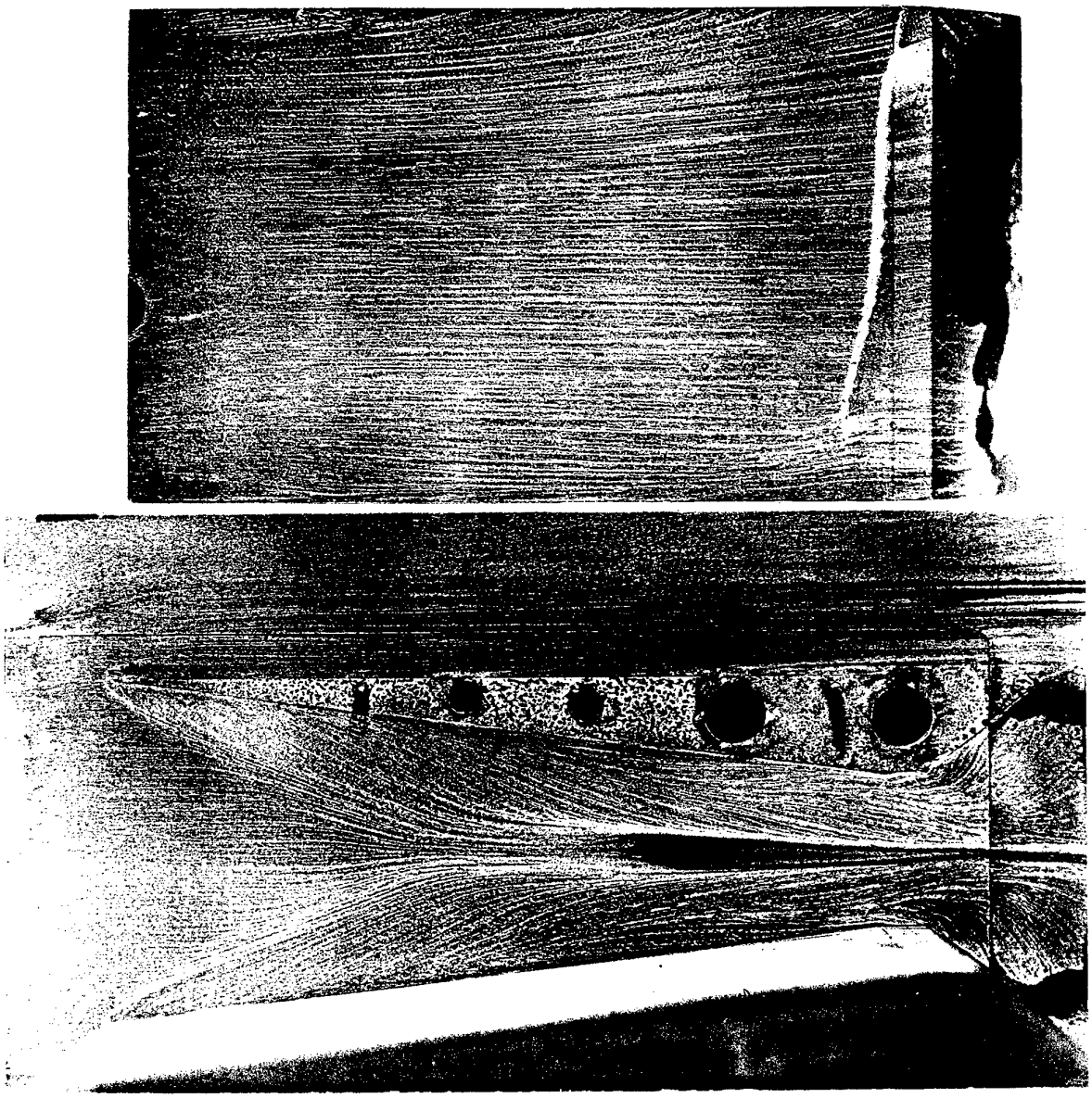

Fig. 5. $M_\infty = 4$, $\beta_1 = \beta_2 = 7°$

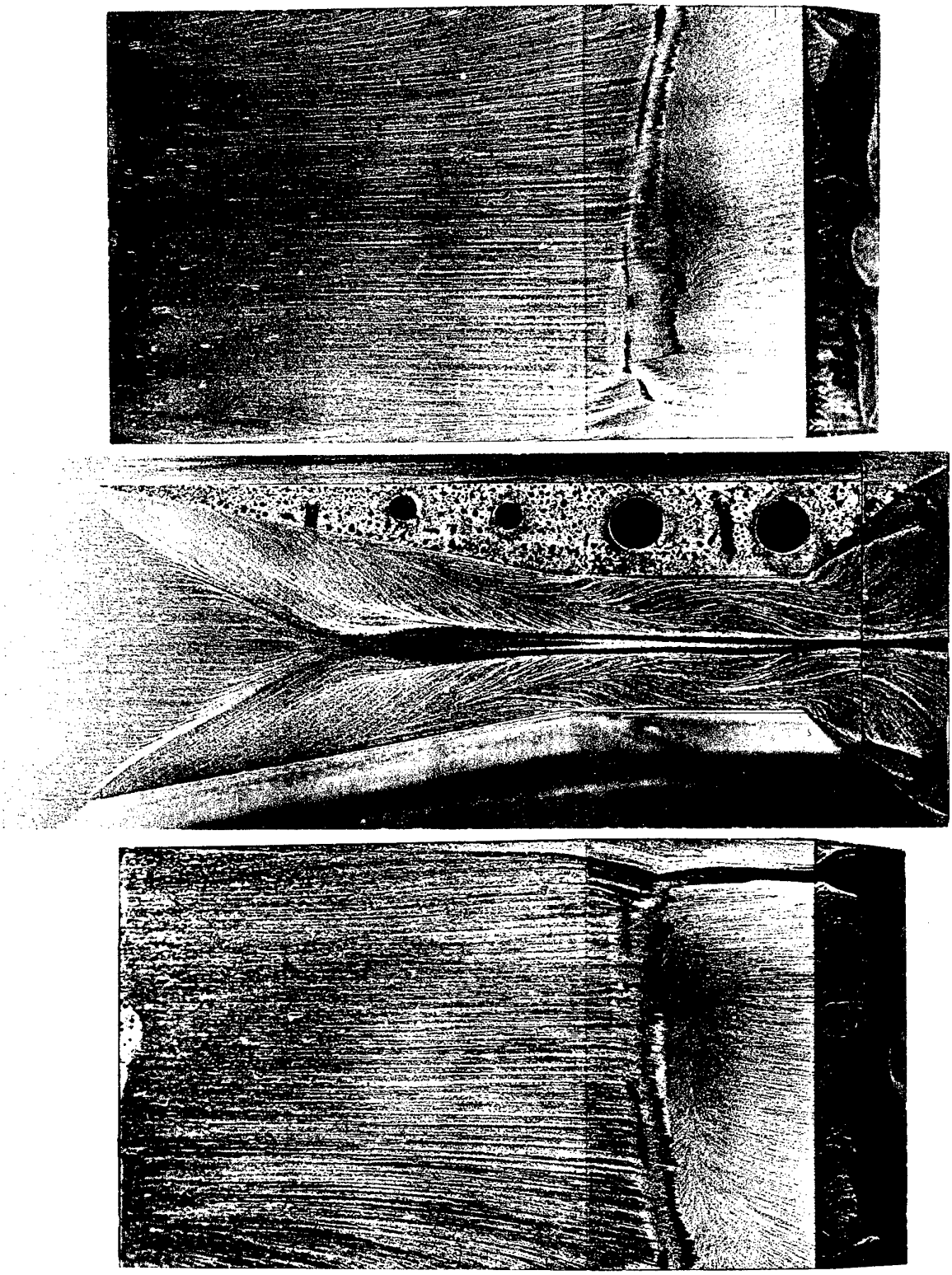

Fig. 6. $M_\infty = 4$, $\beta_1 = \beta_2 = 11°$

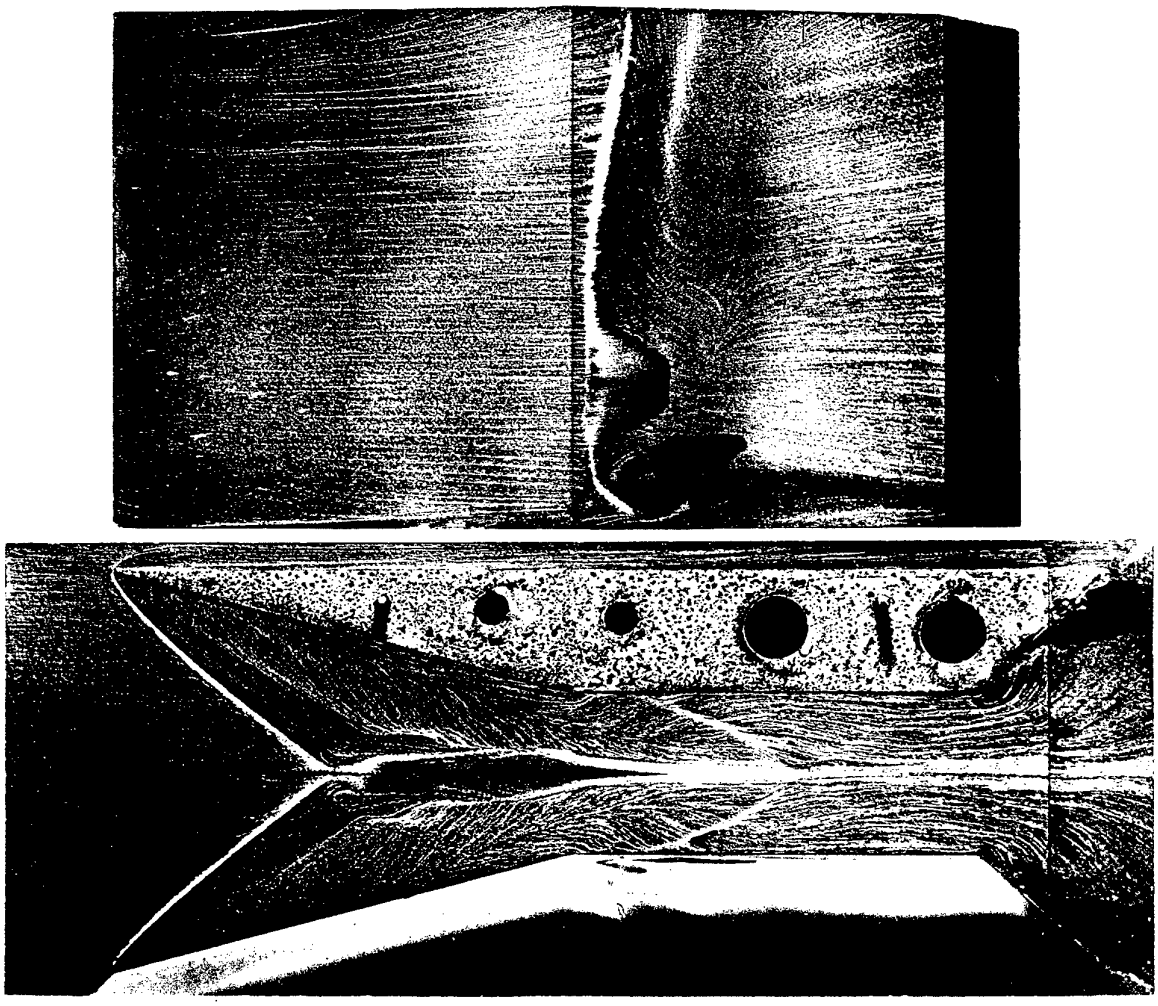

Fig. 7. $M_\infty = 4$, $\beta_1 = \beta_2 = 15°$

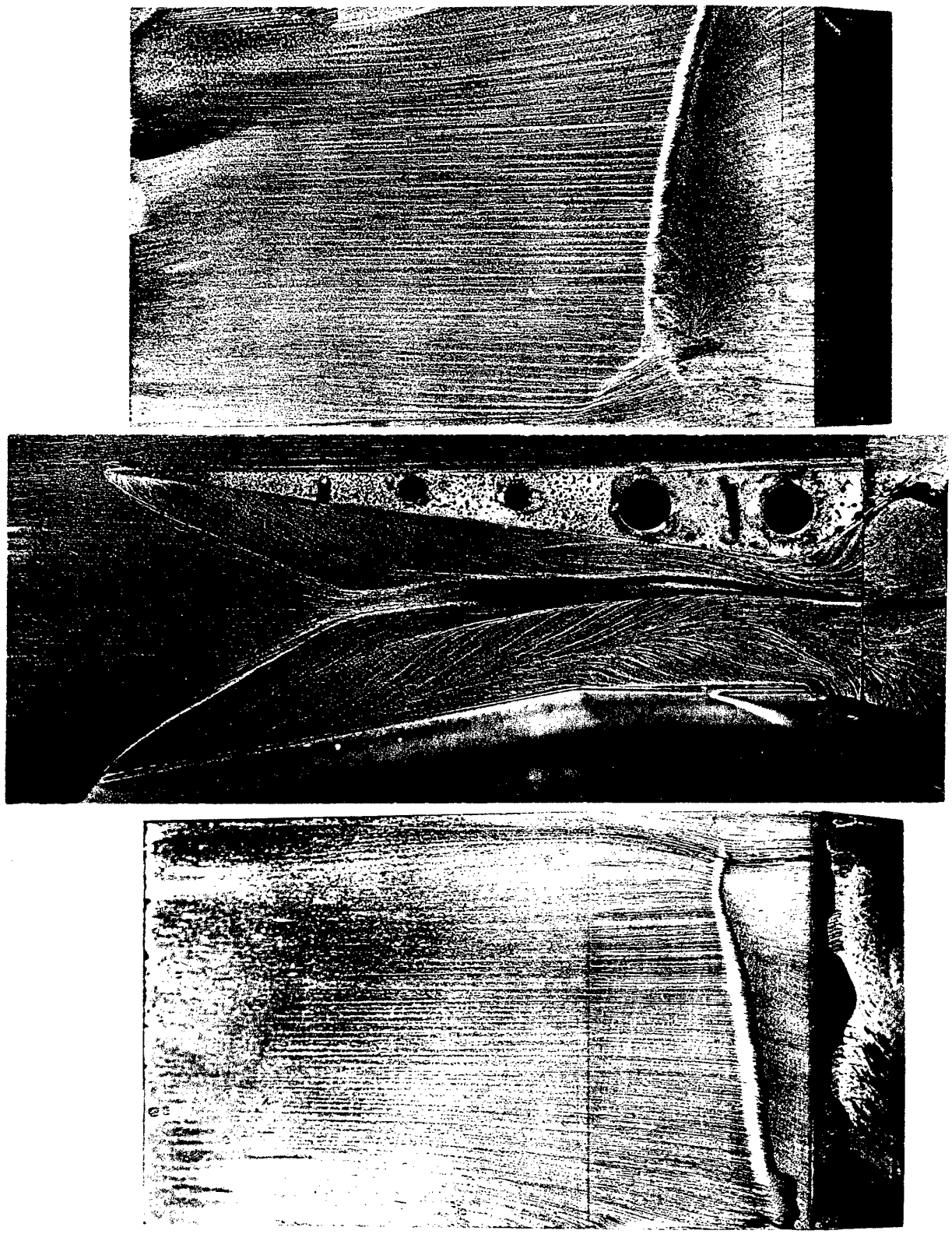

Fig. 8. $M_\infty = 4$, $\beta_1 = 7°$, $\beta_2 = 11°$

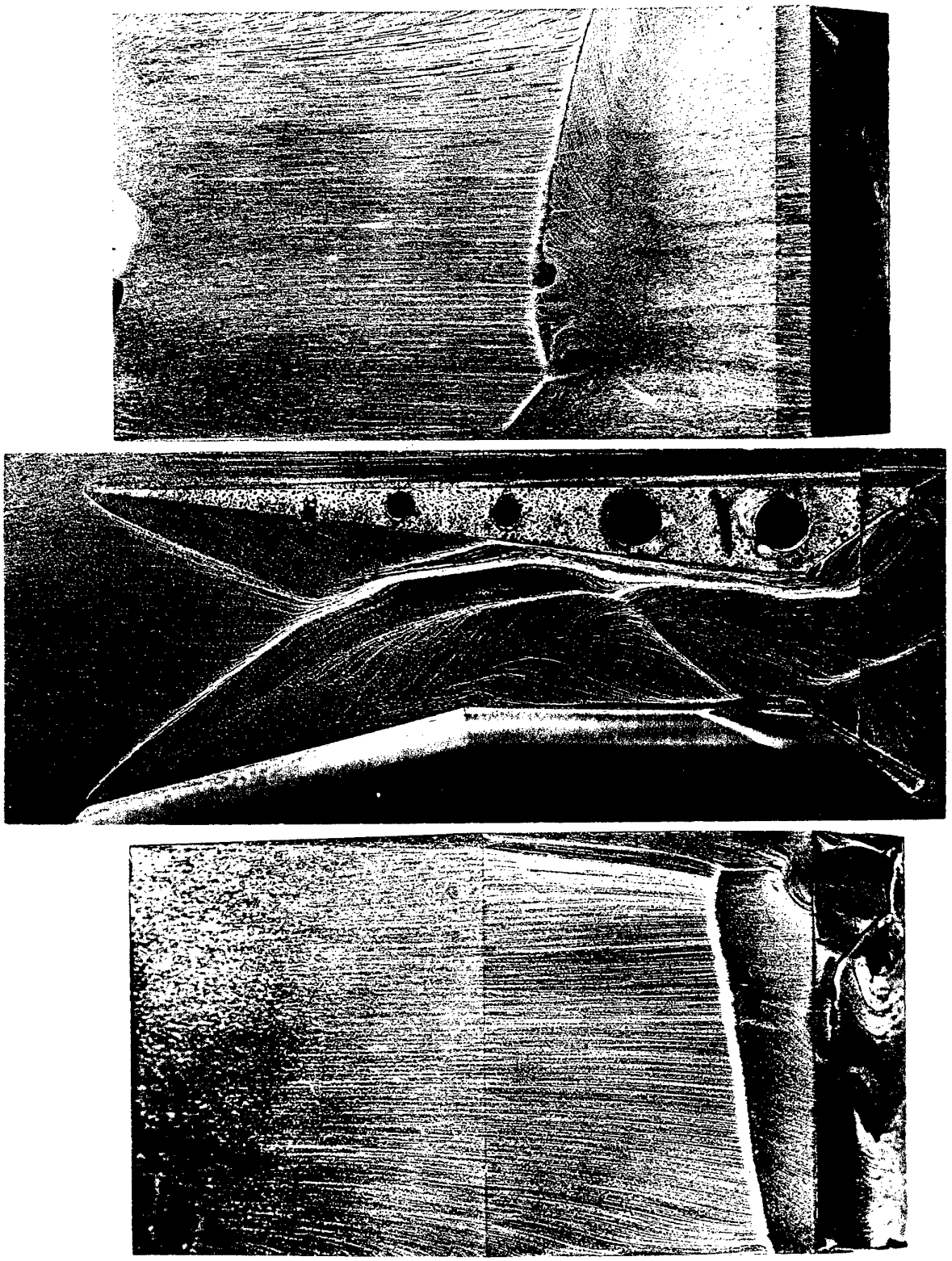

Fig. 9. $M_\infty = 4$, $\beta_1 = 7°$, $\beta_2 = 15°$

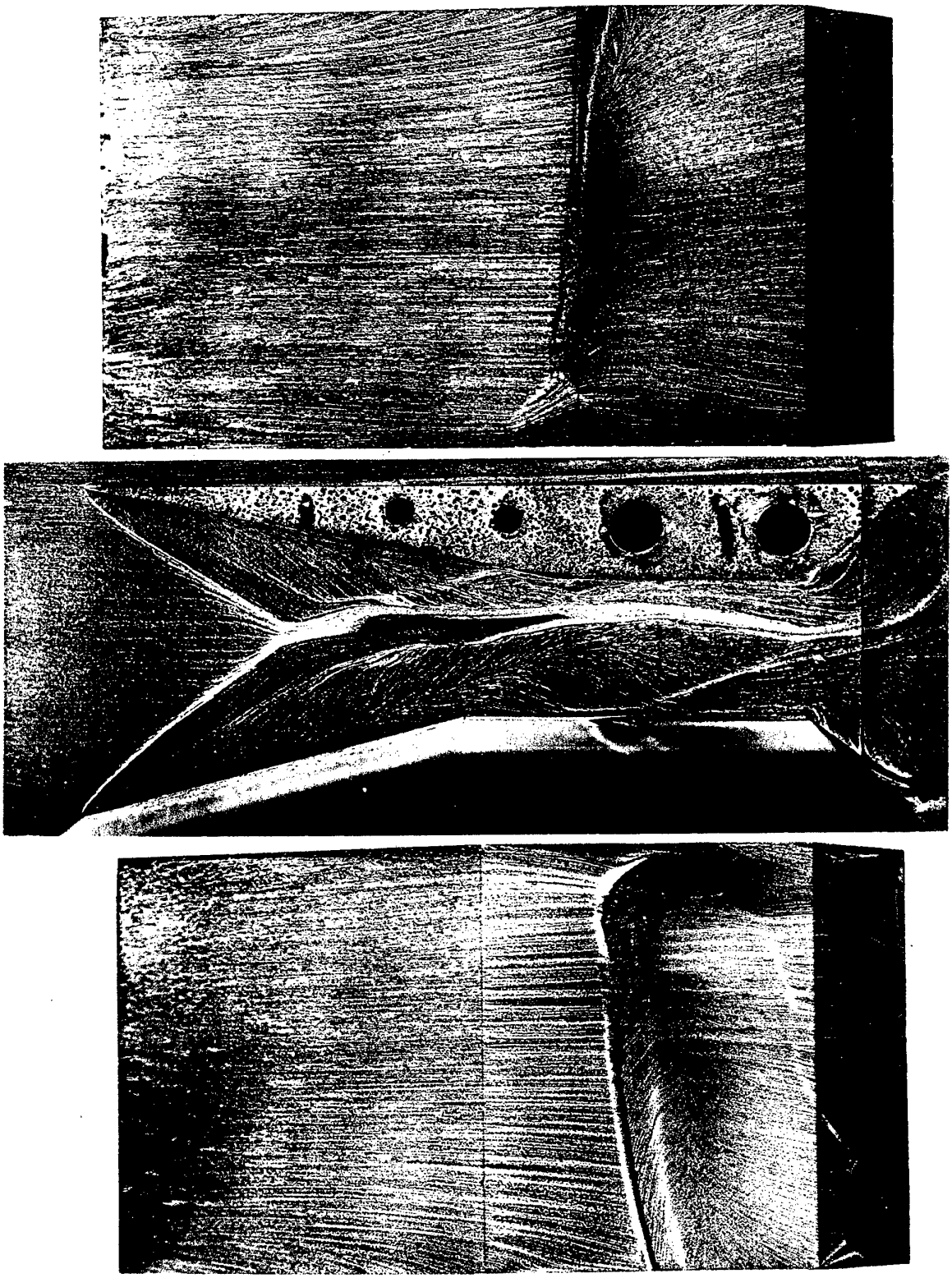

Fig. 10. $M_\infty = 4$, $\beta_1 = 11°$, $\beta_2 = 15°$

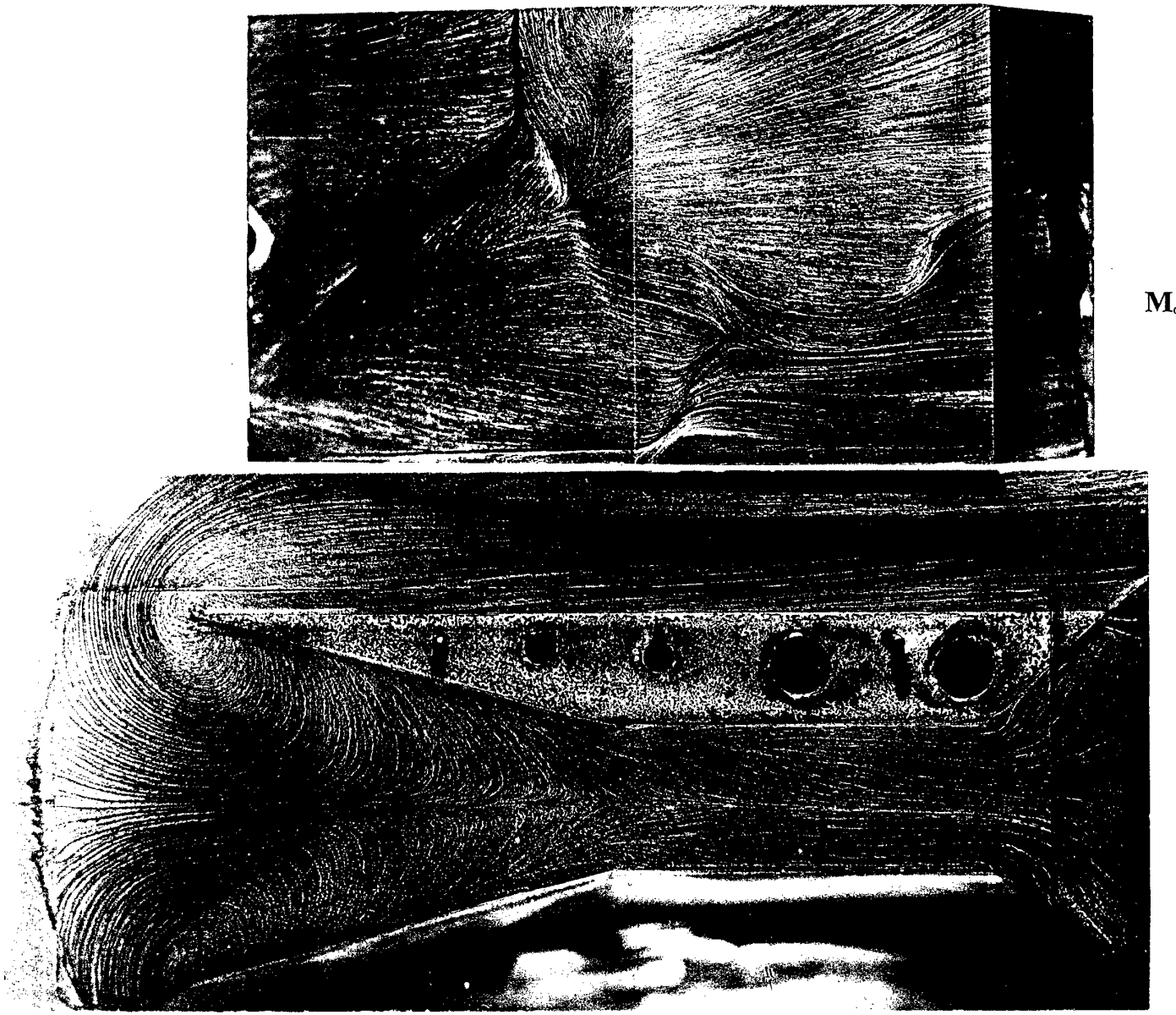

Fig. 11.
$M_\infty = 3$, $\beta_1 = \beta_2 = 15°$

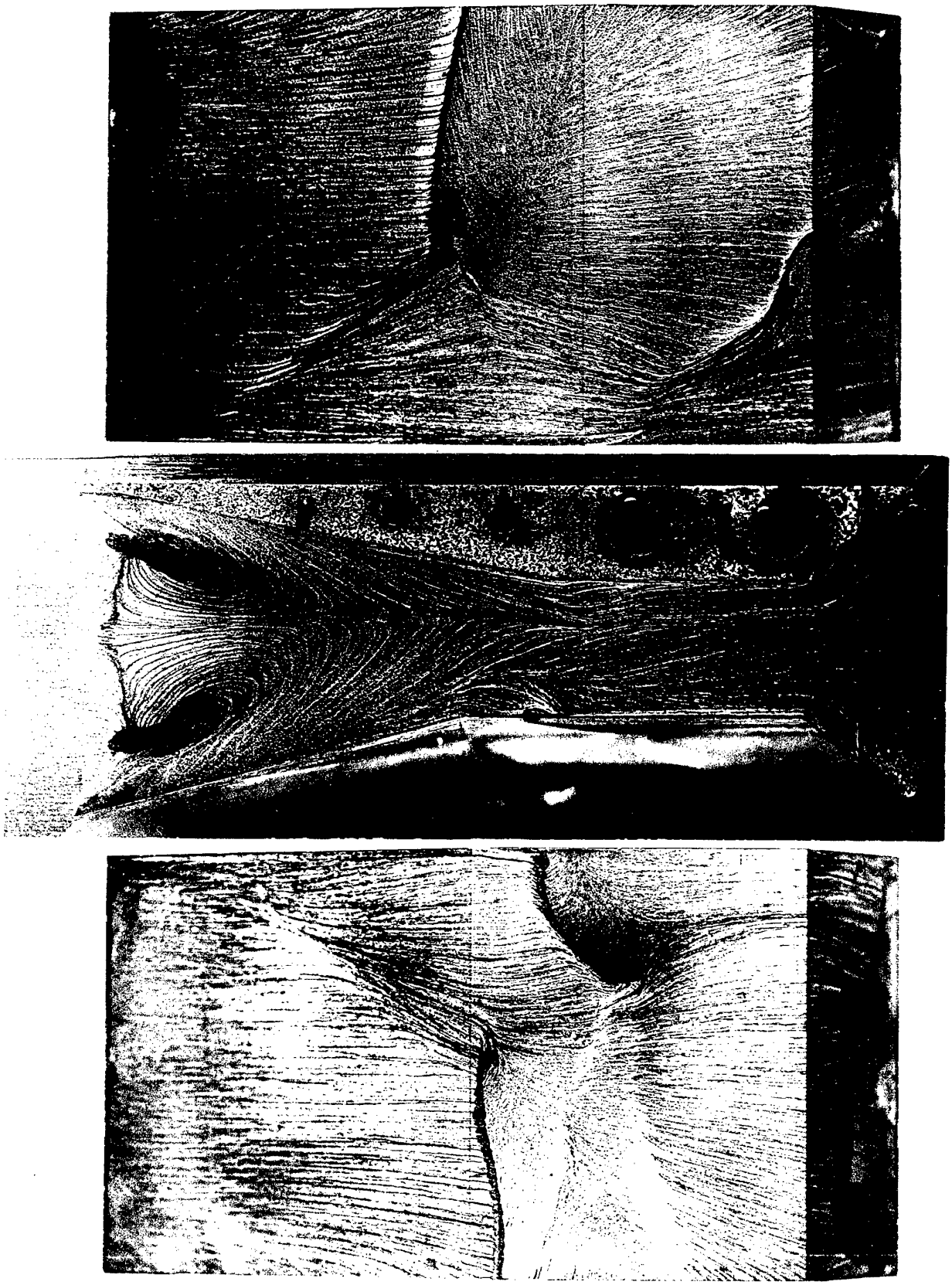

Fig. 12. $M_\infty = 3$, $\beta_1 = 11°$, $\beta_2 = 15°$

APPENDIX 2

TWO FINS GEOMETRY

SURFACE PRESSURE DATA

Wind tunnel facility: T-333 ITAM 22-23.02.94

M_∞=3.89 P_0 = 1.48 MPa T_0 = 258 K Re_1 = 93.2·10^6 m^{-1}

β_1/β_2	7°/7°	11°/11°	15°/15°	7°/11°	7°/15°	11°/15°
P_1, KPa	11.29	11.05	11.31	11.03	11.36	11.14

Throat Middle Line (TML) data

x, mm	P/P_1					
- 4	0.979	0.990	0.979	0.992	0.988	0.975
6	0.979	0.981	0.996	0.983	0.983	0.988
16	1.005	1.005	1.007	1.005	1.007	0.999
22	1.034	1.030	1.020	1.049	1.020	1.036
26	1.008	1.010	1.011	1.009	1.013	1.017
30	0.999	1.003	1.002	0.994	1.005	1.003
34	0.988	1.001	0.989	0.989	0.994	0.997
38	1.008	0.981	0.996	0.978	0.990	0.986
42	1.003	0.999	1.221	0.992	1.098	1.113
46	0.995	1.019	2.073	1.003	1.432	1.441
50	1.144	1.296	2.587	1.256	1.713	1.833
54	1.157	1.571	2.850	1.365	1.771	2.055
58	1.197	1.846	2.966	1.487	1.814	2.251
61	1.255	2.002	3.107	1.581	1.858	2.378
64	1.375	2.188	3.293	1.710	1.944	2.497
67	1.470	2.328	3.651	1.821	2.000	2.563
70	1.566	2.476	3.911	1.912	1.974	2.625
73	1.614	2.585	4.214	1.977	1.925	2.656
76	1.696	2.714	4.620	2.059	1.873	2.590
79	1.772	2.823	5.118	2.137	1.847	2.451
82	1.99	3.01	5.68	2.39	2.10	2.67
85	1.99	3.09	6.24	2.39	2.10	2.82
88	2.07	3.28	6.90	2.47	2.34	3.16
91	2.15	3.47	7.58	2.52	2.55	3.47
94	2.19	3.67	8.15	2.53	2.84	3.96
97	2.28	3.90	8.64	2.52	3.24	4.53
100	2.34	4.15	9.00	2.57	3.72	5.03
103	2.43	4.46	9.34	2.73	4.45	5.67
106	2.49	4.75	9.00	2.93	5.15	6.11
109	2.52	5.04	8.00	3.05	5.20	5.99
112	2.67	5.35	7.02	3.35	5.05	5.99
116	2.71	5.50	5.64	3.46	4.31	5.65
120	2.84	5.77	4.74	3.64	3.83	5.49
124	2.87	5.77	3.85	3.75	3.25	5.72
128	3.03	5.93	3.38	3.98	3.04	6.72
133	3.01	5.86	3.62	4.17	2.66	5.22
138	3.03	5.43	4.75	4.24	2.96	4.52
143	3.20	3.45	5.29	3.56	5.27	4.27
150	3.14	4.51	4.37	3.95	3.95	3.89
160	3.33	2.68	6.46	4.47	4.98	3.42

Cross Sections data

x = 46 mm

z_1, mm						
-25	1.564	2.239	3.434	2.221	3.371	3.430
-20	1.409	1.669	2.171	1.663	2.184	2.178
-15	1.351	1.576	1.659	1.550	1.644	1.639
-10	1.242	1.494	1.787	1.483	1.342	1.787
- 6	1.123	1.358	1.711	1.336	1.620	1.692
- 3	1.045	1.154	1.859	1.134	1.611	1.628
0	0.995	1.019	2.073	1.003	1.432	1.441
3	1.023	1.110	1.828	1.020	1.134	1.243
6	1.045	1.280	1.676	1.043	1.037	1.276
9	1.257	1.516	1.761	1.287	1.279	1.514
12	1.288	1.600	1.720	1.316	1.290	1.600
15	1.395	1.591	1.585	1.372	1.350	1.577
18	1.375	1.516	1.711	1.401	1.370	1.507
21	1.377	1.629	2.259	1.405	1.376	1.613
24	1.509	2.017	3.341	1.550	1.514	1.987
27	1.640	2.437	3.308	1.670	1.620	2.409

x = 79 mm

z_2, mm						
-25	1.885	-	-	-	-	-
-20	1.761	2.616	-	2.566	-	-
-15	1.572	2.412	3.603	2.372	3.561	3.617
-10	1.544	1.944	4.373	1.863	3.315	3.375
- 6	1.668	2.468	3.686	1.688	2.248	2.352
- 3	1.78	2.72	5.01	1.95	1.87	2.46
0	1.772	2.823	5.118	2.137	1.847	2.451
3	1.80	2.73	5.13	2.29	2.31	3.46
6	1.72	2.46	3.75	2.28	2.62	3.70
9	1.65	1.88	4.08	2.15	2.90	3.70
12	1.50	1.95	3.86	1.86	2.91	3.11
15	1.55	2.39	3.70	1.63	2.95	2.44
18	1.69	2.77	3.56	1.71	2.60	2.77
21	1.84	2.70	-	1.85	1.86	2.67
24	1.82	-	-	1.83	1.82	-

x = 112 mm

z_3, mm						
-20	1.95	-	-	-	-	-
-15	2.07	3.09	4.66	2.39	1.28	1.44
-10	2.23	4.34	3.70	3.01	1.30	1.71
- 9	-	4.84	-	-	-	-
- 6	2.41	4.56	5.98	3.33	1.74	2.93
- 3	2.44	4.92	6.63	3.30	2.97	4.77
0	2.67	5.35	7.02	3.35	5.05	5.99
3	2.53	4.98	6.78	3.07	4.95	6.05
6	2.39	4.39	6.12	3.32	3.86	6.78
9	2.26	4.84	4.29	3.29	3.21	7.24
10	-	-	3.70	-	-	-
12	2.21	3.99	-	3.31	4.36	8.20
15	2.12	3.10	4.08	3.04	5.17	8.01
18	1.95	-	-	2.64	5.64	-

APPENDIX 3

TWO FINS GEOMETRY

SURFACE TEMPERATURE AND HEAT TRANSFER DATA

Wind tunnel facility: T-333 ITAM, 19.04.94

$\beta_1 = \beta_2 = 7°$

$P_0 = 1.485$ Mpa; $M_\infty = 3.95$; $Re_1 = 87 \cdot 10^{-6}$ m^{-1}; $T_0 = 260$ K

TML DATA

x, mm	T_{aw}	T_w	α
0	240.2	261.2	270
10	241.2	266.5	262
26	244.6	278.9	227
38	241.3	273.5	246
42	241.6	275.3	233
46	241.6	275.1	226
50	241.7	275.3	222
54	241.9	272.5	227
58	241.9	271.1	237
61	242.3	271.3	239
64	243.3	273.2	232
67	242.7	271.4	242
70	243.6	270.5	258
76	244.1	277.6	226
79	244.1	279.2	226
82	243.8	280.0	217
85	244.7	278.3	229
88	245.4	278.8	218
91	245.4	275.1	234
94	246.0	273.3	248
97	246.0	273.3	248
100	246.0	273.8	242
103	245.2	274.8	235
106	245.8	274.1	251
112	246.1	276.6	244
116	246.7	276.9	237
124	246.0	271.1	265
128	246.3	270.4	258
133	245.8	267.3	280
138	245.8	264.5	299
143	246.6	261.9	343
150	245.1	259.8	337
160	244.6	257.7	299

CROSS SECTIONS DATA

x = 46 mm

z, mm			
-10	240.2	258.9	281
- 6	240.1	268.5	229
- 3	240.5	270.0	236
0	241.6	275.1	226
3	240.5	277.9	214
6	240.4	276.6	223
10	240.2	258.9	281

x = 79 mm

-10	244.1	262.2	317
- 9	244.1	280.5	231
- 3	243.5	281.1	224
0	244.1	279.2	226
3	243.5	281.1	224
9	244.1	280.5	231
12	244.1	262.2	317

x = 112 mm

- 9	241.9	263.8	362
- 6	243.3	265.7	355
- 3	245.2	273.2	271
0	246.1	276.6	244
3	245.2	273.2	271
6	243.3	265.7	355
9	241.9	263.8	362

$\beta_1 = \beta_2 = 15°$

$P_o = 1.470$ Mpa; $M_\infty = 3.95$; $Re_l = 86 \cdot 10^{-6}\ m^{-1}$; $T_o = 261.1$ K

TML Data

x, mm	T_{aw}	T_w	α
0	242.0	260.0	302
10	242.6	266.5	267
26	242.9	286.3	230
30	243.1	277.1	231
38	244.3	271.0	287
42	246.2	271.0	306
46	247.2	271.5	302
50	248.1	272.8	291
54	248.7	271.0	300
58	249.0	269.0	336
61	248.4	267.1	360
64	248.1	264.3	415
67	247.1	259.7	531
70	247.6	259.4	571
76	250.9	274.4	542
79	252.1	272.3	532
82	251.9	266.2	533
85	250.1	262.4	612
88	248.2	258.5	686
91	246.9	254.4	895
94	246.2	252.5	1040
97	244.7	251.0	1040
100	243.7	250.3	984
103	242.2	249.0	993
106	241.8	248.5	1013
112	240.7	249.0	874
116	241.0	249.6	811
124	240.4	249.7	695
128	240.7	251.0	586
133	241.2	251.0	591
138	241.5	248.8	736
143	243.1	249.1	841
150	242.4	248.4	795
160	242.4	248.1	705

CROSS SECTIONS DATA

x = 46 mm

z, mm			
-10	244.1	245.0	466
- 6	244.7	274.1	325
- 3	245.4	275.6	333
0	247.2	271.5	302
3	244.7	270.9	296
6	245.0	270.0	312
10	244.1	245.0	466

x = 79 mm

-10	242.5	248.5	920
- 9	241.6	245.0	609
- 3	246.2	270.6	566
0	252.1	272.3	532
3	246.2	270.6	566
9	241.6	245.0	609
12	240.1	252.2	631

x = 112 mm

- 9	241.3	253.1	652
- 6	241.6	250.1	900
- 3	241.2	248.7	978
0	240.7	249.0	874
3	241.2	248.7	978
6	241.6	250.1	900
9	241.3	253.1	652

$\beta_1 = 7°$; $\beta_2 = 11°$

$P_o = 1.490$ Mpa; $M_\infty = 3.95$; $Re_1 = 88 \cdot 10^{-6}$ m^{-1}; $T_o = 260$ K

TML DATA

x, mm	T_{aw}	T_w	α
0	237.6	259.9	295
10	238.1	266.5	271
26	239.5	278.1	234
30	238.5	-	-
34	237.8	-	-
38	239.2	274.6	261
42	239.6	276.1	252
46	239.5	275.8	244
50	239.9	275.8	242
54	240.1	272.1	253
58	240.4	271.1	264
61	240.8	271.0	269
64	241.6	271.9	268
67	241.6	270.1	284
70	241.7	268.5	303
76	242.9	273.3	291
79	242.7	273.9	297
82	242.1	273.0	297
85	242.9	271.9	311
88	243.8	271.0	313
91	243.2	266.1	353
94	243.5	264.1	386
97	242.7	262.4	403
100	242.1	260.8	421
103	240.8	259.6	431
106	240.1	258.2	457
112	239.5	256.7	505
116	240.1	257.3	486
124	239.3	254.1	529
128	239.2	253.6	505
133	239.5	251.8	569
138	238.6	251.0	529
143	240.4	251.0	578
150	238.5	249.9	505
160	238.0	249.6	420

CROSS SECTIONS DATA

z, mm	x = 46 mm		
-10	238.8	257.6	325
- 6	238.5	267.7	260
- 3	239.2	270.4	260
0	239.5	275.8	244
3	238.8	278.8	234
6	238.3	278.2	237
	x = 79 mm		
-10	240.4	257.0	403
0	242.7	273.9	297
3	242.7	282.0	251
9	242.3	282.3	246
12	240.8	270.4	311
	x = 112 mm		
0	239.5	256.7	505
3	241.3	262.1	424
6	243.3	272.1	322
9	242.9	272.9	309

$\beta_1 = 7°$; $\beta_2 = 15°$

$P_o = 1.498$ MPa; $M_\infty = 3.93$; $Re_1 = 90 \cdot 10^{-6}$ m^{-1}; $T_o = 258$ K

TML DATA

x, mm	T_{aw}	T_w	α
0	242.2	257.3	337
10	243.5	261.9	324
26	244.8	267.1	314
30	244.5	267.5	318
38	242.3	261.6	278
42	243.1	262.5	273
46	242.6	260.4	287
50	243.4	261.2	282
54	243.1	259.4	306
58	244.8	259.3	325
61	243.5	256.3	366
64	243.7	256.0	379
67	242.3	255.3	362
70	243.2	255.3	388
76	243.4	256.6	386
79	241.3	255.7	371
82	239.7	252.9	401
85	239.8	252.2	422
88	239.4	250.7	435
91	238.8	247.6	531
94	239.5	247.3	589
97	238.7	246.6	578
100	238.7	246.5	583
103	237.5	245.3	601
106	237.9	244.7	706
112	237.8	245.6	644
116	237.3	246.0	556
124	238.1	246.5	536
128	238.2	246.6	502
133	238.5	246.3	521
138	238.5	245.0	583
143	239.4	244.8	650
150	239.5	245.7	542
160	238.8	245.0	457

CROSS SECTIONS DATA

z, mm	x = 46 mm		
-10	240.9	249.0	437
- 6	240.1	254.1	315
- 3	240.3	255.0	318
0	242.6	260.4	287
3	240.1	260.9	260
6	239.5	261.2	252
	x = 79 mm		
-10	238.1	245.3	537
0	241.3	255.7	371
3	241.6	257.8	352
9	244.7	264.4	289
12	244.1	266.0	242
	x = 112 mm		
0	237.8	245.6	644
3	237.0	245.3	621
6	237.5	246.6	587
9	238.7	250.0	473

	α/α_1			
β_1/β_2	7°/7°	7°/11°	7°/15°	15°/15°
α_1 (at x)	230(26)	234(26)	278(38)	230(26)

TML DATA

x, mm	α/α_1			
0	1.17	1.26	1.21	1.31
10	1.14	1.16	1.17	1.16
26	0.99	1.00	1.13	1.00
30	-	-	1.14	1.00
38	1.07	1.12	1.00	1.25
42	1.01	1.08	0.98	1.33
46	0.98	1.04	1.03	1.31
50	0.97	1.03	1.01	1.27
54	0.99	1.08	1.10	1.30
58	1.03	1.13	1.17	1.46
61	1.04	1.15	1.32	1.57
64	1.01	1.15	1.36	1.80
67	1.05	1.21	1.30	2.31
70	1.12	1.29	1.40	2.48
76	0.98	1.24	1.39	2.36
79	0.98	1.27	1.33	2.31
82	0.94	1.27	1.44	2.32
85	1.00	1.33	1.52	2.66
88	0.95	1.34	1.56	2.98
91	1.02	1.51	1.91	3.89
94	1.08	1.65	2.12	4.52
97	1.08	1.72	2.08	4.52
100	1.05	1.80	2.10	4.28
103	1.02	1.84	2.16	4.32
106	1.09	1.95	2.54	4.40
112	1.06	2.16	2.32	3.80
116	1.03	2.08	2.00	3.53
124	1.15	2.26	1.93	3.02
128	1.12	2.16	1.83	2.55
133	1.22	2.43	1.87	2.57
138	1.30	2.26	2.10	3.20
143	1.49	2.47	2.34	3.66
150	1.47	2.16	1.95	3.46
160	1.30	1.80	1.64	3.07

CROSS SECTIONS DATA

z, mm	x = 46 mm			
-10	1.22	1.39	1.57	2.03
- 6	1.00	1.11	1.13	1.47
- 3	1.03	1.11	1.14	1.45
0	0.98	1.04	1.03	1.31
3	0.93	1.00	0.94	1.29
6	0.97	1.01	0.91	1.36
10	1.22	-	-	2.03
	x = 79 mm			
-10	1.38	1.72	1.93	4.00
- 9	1.00	-	-	2.65
- 3	0.97	-	-	2.46
0	0.98	1.27	1.33	2.31
3	0.97	1.07	1.27	2.46
9	1.00	1.05	1.04	2.65
12	1.29	1.33	0.87	4.00
	x = 112 mm			
- 9	1.57	-	-	2.83
- 6	1.54	-	-	3.91
- 3	1.18	-	-	4.25
0	1.06	2.16	2.32	3.80
3	1.18	1.81	2.23	4.25
6	1.54	1.38	2.11	3.91
9	1.57	1.32	1.70	2.83